UNIVERSITY OF OKLAHOMA GRADUATE COLLEGE

ASPECT RATIO AND SURFACE CHEMISTRY EFFECTS ON POLYMER-NANOTUBE COMPOSITES

A DISSERTATION

SUBMITTED TO THE GRADUATE FACULTY

in partial fulfillment of the requirements for the Degree of

DOCTOR OF PHILOSOPHY

by MASON RHUE

Norman, Oklahoma

2025

Downloaded from SHAREOK. Persistent Handle URL: https://hdl.handle.net/11244/341589

ASPECT RATIO AND SURFACE CHEMISTRY EFFECTS

ON POLYMER-NANOTUBE COMPOSITES

A DISSERTATION APPROVED FOR THE

SCHOOL OF SUSTAINABLE CHEMICAL, BIOLOGICAL AND MATERIALS

ENGINEERING

BY THE COMMITTEE CONSISTING OF

Dr. Brian Grady, Chair

Dr. Steven Crossley

Dr. Reza Foudazi

Dr. Jivtesh Garg

© Copyright by MASON RHUE 2025

All Rights Reserved.

Acknowledgements

This research was supported by a grant from the National Science Foundation, 2022297, awarded through the CMMI program. I gratefully acknowledge the Strategic Investment Equipment Program sponsored by the VPRP Office at the University of Oklahoma for funds related to the purchase of the TGA. I gratefully acknowledge the University of Arkansas Nano & Bio Materials Characterization Facility for XPS spectral acquisition. Microscopy data collection was performed at the Samuel Roberts Noble Microscopy Laboratory, an OU core facility supported by the Vice President for Research and Partnerships. I gratefully acknowledge Lion Elastomers and ARLANXEO for providing rubber samples.

To my advisor, Dr. Grady, thank you for your guidance throughout graduate school and for pushing me to become a better researcher. To my doctoral committee, thank you for challenging me to think outside the box. To my lab mates, thank you for the invaluable scientific conversations, willingness to help at a moment's notice, and daily encouragement. To the undergraduate student researchers that worked in the lab, thank you for your meaningful contributions to this research and allowing me to mentor you through your laboratory experience. Finally, to my family and friends, thank you for your unwavering and unconditional support over the last five years.

Table of Contents

Table of Tables ..... **viii**

Table of Figures ..... **ix**

Abstract ..... **xv**

Chapter 1: Introduction **1**

1.1 Carbon nanotube properties and applications *1*

1.2 Polymer-nanotube composites *3*

1.3 Current limitations and recent advances in carbon nanotube synthesis *5*

1.4 Implications of aspect ratio on polymer-nanotube composites *6*

1.5 Carbon nanotube length modification *10*

1.6 Carbon nanotube functionalization *12*

1.7 Implications of surface chemistry on polymer-nanotube composites *13*

1.8 Motive and present study *14*

Chapter 2: Experimental **17**

2.1 Materials *17*

2.2 Planetary ball milling *22*

2.3 Mechanochemical functionalization *25*

2.4 Carbon nanotube characterization *27*

2.5 Polycarbonate compounding *29*

2.6 Polycarbonate composite characterization *31*

2.7 Rubber compounding *34*

2.8 Rubber compound characterization *36*

Chapter 3: Carbon nanotube aspect ratio modification by planetary ball milling 38

3.1 Low aspect ratio carbon nanotubes *38*

3.1.1 Minimum single impact energy 38

3.1.2 Length reduction kinetics 43

3.2 Ultrahigh aspect ratio carbon nanotubes *50*

3.2.1 Minimum single impact energy 50

3.2.2 Length reduction kinetics 53

3.2.3 Defect density and electrical conductivity 55

3.3. Comparison to length reduction by ultrasonication *57*

3.3.1 Fracture mechanism 57

3.3.2 Power law length reduction kinetics 61

Chapter 4: Carbon nanotube surface chemistry modification by planetary ball milling 65

4.1 Dry mechanochemical functionalization with ammonium carbonate *65*

4.2 Aqueous mechanochemical functionalization with ammonium carbonate *73*

4.3 Noncovalent mechanochemical functionalization with melamine *79*

4.4 Mechanochemical sulfur-doping for vulcanized rubber additives *85*

Chapter 5: Aspect ratio and surface chemistry effects on polycarbonate-nanotube composites 92

5.1 Compounding *92*

5.2 Percolation behavior *97*

5.2.1 Aspect ratio effects 97

5.2.2 Surface chemistry effects 105

5.3 Thermal properties *107*

5.4 Mechanical properties *112*

Chapter 6: Aspect ratio and surface chemistry effects on tire tread rubber-nanotube composites 114

6.1 Design considerations *114*

6.2 Compounding *115*

6.3 Curing kinetics *119*

6.4 Mechanical properties *122*

6.5 Dynamic mechanical properties *126*

6.6 Surface chemistry effects *129*

Chapter 7: Conclusions 136

Chapter 8: Recommendations 139

Appendix A: Sample Calculation for Burgio-Rojac Model 142

Appendix B: XPS O1s/N1s Core Level Scans of Functionalized CNTs 145

References 151

Table of Tables

Table 1: Morphology of commercial and laboratory synthesized MWCNTs. 21

Table 2: Mechanochemically functionalized CNT specifications and nomenclature..... 26

Table 3: PC composite nomenclature and CNT specifications..... 31

Table 4: Control passenger tire tread rubber compound..... 35

Table 5: Single impact energies associated with Figures 14 and 15..... 50

Table 6: Power law relationships between sonication/milling E_{cum} and CNT length..... 63

Table 7: C1s peak deconvolution analysis corresponding to Figure 30. 72

Table 8: C1s peak deconvolution analysis corresponding to Figure 36. 79

Table 9: C1s peak deconvolution of melamine functionalized NC7000. 85

Table 10: Fitted rheological and electrical percolation parameters. 102

Table 11: Thermal properties of PC-CNT (5.0 wt%) composites measured by DSC/TGA..... 109

Table 12: Loss tangent values of SBR-BR compounds at reference temperatures. 129

Table of Figures

Figure 1: Atomic structure of various carbon nanotubes. 2

Figure 2: Number of published articles containing "carbon nanotube" and "polymer" by year since 1991 according to Web of Science. 4

Figure 3: Schematic of vermiculite exfoliation and impregnation for preparation as support materials for carbon nanotube synthesis by chemical vapor deposition. 18

Figure 4: (a-b) SEM and (c) TEM micrographs of ultrahigh aspect ratio CNTs synthesized on vermiculite supports. 19

Figure 5: SEM and TEM micrographs of (a-b) NC7000, (c-d) C150P, (e-f) SMW200, and (g-h) CSCNT. 20

Figure 6: High resolution TEM micrographs of (a) NC7000, (b) C150P, (c) SMW200, and (d) CSCNT wall morphology. 21

Figure 7: Carbon nanotube diameter distributions measured by TEM. 22

Figure 8: Carbon nanotube length reduction with respect to single impact energy. 39

Figure 9: Relationship between CNT diameter and minimum single impact energy for the four, short commercial carbon nanotubes and another parallel-walled CNT sample previously studied by Kozma et al. [90]. 41

Figure 10: Raman spectra of 0.4 g milled (a) NC7000, (b) C150P, (c) SMW200, and (d) CSCNT. Lengths correspond to data points in Figure 8 and I_D/I_G values are an average of five spectra. 42

Figure 11: SEM micrographs of (a) pristine NC7000 and 0.4 g trial milling times of (b) 10 min, (c) 20 min, and (d) 30 min. 44

Figure 12: Length distributions of (a) pristine NC7000 and 0.4 g trial milling times of (b) 10 min, (c) 20 min, and (d) 30 min with corresponding log-normal distribution parameters. 45

Figure 13: Carbon nanotube length reduction with respect to cumulative impact energy. 46

Figure 14: Normalized length difference collapsed to a single curve with respect to total cumulative impact energy fitted by Equation 20. 48

Figure 15: Normalized length difference collapsed to a single curve with respect to excess cumulative impact energy fitted by Equation 23. 50

Figure 16: SEM micrographs of VNT100 milled for 30 min at (a) 3.5 mJ/impact, (b) 125 mJ/impact, and (e) 175 mJ/impact. 52

Figure 17: SEM micrographs of CNTs milled at 175 mJ/impact for (a) 8 min, (b) 20 min, (c) 36 min, and (d) 60 min corresponding to the data points in Figure 18. 53

Figure 18: Milling-induced length reduction of ultrahigh aspect ratio CNTs compared to length reduction kinetics predicted by Equations 20 or 23. 54

Figure 19: Effects of planetary ball milling on CNT electrical conductivity and defect density. 56

Figure 20: Milling-induced stripping of surface impurities as evidenced by high resolutions TEM micrographs of (a-b) pristine C150P and (c-d) milled C150P. 56

Figure 21: Sonication of carbon nanotubes imparts (a-b) radial buckling on long carbon nanotubes and (c-d) axial tension for short nanotubes. Red arrows indicate the force experienced by the nanotubes, and red dots indicate points of fracture. 58

Figure 22: Representative schematic of impact induced fracture of (a) long and (b) short carbon nanotubes. Red dots indicate points of fracture. Most CNTs fracture points occur at CNT-CNT intersections, but isolated CNTs may fracture as well. 59

Figure 23: Representative TEM micrographs of (a-b) capped, (c-d) open, and (e-f) collapsed CNT ends of parallel walled (NC7000) and cup-stacked (CSCNT) CNTs. 60

Figure 24: Length reduction behavior of carbon nanotubes with respect to cumulative impact energy fit to a power law. 62

Figure 25: Schematic of dry ball milling induced functionalization of CNTs with ammonium carbonate. 65

Figure 26: SEM micrographs of dry mechanochemically functionalized VNT100 milled at 300 rpm for (a-b) 30 min, (c-d) 1 hr, and (e-f) 4 hr. 66

Figure 27: Thermal degradation behavior of dry mechanochemically functionalized VNT100. 67

Figure 28: Degree of functionalization of dry mechanochemically functionalized VNT100 correlated to cumulative impact energy. 69

Figure 29: XPS spectra of pristine and dry mechanochemically functionalized VNT100. 70

Figure 30: C1s core level deconvolution for (a) pristine and dry mechanochemically functionalized VNT100 milled at 300 rpm for (b) 30 min, (c) 1 hr, and (d) 4 hr. 71

Figure 31: Schematic of wet ball milling induced functionalization of CNTs with ammonium carbonate. 73

Figure 32: SEM micrographs of aqueous mechanochemically functionalized VNT100 milled at 300 rpm for (a-b) 30 min, (c-d) 1 hr, and (e-f) 4 hr. 74

Figure 33: Thermal degradation behavior of aqueous mechanochemically functionalized VNT100. 76

Figure 34: Degree of functionalization of aqueous mechanochemically functionalized VNT100 correlated to milling time. 76

Figure 35: XPS spectra of aqueous mechanochemically functionalized VNT100. 77

Figure 36: C1s core level deconvolution for aqueous mechanochemically functionalized VNT100 milled at 300 rpm for (a) 30 min, (b) 1 hr, and (b) 4 hr. 78

Figure 37: Schematic of ball milling induced functionalization of CNTs with melamine. 80

Figure 38: SEM micrographs of melamine functionalized NC7000 milled at 300 rpm (31 mJ/impact) for (a) 30 min, (b) 1 hr, and (c) 4 hr. 81

Figure 39: Thermal degradation behavior of melNC CNTs. 82

Figure 40: XPS spectra of NC7000 CNTs mechanochemically functionalized with melamine. 83

Figure 41: C1s deconvolution for (a) pristine NC7000 and (b-d) melNC milled at 300 rpm for (a) 30 min, (c) 1 hr, and (d) 4 hr. 84

Figure 42: Schematic of ball milling induced functionalization of CNTs with sulfur. 86

Figure 43: SEM micrographs of (a) unpurified sNC, (b) purified sNC, and (c) purified sVNT. 87

Figure 44: Thermal degradation behavior of sVNT CNTs milled at 300 rpm (31 mJ/impact) for 1 hr. 88

Figure 45: FTIR spectra of pristine VNT100 and purified sVNT. 89

Figure 46: (a) Full XPS spectra and high resolution (b) C1s and (c) S2p scans of sVNT. 90

Figure 47: Screw torque curves recorded during PC-CNT compounding..... 93

Figure 48: Linear relationship between CNT length and composite melt viscosity at ejection. . 93

Figure 49: Optical micrographs of PC filled with 0.1 wt% (a-b) VNT100, (c) VNT100*, and (d) mVNT5. 94

Figure 50: SEM micrographs of PC filled with 2 wt% (a-b) VNT100, (c-d) mVNT5, (e-f) dfVNT5, and (g-h) afVNT20. 96

Figure 51: Oscillation frequency sweep curves of PC-VNT100. 98

Figure 52: Consecutive oscillation frequency sweep tests on neat PC at (a) 280 °C and (b) 260 °C. 99

Figure 53: Rheological percolation behavior of CNTs in polycarbonate as measured by composite storage modulus at 0.1 rad/s shear rate. Dotted lines show fits according to Equation 8..... 100

Figure 54: Electrical percolation behavior of CNTs in polycarbonate as measured by electrical conductivity. Dotted lines show fits according to Equation 5. 101

Figure 55: Theoretical (see Equation 4) vs. experimental percolation thresholds from this work and previous work on various short ($\alpha \approx 100$) MWCNTs [60]. 103

Figure 56: Schematic illustration of dispersion mechanism of pristine VNT100 bundles. 104

Figure 57: Oscillation frequency sweep curves of (a) PC-dfVNT5 and (b) PC-afVNT20. 106

Figure 58: Effect of mechanochemical functionalization on electrical percolation behavior of CNTs compared to plain milled CNTs of the same aspect ratio..... 107

Figure 59: Hydrogen bonding between CNT surface groups and polycarbonate chains. 108

Figure 60: TGA curves of PC-CNT composites..... 109

Figure 61: Tensile mechanical properties of PC composites containing 1 wt% CNTs. 113

Figure 62: Rubber compounding curves..... 116

Figure 63: Maximum and final blade torque measurements during compounding for SBR-BR compounds. 118

Figure 64: SBR-BR torque curves during isothermal vulcanization at 160 °C. 119

Figure 65: Degree of vulcanization curves for SBR-BR composites containing (a) 72 phr filler, (b) 52 phr filler, (c) 36 phr filler, and (d) CNT filler only. 121

Figure 66: Vulcanization rate constant dependence on filler type and content. 122

Figure 67: Tensile mechanical properties of SBR-BR composites. 123

Figure 68: Abrasion resistance of SBR-BR compounds measured by mass loss from abrasion testing. 125

Figure 69: Storage modulus, loss modulus, and loss tangent curves for SBR-BR composites containing (a) 72 phr filler, (b) 54 phr filler, and (c) CNTs only. 128

Figure 70: Sulfur doping effects on SBR-BR vulcanization kinetics. 130

Figure 71: Effect of sulfur doping on tensile mechanical properties of SBR-BR composites. . 131

Figure 72: Sulfur doping effects on the abrasion resistance of SBR-BR compounds. 132

Figure 73: Sulfur doping effects on the loss tangent of SBR-BR composites containing dual CB:CNT fillers. 133

Figure 74: Schematic of sulfur-doped CNT interaction with vulcanization SBR-BR rubber. .. 134

Abstract

While carbon nanotubes have demonstrated efficacy as additives in polymer composites due to their superior properties, economic imitations associated with nanotube synthesis have hindered any large-scale applications. Recent advancements in carbon nanotube synthesis on multilayered catalyst supports have greatly surpassed yields of nanotubes grown on traditionally spherical catalysts, potentially removing the need for extra purification processes and thus reducing total cost of production. While most commercially available carbon nanotubes possess aspect ratios (length to diameter ratios) near 100, nanotubes grown on multilayered supports can reach aspect ratios well over 1,000. Hence, this research aimed to enhance the understanding of carbon nanotube aspect ratio on polymer-nanotube composites with additional emphasis on the effects of nanotube surface chemistry. Planetary ball milling, a simple and industrially relevant process, was employed to modify nanotube aspect ratio and surface chemistry. It was found that the kinetic length reduction behavior of carbon nanotubes subject to ball milling could be predicted by a simple exponential expression regardless of nanotube wall morphology, bulk morphology, or initial average length. Additionally, ball milling carbon nanotubes in the presence of species like ammonium carbonate, melamine, and sulfur was found to result in a variety of covalently and noncovalently bonded oxygen, nitrogen, and sulfur containing groups, respectively. Polycarbonate composites containing pristine, ultrahigh aspect ratio carbon nanotubes were found to exhibit high melt viscosities during compounding, leading to notable polymer degradation. Additionally, nanotube dispersion was found to be less than ideal due to the existing interleaved bundle morphology, resulting in higher-than-expected percolation thresholds. Upon ball milling for nanotube length reduction, the processability of composites was found to improve substantially; however, dispersion worsened due to the formation of small, tightly packed agglomerates.

Mechanochemically oxygen-functionalized nanotubes exhibited improved dispersion and lower percolation thresholds than plain ball milled nanotubes of similar lengths due to enhanced interactions with the polymer via hydrogen bonding interactions. Tire tread rubber compounds filled with carbon nanotubes and carbon black/nanotube hybrid filler systems displayed increasing degrees of mechanical reinforcement with increasing filler aspect ratio. Mechanochemically sulfur-doped nanotubes resulted in further improved mechanical reinforcement and reduced rolling resistance, suggesting there may be merit to further study in reducing tire filler content toward improving automobile fuel economy. The implications of this research demonstrate potential for using ball milling as a scalable procedure for controlling carbon nanotube length and surface chemistry for targeted polymer composite properties.

Chapter 1: Introduction

1.1 Carbon nanotube properties and applications

Formally discovered in 1991 by Iijima [1], carbon nanotubes (CNTs) are novel allotropes of elemental carbon best described as two-dimensional graphene sheets (sp^2 hybridized carbon) rolled into cylinders. The varying morphologies of carbon nanotubes are shown in Figure 1. The simplest CNT is the single walled carbon nanotube (SWCNT), containing only one cylindrical layer of graphitic carbon. If there are two layers, the CNT is considered a double walled carbon nanotube (DWCNT), and for three or more layers, they are considered multiwalled carbon nanotubes (MWCNT). The diameters of SCWNTs are typically on the order of 1-5 nm, while MWCNTs can have diameters ranging from 5 to 100 nm. The lengths of carbon nanotubes can vary widely upwards of millimeters depending on the method of synthesis, yielding a wide variety of aspect, i.e. length to diameter, ratios. The length of carbon nanotubes is typically long enough that they are effectively considered one-dimensional materials. Most typically, carbon nanotubes are parallel walled, meaning their walls are parallel to the axial direction. In other words, they contain continuous layers of cylindrical graphene along the length of the nanotube. Alternatively, carbon nanotubes can have varying wall morphologies, most notably containing walls slanted relative to the axial direction of the nanotube. There are a wide variety of these types of nanotubes, often termed cup stacked, cone stacked, herringbone, fishbone, and/or bamboo shaped carbon nanotubes [2].

The unique morphology and composition of carbon nanotubes imparts equally unique material properties. The mechanical strength of carbon nanotubes is nearly unrivaled in material science, second only to other graphene derivatives and diamond [3, 4]. The tensile strength of CNTs has been shown to be upwards of 100 GPa for individual nanotube layers, confirmed by

both experimental and computational measurements [5, 6]. Additionally, the Young's modulus of CNTs has been measured at over 1,000 GPa for pristine CNTs with few defects [7]. Carbon nanotubes are also good electrical conductors due to the conjugated graphitic backbone, allowing for electron delocalization and transfer along the length of the nanotube. The electrical conductivity of carbon nanotubes can vary widely from semiconducting up to near metallic levels (~10^4 S/cm) and largely depends on nanotube chirality and graphitic purity [8-10]. Due similarly to the conjugated structure, carbon nanotubes also exhibit high thermal conductivity upwards of 6000 W/m·K [11].

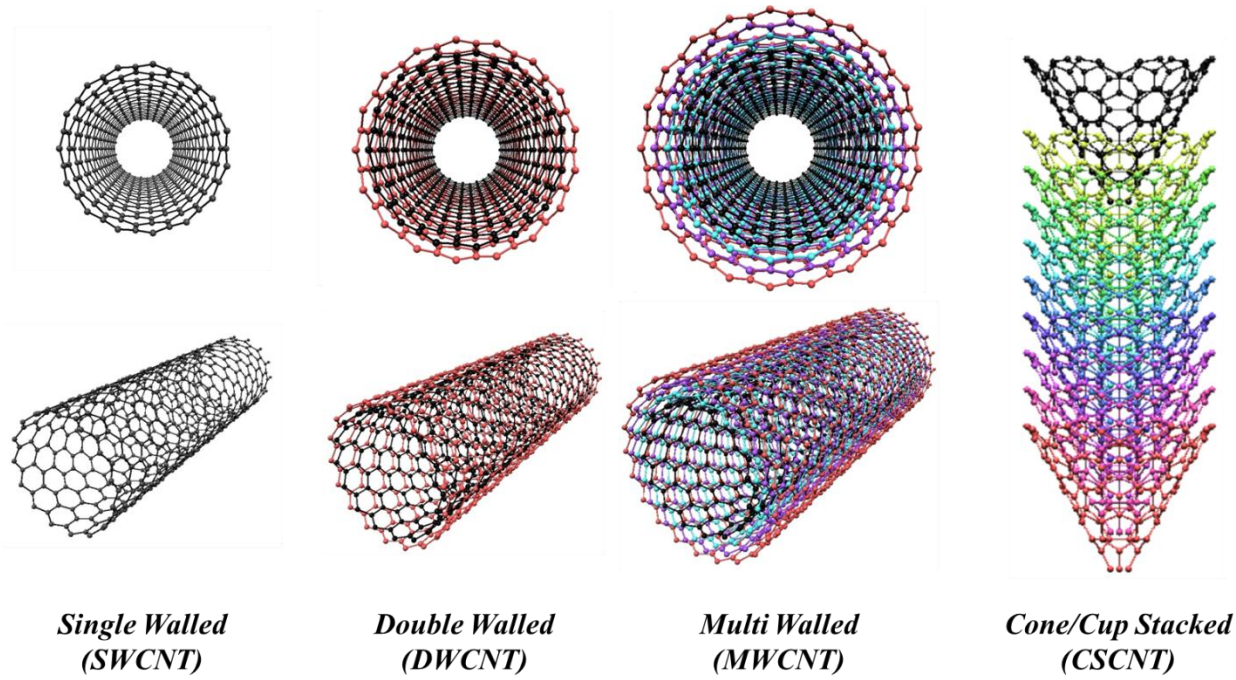

Figure 1: *Atomic structure of various carbon nanotubes.*

Due to these superior material properties, carbon nanotubes have been targeted in many applications. Due to their high aspect ratio and high electrical conductivity, yarns spun from carbon nanotubes have been shown to have high tensile strengths (> 1 GPa) and high electrical

conductivities (> 10^2 S/cm) [12], making CNT yarns interesting suitors for applications in lightweighting aerospace/automotive components [13] and flexible, wearable electronics [14]. Electrical applications of CNTs are vast with demonstrated efficacy in energy storage [15, 16], and fuel cells [17]. The tunable chemistry and diameter of CNTs has yielded applications in membrane technology for water treatment [18] and bioseparations [19]. Other unique applications for CNTs such as carriers for targeted drug delivery and tissue engineering scaffolds have been of interest to the biomedical field [20, 21].

1.2 Polymer-nanotube composites

Perhaps the largest and most intriguing application for carbon nanotubes is in polymer composites. Figure 2 shows the percentage of published nanotube-relevant articles including content regarding polymer-related applications, with present day approaching 25%. Polymers are important materials in everyday life as they are typically lighter and less expensive compared to comparable materials like metals (stainless steel, aluminum, etc.) and ceramics (porcelain, metal oxides, etc.). While most polymers lack the heat and wear resistance of ceramics or the conductivity and strength of metals, incorporation of additives to polymers allows for the tuning of composite properties to allow for suitable replacement of these two traditional materials.

A primary advantage of carbon nanotubes in polymers is their superior degree of lightweighting compared to other traditional fillers like carbon black due to two factors: filler density and filler content required for adequate reinforcement. SWCNTs typically have a density around 1.3-1.4 g/cm^3, while MWCNTs typically have a density near 1.7-1.9 g/cm^3, though these values vary widely depending on nanotube diameter and number of walls [22]. In comparison, carbon black, the most common carbon-based filler used for mechanical reinforcement,

pigmentation, and UV protection of plastics, has a density of roughly 1.9-2.1 g/cm^3. Other common non-carbon polymer additives like talc and calcium carbonate have a density of 2.7 g/cm^3. These factors, combined with their superior individual properties, make them prime candidates for replacing traditional additives in a variety of applications.

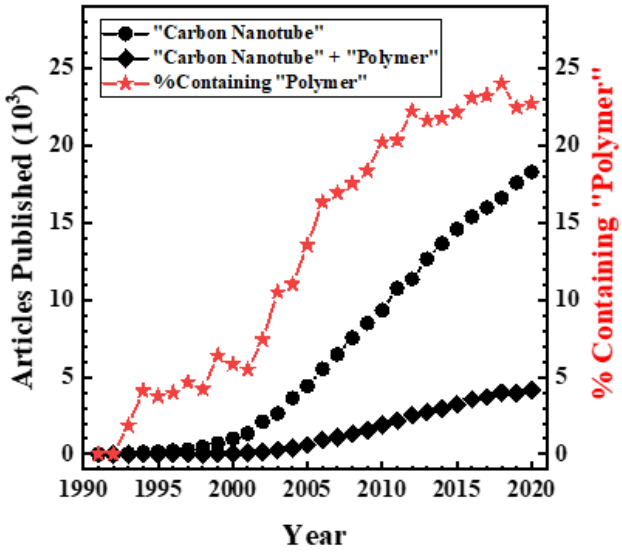

Figure 2: *Number of published articles containing "carbon nanotube" and "polymer" by year since 1991 according to Web of Science.*

The positive effects of carbon nanotube incorporation on the mechanical reinforcement of polymers are well documented, showing improved the strength and stiffness for thermoplastics [23, 24], rubbers [25, 26], and rigid thermosets [27, 28]. The electrical conductivity of polymer-CNT composites has been shown to increase by upwards of ten orders of magnitude into the semiconducting range upon addition of 1 wt% (or less) CNTs compared to the neat insulating polymer [29, 30]. Additionally, the thermal conductivity of polymer-nanocomposites has been shown to increase by multiple orders of magnitude relative to the neat polymer [31]. These

composite property enhancements have made polymer-CNT composites suitors in many applications such as lightweighting for automotive [32] and aerospace [33] components, thermoelectrics [34], and EMI shielding [35, 36].

1.3 Current limitations and recent advances in carbon nanotube synthesis

Despite the proven benefits of carbon nanotubes as additives in polymer composites, widespread industrial application of these materials has yet to occur largely due to their currently limited economic viability compared to other common polymer additives, stemming from high costs associated with carbon nanotube production. Carbon nanotubes can be produced from a variety of processes including arc discharge and laser ablation; however, the most common method of producing carbon nanotubes at an industrial scale is chemical vapor deposition (CVD) [37]. Typical industrial chemical vapor deposition processes for CNT synthesis use roughly spherical catalyst supports like silicon oxide and/or aluminum oxide particles [38-40]. While yields vary widely depending on reaction conditions and catalysts used, the CNTs produced from these processes typically reach yields on the order of 5 g_{CNT}/g_{cat} (~80% carbon purity) for MWCNTs, necessitating the removal of catalyst and support material by additional processing steps [41, 42]. The cost of industrially available MWCNTs is near $50/kg, although some grades of MWCNTs can be found at $10-20/kg [43]. SWCNTs are typically much more expensive at upwards of $100-1000/g due to the more precise synthesis controls necessary and even lower synthesis yields compared to MWCNTs. For comparison, carbon black can be purchased near $1/kg [44].

Alternatively to spherical catalyst supports, flat monolayered supports, such as aluminum foil and silicon oxide wafers, have been used to synthesize vertically aligned carbon nanotube arrays, often dubbed “forests” due to their appearance of unidirectional growth similar to trees [45,

46]. CNT forests grown on monolayered supports can reach lengths upwards of millimeters, which is promising for increasing carbon yield relative to catalyst and support material [47, 48]. However, CNTs grown on monolayered supports must still be purified by stripping them from the support surface. Some studies have extrapolated this idea by using lamellar catalyst supports, such as mineral clays like vermiculite, mica, and montmorillonite [49-51]. Exfoliation of individual clay layers substantially increases the surface area to mass ratio of the support mateiral, increasing the number of sites for catalyst particle deposition for CNT growth. While the CNT growth mechanism is effectively the same compared to forest grown on monolayered supports, clay sheets often break apart during synthesis, resulting in long, loosely packed bundles. Our collaborators have shown that in the case of good clay exfoliation and long CNT growth (~100 μm), carbon yields have surpassed 95 wt%, suggesting purification of the carbon nanotubes may not be necessary depending on the application [52]. Thus, these grades of carbon nanotubes make a strong economic case for application in polymer composites, and the effects of adding these nanotubes to various polymers will be studied in this work.

1.4 Implications of aspect ratio on polymer-nanotube composites

The effects of filler aspect ratio on the mechanical properties of composites have been studied extensively and yield a variety of models. Landmark studies by Halpin and Tsai derived relationships between fiber aspect ratio and composite modulus by the general form

$$E_c = E_m\left(\frac{1+\xi\eta\varphi}{1-\eta\varphi}\right) \tag{1}$$

$$\eta = \frac{\left(\frac{E_f}{E_m}-1\right)}{\left(\frac{E_f}{E_m}+\xi\right)} \tag{2}$$

$$\xi = 2\frac{L}{D} = 2\alpha \tag{3}$$

where E_c is the composite modulus, E_m is the matrix modulus, E_f is the fiber modulus, ξ is the reinforcement factor, φ is the fiber content, L is the fiber length, and D is the fiber diameter, and α is the aspect ratio [53]. While originally derived for uniaxially aligned fiber composites, the equations can be modified to describe the mechanical reinforcement effects of randomly oriented fiber composites. According to Equations 1-3, an increased fiber aspect ratio results in an increased composite modulus. This phenomenon is generally attributed to the increased surface area over which a load can be transferred from the matrix to the filler. Thus, a high degree of mechanical reinforcement could be expected for high aspect ratio CNTs; however, it should be noted that degree of dispersion, CNT curvature, and polymer-CNT adhesion also play major roles.

Considering electrically conductivity fillers like carbon nanotubes, filler aspect ratio also plays a large role in the electrical conductivity of composites due to the percolation effect. Percolation occurs when a filler forms a three-dimensionally connected network within a system. For a randomly dispersed system where each nanotube exists individually (i.e., no bundling or agglomeration) and is assumed to be a rigid rod, a simple geometric relationship exists between filler aspect ratio and theoretical volume percolation threshold, $\varphi_{c,theo}$ [54].

$$\varphi_{c,theo}\ [vol\ frac] = \frac{D}{2L} = \frac{1}{2\alpha} \tag{4}$$

In practice, the formation of a percolated CNT network in polymers has been shown to cause sharp divergences in composite electrical and rheological properties upon small changes in CNT content. Electrical percolation occurs as the distance between CNTs in the composite decreases sufficiently to allow for either direct electron transfer between CNTs in direct contact or electron tunneling/hopping between CNTs in close proximity [55, 56]. Efficient electron tunneling/hopping

typically requires CNTs to be within ~5 nm of each other [57]. The bulk electrical conductivity, σ, of polymer-CNT systems has been shown to exhibit power law behavior with respect to CNT content by the following

$$\sigma = \sigma_o\left(\varphi - \varphi_{c,\sigma}\right)^{\beta_\sigma} \tag{5}$$

where $\varphi_{c,\sigma}$ is the electrical percolation threshold and σ_0 and β_σ are fitted parameters [58, 59]. Most commercial CNTs have aspect ratios on the order of 100, giving a theoretical percolation threshold of 0.5 wt% according to Equation 4, which is roughly equivalent to what has been found experimentally for well-dispersed systems [60]. While the effects of CNT aspect ratio on composite properties have been studied previously, the upper limits of CNT aspect ratio in these studies rarely eclipse ~500 [61-63], suggesting there may be further improvements in percolation behavior that could be obtained from higher aspect ratio carbon nanotubes. Additionally, because a higher degree of CNT intersection can be expected for higher aspect ratio CNTs above the percolation threshold, higher bulk composite conductivities may also be achieved.

While the positive implications of high filler aspect ratio on composite mechanical and electrical properties are clear, some negative drawbacks exist with respect to composite rheological properties. In the context of melt-mixed compounds, melt viscosity is an important consideration in composite processing to inhibit polymer degradation; some studies have shown significant reductions in thermal stability and molecular weight of polymers upon incorporation of carbon nanotubes by melt mixing [64, 65]. The relationship between filler aspect ratio and suspension viscosity has been studied previously and has yielded a variety of empirical and theoretical models. Douglas and Gorbaczi [66] studied the relationship between suspension intrinsic viscosity, $[\eta]$, and filler aspect ratio, and the following empirical relationship

$$[\eta] \approx \frac{1012 + 2904\alpha - 1855\alpha^{1.5} + 1604\alpha^2 + 80.44\alpha^3}{1497\alpha + \alpha^2} \quad (6)$$

was developed by Bicerano et al. to described a large range of filler aspect ratios up 1,000 [67]. The intrinsic viscosity describes the effect of a filler on the viscosity of a suspension and is defined as follows

$$[\eta] = \lim_{\varphi \to 0} \frac{\eta - \eta_o}{\eta_o \varphi} \quad (7)$$

and where η is the suspension viscosity and η_o is the unfilled viscosity. While the basic forms of intrinsic viscosity evaluation are valid only for Newtonian fluids (i.e., not directly valid for non-Newtonian polymer melts), it can be deduced that high filler aspect ratios would result in high composite melt viscosities relative to a neat polymer melt.

The rheological properties of polymer-CNT composites under shear stress can also elucidate information about CNT percolation. Rheological percolation occurs when CNTs become close enough in proximity to affect the bulk rheological properties of the composite. Because the presence of CNTs can cause an immobilization of polymer chains near the surface of nanotubes, CNTs do not need to be in direct contact to cause changes bulk composite rheological properties. This critical nanotube-nanotube distance has been shown previously to be dependent on polymer radius of gyration and is on the order of 10-100 nm [68, 69]. The storage modulus, *G'*, of polymer-CNT composites measured at low shear rates (e.g., 0.1 rad/s) is particularly sensitive to the formation of a percolated CNT network such that a similar power law behavior to Equation 5 is typically seen with respect to CNT content by the following

$$G' = G'_o\left(\varphi - \varphi_{c,G'}\right)^{\beta_{G'}} \quad (8)$$

where $\varphi_{c,\sigma}$ is the electrical percolation threshold and G'_o and $\beta_{G'}$ are fitted parameters [70-72]. The sharp increase in storage modulus upon small additions of CNT to a composite indicates a shift

from viscous-like behavior to solid-like behavior of the composite. While this percolation phenomenon is good for electrical conductivity, the additional effect in increasing composite viscosity can make processing difficult for systems with high aspect ratio fillers and for filler contents notably above the percolation threshold. Thus, in the context of melt-mixed polymer-CNT composites with ultralong nanotubes, investigation into carbon nanotube length reduction before compounding is likely warranted.

1.5 Carbon nanotube length modification

Because the growth of long carbon nanotubes is advantageous for increasing yield during synthesis to improve economics of production, the reduction of carbon nanotube length after synthesis would likely be desired. Attempts have been made previously to model the kinetics of carbon nanotube length reduction based on parameters of the breaking process. Studies on carbon nanotube length reduction by ultrasonication discuss the mechanisms of CNT fracture and find a power law relationship between cumulative sonication energy and resulting carbon nanotube length [73-77]. These studied indicate that a terminal length will eventually be reached, though the power law fit was not extended to this limit [75]. However, the dependence of length reduction on sonication energy varies in different studies and seems to vary for different nanotube morphologies (i.e., parallel walled, cup stacked, bamboo shaped, etc.) [78]. However, implementing sonication on an industrial scale would prove difficult as it would require further separation of the carbon nanotubes from solvent, effectively eliminating the positive effects of initially removing the purification steps during synthesis.

Ball milling is a well understood process used in particle size reduction and has been employed for reducing carbon nanotube length and agglomeration [79, 80]. Ball milling for CNT

length reduction is particularly enticing due to its relative simplicity, low cost, and capacity for optimization on an industrial scale. Attempts to correlate carbon nanotube length reduction to ball milling parameters like milling time have been made previously [81]. However, these empirical correlating equations cannot be applied to other systems due to the use of system specific parameters. Further, many ball milling studies only model length reduction based on milling time without sufficient detail to other important parameters like rotational speeds, grinding media size and material, etc., making it difficult to extend these results to different carbon nanotubes.

Burgio et al. derived an expression that models the impact energy of planetary ball milling for use in the mechanical alloying of a Fe-Zr system [82, 83]. Further studies adding detail to the mathematical understanding of planetary ball milling validated this energy model based on power measurements during mechanical alloying [84, 85] and made corrections to the impact energy expression considering factors like collision elasticity [86] and grinding media hindering. This energy model was particularly useful in correlating cumulative energy of milling to phase changes in the Pd-Si [87], Ti-Al [88], and Mo-Si [89] alloy systems. Kozma et al. were the first to and only group (prior to the work described in this thesis) to apply this energy model to planetary ball milling of carbon nanotubes and found that, for a single type of carbon nanotube, an impact energy barrier exists at 35 mJ for which meaningful length reduction occurs only above that energy barrier [90]. Like sonication studies, an apparent terminal length was found at high milling times where little to no further length reduction occurred. However, further study of the energy collision model for relating milling conditions to CNT length reduction is warranted given that carbon nanotubes may fracture differently depending on their initial length, diameter, wall morphology, and bulk morphology.

1.6 Carbon nanotube functionalization

Carbon nanotube functionalization has been studied extensively for a variety of applications. Common approaches for functionalizing carbon nanotubes generally involve the use of solvents, mechanical stirring/mixing, and heating. Perhaps the most common of these approaches is CNT ultrasonication and/or boiling in sulfuric acid, nitric acid, or a mixture of the two, resulting in primarily carboxylic acid groups on CNT surfaces and ends [91-93]. However, the variety of reported carbon nanotube functionalization methods is extensive and wide-ranging in the reported literature. For example, Simmons et al. noncovalently functionalized SWCNTs with pyrenecarboxylic acid (PCA) via π-π interactions by conducting a series of ultrasonic bath treatments on SWCNT dispersions in methanol containing dissolved PCA [94]. Hsieh et al. fluorinated CNTs by impregnation with a solution of perfluoroalkyl methacrylic copolymer for applications in water-oil membrane separation technology, improving water-oil separation efficiency by 10-20% compared to unfunctionalized CNTs [95]. Knyazev et al. produced SWCNTs with functional amine and thiol groups by modification with 4-(2-aminoethyl)benzenediazonium tetrafluoroborate via diazonium addition followed by N-hydroxysuccinimide ester and 4-maleimidobutyric acid for the selective adsorption of bovine serum albumin protein [96]. These examples represent a miniscule fraction of reported CNT functionalization approaches and applications, but while these functionalization approaches have proven effective, harsh solvents and exotic chemicals would be likely be a hindrance on an industrial scale.

While ball milling was previously discussed in context of carbon nanotube length reduction, ball milling has also been used to functionalize graphitic materials. Ball milling has a distinct advantage in industry-facing applications in that it is often applied as a dry, solvent-free

process. Ball milling can impart functionalization through the spontaneous interaction of broken carbon-carbon bonds with other adjacent chemical species. Early investigations by Konya et al. into mechanochemical functionalization of carbon nanotubes used milling vessels charged with high pressure gases like CO_2, NH_3, and H_2S, among others, resulting in ketone, amine and amide, and thiol functionalities, respectively [97]. Other applications have since been studied through milling carbon nanomaterials in the presence of solid species like sulfur [98] and methyl-2-azidoacetate [99]. Co-milling carbon nanotubes with polymers has also been found to encourage polymer wrapping around and grafting to CNT surfaces [100].

1.7 Implications of surface chemistry on polymer-nanotube composites

The presence of functional groups of carbon nanotube surfaces is generally advantageous in the context of polymer composites, and the mechanism by which functionalization improves polymer-CNT adhesion depends on the type of functionalization and the nature of the polymer-CNT system. The presence of functional groups on CNT surfaces can add a physical layer of separation between adjacent nanotubes that would otherwise agglomerate and interact through van der Waals forces. Additionally, functional groups on carbon nanotube surfaces can interact with functional groups on polymer chains via weak but prevalent non-covalent interactions, like hydrogen bonding and π-stacking. Reactive extrusion and in-situ polymerization have also been used to fabricate covalently linked polymer-nanotube composites [101, 102], further strengthening the interactions between the polymer and filler.

Due to enhanced polymer-nanotube chemical interactions, functionalization of CNTs often leads to improvements in composite properties compared to unfunctionalized CNTs. Yang et al. found that the thermal conductivity enhancement of epoxy-CNT composites roughly doubled upon

CNT modification with 1,3,5-benzenetricarboxylic acid [103]. Barick et al. showed that the tensile strength and elastic modulus of thermoplastic polyurethane composites increased by upwards of 64% and 15%, respectively, upon carboxylic acid modification of CNT surfaces [104]. The electrical and rheological percolation thresholds of functionalized CNTs have often been shown to be lower than that of unfunctionalized CNTs due to improved dispersion [105, 106]. However, while some studies have shown positive effects of mechanochemical functionalization on the mechanical strength and dispersion of polymer composites [107, 108], the coupled effects of filler aspect ratio reduction and surface chemistry have been rarely discussed and are thus a focus of this work.

1.8 Motive and present study

This research aimed to close some critical gaps in knowledge related to carbon nanotubes and polymer-CNT composites. Of particular interest was the applicability of ultrahigh aspect ratio ($\alpha >> 1{,}000$) carbon nanotubes grown on vermiculite supports in polymer composites. Based on the previous literature review, notable gaps in the literature that warranted further study included (a) effects of CNT morphology on their length reduction behavior when subject ball milling, (b) effects of CNT aspect ratios well over 1,000 on the processing and properties of polymer composites, (c) simultaneous effects of CNT aspect ratio and surface chemistry on the properties of polymer composites, and (d) potential for ultrahigh aspect ratio CNTs implementation in large scale polymer composite applications. Chapter 2 outlines the experimental methods for CNT length reduction and mechanochemical functionalization by planetary ball milling as well as polymer-CNT compounding and characterization.

In Chapter 3, the kinetics of carbon nanotube length reduction by planetary ball milling were investigated. The Burgio-Rojac model was employed to translate milling conditions, like rotational speed, grinding media size, milling time, etc., to impact energy. First, the length reduction of short, commercially available carbon nanotubes was studied to gain a universal understanding of how carbon nanotubes fracture when subject to ball milling. The effects of CNT diameter, wall morphology, and bulk morphology on the minimum single impact energy for fracture were investigated. The kinetics of CNT length reduction with respect to milling time were studied, and an exponential expression relating cumulative impact energy to a normalized length term was developed. This relationship was then verified by ball milling ultrahigh aspect ratio CNTs and tracking their length reduction with respect to cumulative milling energy. Additionally, the mechanism of carbon nanotube fracture by ball milling was discussed and compared to other nanotube fracture processed like sonication. Previously established power law kinetics of CNT length reduction by sonication were compared to length reduction by ball milling.

In Chapter 4, facile approaches for mechanochemical functionalization of carbon nanotubes using ball milling were investigated. First, CNTs were ball milled in the presence of ammonium carbonate in both dry and aqueous environments to target covalently bonded oxygen and nitrogen containing functional groups. CNTs were also milled in the presence of melamine to target noncovalent functionalization via π-π interactions. Finally, CNTs were ball milled in the presence of elemental sulfur to produce sulfur-doped CNTs for applications in vulcanized rubber-CNT composites. The effects of milling conditions, primarily milling time, on the types and extents of functionalization were studied.

In Chapter 5, the effects of carbon nanotube aspect ratio and surface chemistry on the properties of polycarbonate-carbon nanotube composites produced via melt mixing were

investigated. Polycarbonate was chosen as a model polymer-CNT system due to its amorphous nature (i.e., no crystallization effects) and due to the readily available previous literature for comparison. Using planetary ball milling, initially 100 μm long CNTs were milled to desired lengths between 50 μm and 5 μm. Additionally, mechanochemically oxygen-functionalized CNTs of comparable lengths were obtained by ball milling. Pristine, milled, and mechanochemically functionalized CNTs were compounded in polycarbonate by melt mixing in a twin-screw extruder. The effects of aspect ratio and surface chemistry on composite processability were evaluated based on melt viscosity and thermal properties. The effects of aspect ratio and surface chemistry on CNT dispersion were evaluated based on visual observation in a scanning electron microscopy as well as measured electrical and rheological percolation behavior.

Finally, in Chapter 6, a potential large-scale application of ultrahigh aspect ratio carbon nanotubes as fillers for tire tread rubber was considered. A typical passenger tire tread compound based on a styrene-butadiene and butadiene rubber blend with carbon black reinforcement was identified as a control. The effects of partial and full replacement of carbon black with ultrahigh aspect ratio CNTs on the vulcanization, rheological, mechanical, dynamic mechanical, and wear properties of tire rubber were investigated. Additionally, the effects of mechanochemical sulfur doping of CNTs on rubber compound properties were studied. Finally, this work was concluded with an overall summary of the findings and their implications along with future research directions.

Chapter 2: Experimental

2.1 Materials

Ultrahigh aspect ratio multiwalled carbon nanotubes were synthesized by a collaborator (Caleb Bavlnka) using the following procedure [52], and a representative schematic is given in Figure 3. Vermiculite (Sigma Z765422) was wet sieved to 150-350 μm and dried at 300 °C for one hour. A 0.81 M dodecyltrimethylammonium bromide solution, which is more than 2 orders of magnitude above the critical micelle concentration, was introduced to the sieved vermiculite by incipient wetness impregnation and allowed to fully absorb for 15 min. Surfactant-loaded vermiculite was dried in a muffle oven preheated to 800 °C for 5 mim, resulting in clay layer exfoliation. This exfoliation process was conducted twice to maximize clay surface area available for metal catalyst particle deposition. Then, a catalyst solution composed of 0.8 wt% Co and 1.6 wt% Fe in water was prepared from iron (III) nitrate nonahydrate and cobalt (II) nitrate hexahydrate. The catalyst solution was introduced to the exfoliated vermiculite dropwise by incipient wetness impregnation and allowed to sit overnight for maximal absorption. The vermiculite was then dried at 100 °C for one hour, allowing for complete water evaporation and metal catalyst particle deposition throughout the entire pore volume of the exfoliated vermiculite. Impregnation and drying were repeated once to ensure complete and even metal coverage on the treated vermiculite. Finally, the catalyst was calcined at 450 °C for one hour.

Carbon nanotube synthesis was conducted via chemical vapor deposition in a 1” ID quartz tube oriented vertically to create a fluidized bed reactor consisting of 70 mg of catalyst. While the temperature ramped to 650 °C at 10 °C/min, the catalyst was reduced via 200 sccm hydrogen. The system was maintained at 650 °C for 30 min under hydrogen for the desired reduction. Then, 200 sccm of nitrogen was flown to purge the reactor during a ramp to 675 °C. After reaching the

reaction temperature of 675 °C, ethylene and nitrogen were co-flown at 200 sccm each for 30 minutes to complete CNT growth. Pure nitrogen flowed through the reactor during cooling to room temperature. The carbon yield was determined to be 25 g_{CNT}/g_{cat} (>95% carbon purity) from the weight lost during complete combustion of the CNT sample in air at 600°C. The resulting CNTs were ~100 μm in length and 15 ± 6 nm in diameter ($\alpha \approx 6{,}700$) as measured from electron micrographs; representative SEM and TEM micrographs are presented in Figure 4. These ultrahigh aspect ratio CNTs will hereafter be referred to as VNT or VNT100.

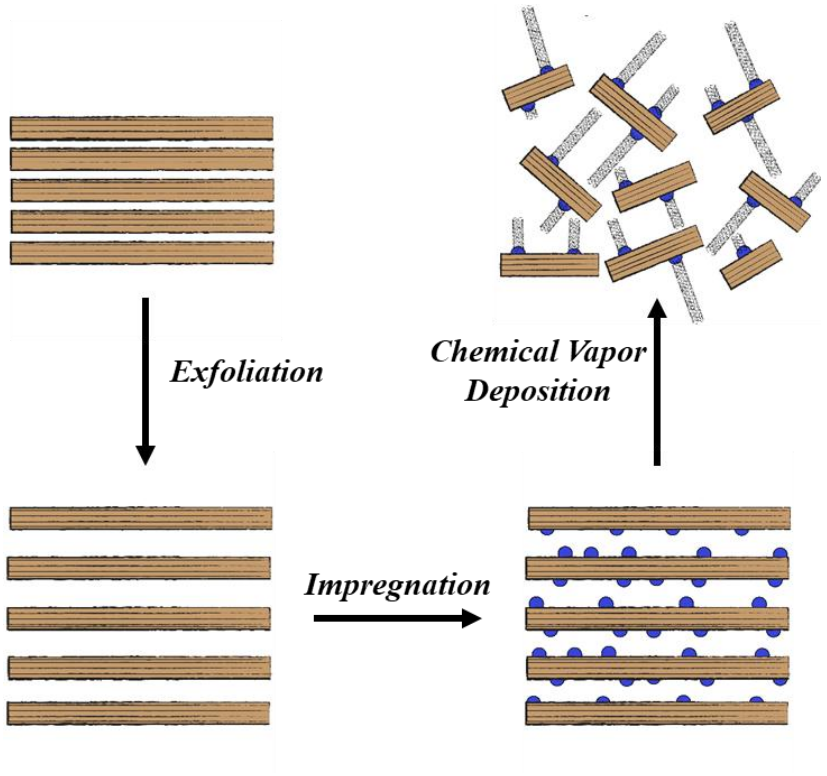

Figure 3: *Schematic of vermiculite exfoliation and impregnation for preparation as support materials for carbon nanotube synthesis by chemical vapor deposition.*

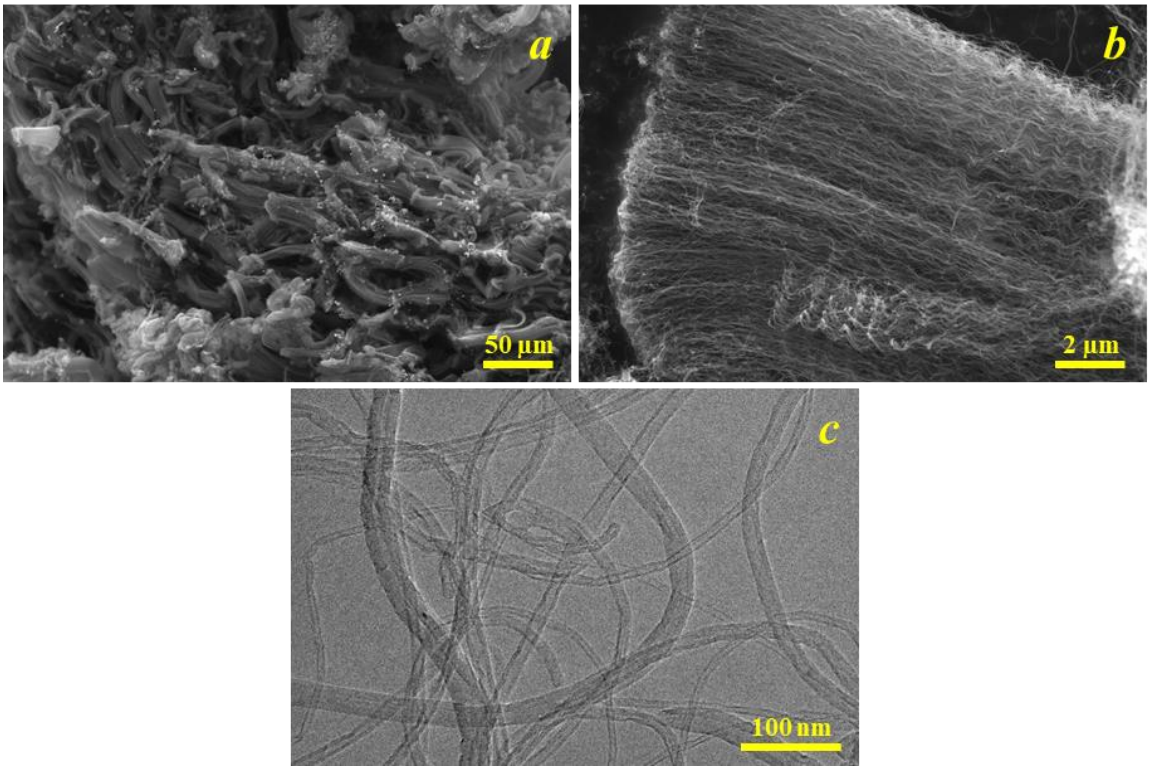

Figure 4: *(a-b) SEM and (c) TEM micrographs of ultrahigh aspect ratio CNTs synthesized on vermiculite supports.*

A variety of commercially available, short multiwalled carbon nanotubes were used as controls and comparisons to the laboratory grown ultrahigh aspect ratio MWCNTs: Nanocyl™ NC7000 (Nanocyl SA, Sambreville, Belgium), Baytubes® C150P (Bayer MaterialScience AG, Leverkusen, Germany), SMW200 (SouthWest Nanotechnologies, Norman, OK), and Cheap Tubes Short Multi Walled Carbon Nanotubes (Cheap Tubes Inc., Grafton, Vermont; referred to hereafter as CSCNT). Figures 5 and 6 display SEM and TEM micrographs of the commercial nanotubes, Table 1 presents the morphology of commercial and laboratory CNTs, and Figure 7 presents the diameter distributions of the CNTs.

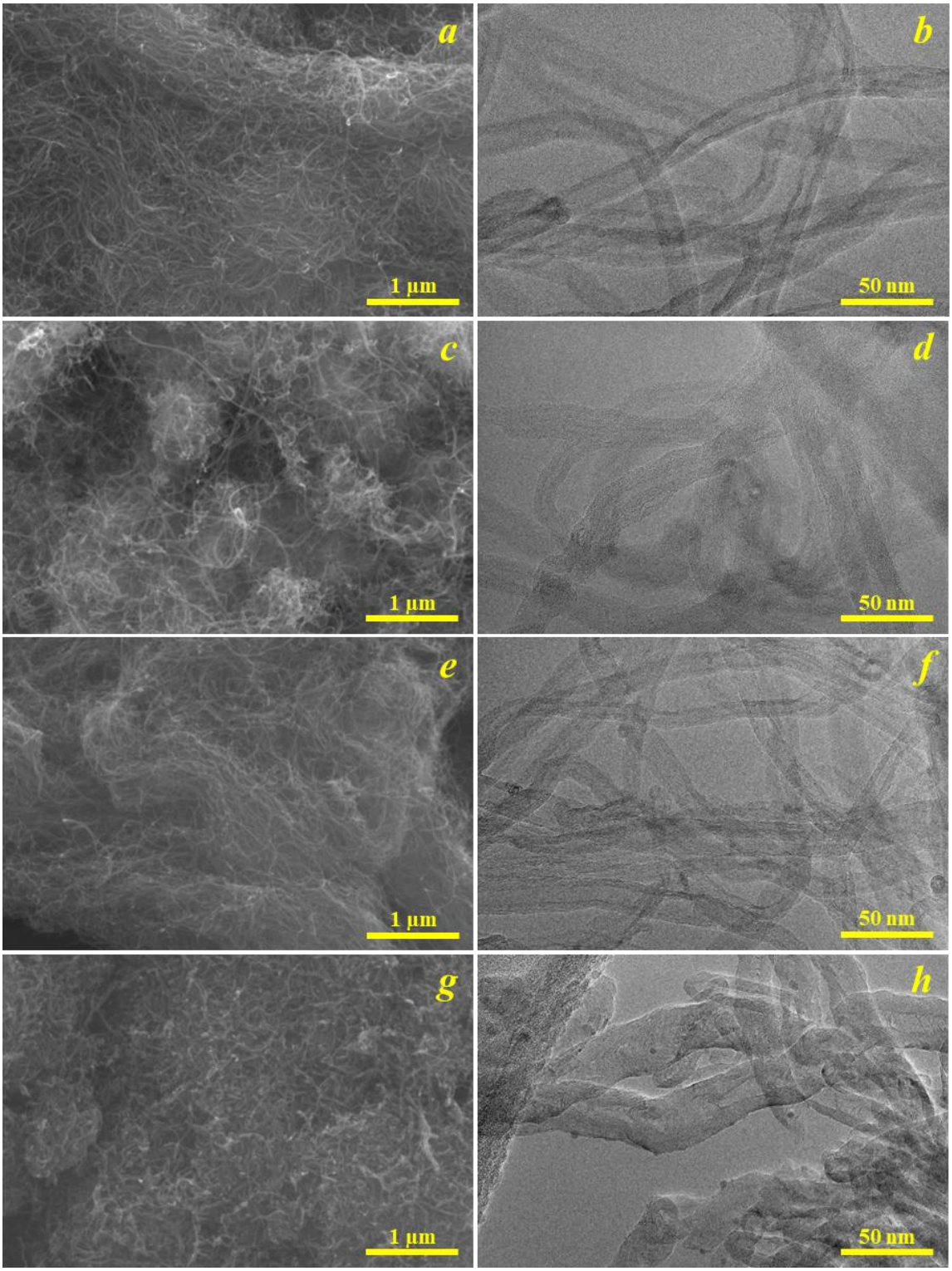

Figure 5: *SEM and TEM micrographs of (a-b) NC7000, (c-d) C150P, (e-f) SMW200, and (g-h) CSCNT.*

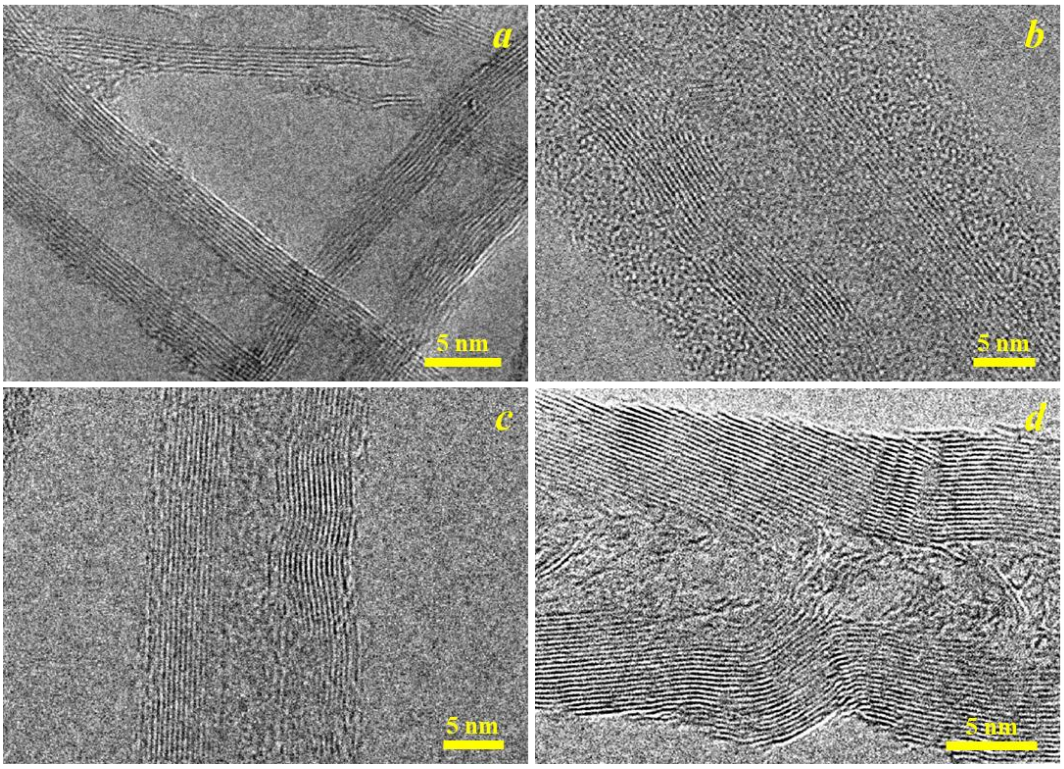

Figure 6: *High resolution TEM micrographs of (a) NC7000, (b) C150P, (c) SMW200, and (d) CSCNT wall morphology.*

Table 1: *Morphology of commercial and laboratory synthesized MWCNTs.*

MWCNT	Length (µm)	Diameter (nm)	*L/D*	Walls	Wall Morphology
VNT100	100	15 ± 6	6,667	14 ± 7	Parallel
NC7000	1.3	11 ± 3	118	9 ± 1	Parallel
C150P	0.8	14 ± 5	57	13 ± 2	Parallel
SMW200	2.1	11 ± 4	191	10 ± 1	Parallel
CSCNT	1.1	19 ± 4	58	17 ± 1	Cup stacked

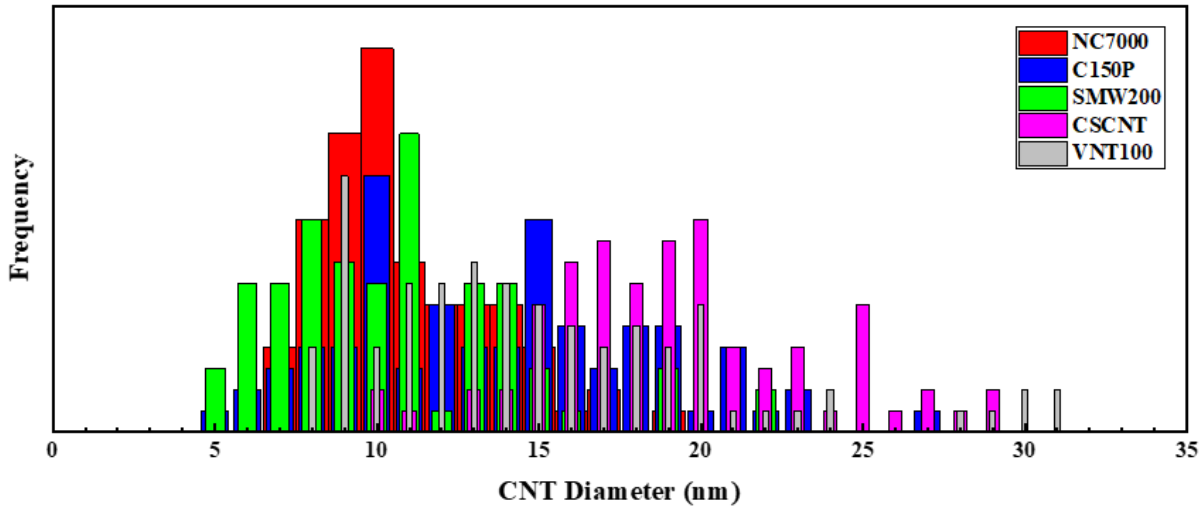

Figure 7: *Carbon nanotube diameter distributions measured by TEM.*

Makrolon® 2600 (M_w = 26,200 g/mol), an amorphous, medium viscosity polycarbonate, was obtained from Covestro. Duradene™ 706 SSBR, a polystyrene-butadiene (SBR) rubber, was provided by Lion Elastomers (Geismar, LA). Buna® CB 1203, a polybutadiene (BR) rubber, was provided by ARLANXEO (The Hague, Netherlands). Raven® 410 Ultra carbon black was obtained from Birla Carbon (Marietta, GA). General solvents (ethanol, chloroform, isopropyl alcohol, etc.), chemicals for carbon nanotube functionalization (ammonium carbonate, melamine, and sulfur), and additional components for rubber compounding (zinc oxide, stearic acid, paraffin oil, etc.) were obtained from Sigma Aldrich and Fisher Scientific.

2.2 Planetary ball milling

Ball milling was carried out with a Retsch PM100 Planetary Ball Mill. The Burgio-Rojac model of planetary ball milling was used to calculate the single impact energy, E_b, by the following

$$E_b = \frac{1}{2}\varphi_b\left(\rho_b\frac{\pi d_b^3}{6}\right)\omega_p^2\left[\left(\frac{\omega_v}{\omega_p}\right)^2\left(\frac{d_v-d_b}{2}\right)^2\left(1-2\frac{\omega_v}{\omega_p}\right)-2r_p\left(\frac{\omega_v}{\omega_p}\right)\left(\frac{d_v-d_b}{2}\right)-\left(\frac{\omega_v}{\omega_p}\right)^2\left(\frac{d_v-d_p}{2}\right)^2\right] \quad (9)$$

where φ_b is the obstruction factor, ρ_b is the density of the grinding balls, ω_p and ω_v are the rotational speeds (rad/s) of the sun wheel and grinding jar, respectively, d_v and d_b are the diameters of the grinding jar and grinding balls, respectively, and r_p is the radius of the sun wheel [82, 83, 109]. The extended velocity expression in the single impact energy equation derives from the difference between the launched velocity of a grinding ball due to rotation of the sun wheel/grinding jar and the velocity after an impact. Thus, E_b corresponds to the energy dissipated to the powder upon a single impact. While Equation 9 assumes a perfectly inelastic collision, corrections of collision elasticity can be made by multiplying the impact energy by a parameter K_a with a value between 0 and 1 indicating a perfectly elastic (K_a = 0) or perfectly inelastic (K_a = 1). However, this correction was not made in this study as free fall experiments with coated grinding balls have shown changes in collision elasticity to be inconsequential in the early stages of milling [86].

The obstruction factor is dependent on the degree of filling in the jar and is calculated by the following

$$\varphi_b = 1 - n_v^{\varepsilon} \tag{10}$$

where n_v is the fraction of filled space by grinding balls in the grinding jar and ε is a parameter dependent on the geometry of the mill.

$$n_v = \frac{N_b}{N_{b,v}} \tag{11}$$

$$N_{b,v} = \frac{\pi d_v^2 h_v}{4 d_b^3} \tag{12}$$

$$n_s = \frac{N_b}{N_{b,s}} \tag{13}$$

$$N_{b,s} = \frac{\pi (d_v - d_b) h_v}{3 d_b^2} \tag{14}$$

N_b is the number of grinding balls in the grinding jar and h_v is the height of the grinding jar. $N_{b,v}$ is the number of grinding balls in a cubic arrangement that would fill the grinding jar and $N_{b,s}$ is the number of grinding balls in a cubic arrangement that would cover one third of the inner surface area of the grinding jar. The value of parameter ε is evaluated from Equation 10 for $N_b = N_{b,s}$ that yields an obstruction factor of 0.95.

The cumulative energy of milling, E_{cum}, is the product of the single impact energy and the number of impacts over the milling period and is given by the following

$$E_{cum} = E_b v_t t \tag{15}$$

where v_t is the impact frequency and t is the milling time. The impact frequency is calculated by the following

$$v_t = N_b K \frac{\omega_p - \omega_v}{2\pi} \tag{16}$$

where K is an instrument parameter dependent on the geometry of the mill.

For all milling trials, an 80 mL stainless steel grinding vessel (d_v = 60 mm, h_v = 36 mm) was filled with one of two stainless steel (ρ_b = 7,760 g/cm^3) grinding media configurations (d_b = 10 mm and N_b = 25 or d_b = 20 mm and N_b = 5). The radius of the PM100 sun plate, r_p, is 70.5 mm, and the speed ratio, ω_v/ω_p, is -2. The geometric constant, K, has been found to be 1.5 for grinding balls 8-10 nm in diameter and was assumed to be similar for grinding balls of 20 mm in diameter given nearly equivalent obstruction factors of 0.9 [85].

The kinetic length reduction behavior of carbon nanotubes was first studied for the four short, commercial carbon nanotubes (NC7000, C150P, SMW200, and CSCNT) using only the 10 mm grinding media configuration. The effects of single impact energy were investigated by varying the rotational speed (ω_p) between 100 rpm and 600 rpm at a constant milling time of 30 min. The effects of cumulative impact energy were investigated by varying milling time between

5 min and 90 min at a constant rotational speed of 300 rpm. For all short, commercial CNT milling trials, sample mass was fixed at 400 mg. For NC7000, the additional effects of sample mass (1.2 g and 2.0 g) and bulk density (doubled original bulk density by dispersing NC7000s in water and evaporating; denoted by NC7000*) were studied.

After full investigation of ball milling effects on the short, commercial CNTs, the kinetic length reduction behavior of VNT100 were studied. The effects of single impact energy were investigated by varying the grinding media configuration (10 mm and 20 mm) and the rotational speed at a constant milling time of 30 min. The effects of cumulative impact energy were investigated by varying milling time up to 120 min at a constant rotational speed of 300 rpm using the 20 mm grinding media configuration. For all VNT100 milling trials, sample mass was fixed at 500 mg.

2.3 Mechanochemical functionalization

Mechanochemical functionalization of carbon nanotubes was carried out in a Retsch PM100 planetary ball mill in the presence of various functionalizing species as outlined in Table 2. First, the effects of milling VNT100 in the presence of ammonium carbonate were investigated. Dry mechanochemical functionalization was carried out by co-milling 500 mg VNT100 and 3.2 g ammonium carbonate. Aqueous mechanochemical functionalization was carried out by adding 50 mL water to the grinding vessel containing 500 mg VNT100 and 3.2 g ammonium carbonate, yielding a 0.65 M ammonium carbonate solution. In both cases, the carbon nanotube to ammonium carbonate ratio was 1:6.4, which is the same as conducted previously in similar studies [110]. The effects of rotational speed (300-600 rpm) and milling time (0.5-24 hr) were investigated. The grinding media configuration was fixed at five 20 mm grinding balls. After milling, the grinding

jar was placed in a fume hood for 1 hr to remove volatiles. Milled CNTs were purified by filtering through 0.22 μm filter paper.

Table 2: *Mechanochemically functionalized CNT specifications and nomenclature.*

Functional Species	CNT	Milling Conditions			Nomenclature
		ω_p (rpm)	t (hr)	N_b x d_b	
Ammonium carbonate	VNT100	300-600	0.5-4	5 x 20 mm	dfVNT afVNT
Melamine	NC7000	300	0.5-4	25 x 10 mm	melNC
Sulfur	VNT100 NC7000	300	1	5 x 20 mm	sVNT sNC

Non-covalent mechanochemical functionalization of carbon nanotubes was carried out by co-milling 500 mg NC7000s and 500 mg melamine. The effects of milling time at constant rotational speed (300 rpm) were investigated. The grinding media configuration was fixed at 25 10 mm grinding balls. Milled CNTs were dispersed in water by magnetic stirring to dissolve free melamine and filtered through 0.22 μm filter paper.

Mechanochemical functionalization of carbon nanotubes with sulfur was carried out by co-milling CNTs (both NC7000 and VNT100) with elemental sulfur (S_8). Milling conditions were fixed at 300 rpm for 1 hr using the 20 mm grinding media configuration. Initial investigations for the characterization of sulfur-functionalized CNT surface chemistry were done on CNTs milled at a 1:1 mass ratio with sulfur. Milled CNTs were dispersed in carbon disulfide by magnetic stirring for 30 min under slight heating to dissolve free sulfur and filtered through 0.22 μm filter paper.

However, for subsequent use of sulfur-functionalized CNTs in rubber compounds, CNTs were milled with sulfur at different mass ratios (6:1.75 and 12:1.75; discussed later) at the same previous milling conditions, and the composite CNT-powders were left unpurified before compounding with rubber.

2.4 Carbon nanotube characterization

Scanning electron microscopy (SEM) on carbon nanotubes was carried out using a Thermo Scientific Quattro S ESEM. To characterize bulk carbon nanotube morphology, dry CNT powders were sprinkled onto carbon tape adhered to a SEM stub. The lengths of very long carbon nanotubes (average length much greater than 5 μm) were measured from SEM micrographs of CNT bundles in the dry bulk phase. The average lengths of these nanotube samples were taken as the average of at least 20 individual bundle length measurements. For more accurate length characterization of short nanotubes (average length less than 5 μm), CNT powder was dispersed in a suitable solvent at approximately 0.1 g/L and sonicated for 3 minutes. Solvent-CNT compatibility testing was conducted by trial and error and assessed qualitatively based on stability of CNT dispersion; chloroform was used as a suitable dispersing agent for NC7000, C150P, and SMW200 while isopropyl alcohol was used for CSCNT and VNT100. A drop of the resulting dispersion was pipetted onto a polished silicon wafer adhered to a SEM stub by carbon tape. The stub was then placed in a vacuum to remove excess solvent. The average lengths of these nanotube samples were taken as the average of at least 100 individual CNT length measurements. For individual carbon nanotubes that were too long to be imaged in one micrograph, multiple micrographs were obtained to encompass the entire CNT length, and the micrographs were stitched together using image processing software. Transmission electron microscopy on carbon nanotubes was carried out using

a JEOL 2010F FE-S/TEM. For CNT diameter measurement and wall morphology characterization, powders were ultrasonically dispersed and pipetted onto lacey carbon copper grids. The average diameters of nanotube samples were taken as the average of at least 80 individual CNT diameter measurements. ImageJ image processing software was used for all quantitative assessment of CNT lengths, diameters, and number of walls.

Bulk electrical conductivities of carbon nanotubes were measured with a custom-built resistivity cell using a four-point measurement to reduce the effects of contact resistance. Two brass electrodes were machined to fit into an insulating acrylic cylindrical casing. Carbon nanotube powder was packed into the insulating casing, and the top electrode was placed on top with a 2 kg weight to compress the powder to a pressure of 200 kPa. Current was supplied and resistance was measured by a Keithley 2000 Multimeter. A total of four conductivity measurements were taken for each CNT sample.

Thermogravimetric analysis (TGA) was carried out using a TA Instruments TGA 550. Approximately 5 mg CNTs were placed in an aluminum pan and heated from 30 °C to 800 °C at 10 °C/min under nitrogen atmosphere. Degradation temperatures, T_d, associated with surface group desorption and/or decomposition and CNT backbone decomposition were taken as the peak of the derivative curve (inflection point of the weight loss curve).

Fourier transmission infrared spectroscopy (FTIR) was carried out using a Nicolet iS50R FT-IR with a diamond crystal. Approximately 2 mg CNTs were pressed into the crystal under light pressure from a flat tip, ensuring full sample-crystal contact. Spectra were acquired over 400-4000 cm^{-1} wavenumbers and scans were averaged over 64 accumulations. Peaks were identified and analyzed using OMNIC™ software.

Raman spectroscopy was carried out using a Renishaw inVia^{TM} Confocal Raman Microscope with a 532 nm laser. The Raman peaks of interest for this study were the G band centered around 1565-1585 cm^{-1} and the D band centered around 1330-1350 cm^{-1}. The G band is indicative of graphitic sp^2 hybridization, while the D band is related to defects in graphitic structures. The ratio of the D band to G band peak areas, notated as I_D/I_G, was used as a measure of the defect density in the carbon nanotube sample. I_D/I_G values approaching infinity indicate a high defect density, while I_D/I_G values approaching zero indicate a low defect density. Peak areas were obtained from the integrated WiRE^{TM} software after performing baseline subtraction, normalization, and curve fitting on each individual spectrum. At least four spectra were taken from different locations on each sample, and I_D/I_G was taken as an average of the individual spectra.

X-ray photoelectron spectroscopy (XPS) was carried out by Dr. Mourad Benamara (Data acquisition only) at the University of Arkansas Nano & Bio Materials Characterization Facility using a PHI Versaprobe II Hybrid with a Al Kα beam. Full spectral scans (0-1100 eV) were carried out at 1 eV resolution, and 0.2 eV resolution scans were carried out for C1s, O1s, N1s, and S2p core levels. Peak deconvolution and area analysis was carried out using OriginPro software; all peaks were assumed to be Gaussian and a Shirley background was applied in all cases.

2.5 Polycarbonate compounding

A DSM Xplore 5 cm^3 conical twin screw micro compounder was used to prepare polycarbonate-carbon nanotube (PC-CNT) composites with CNT contents between 0.1 wt% and 5.0 wt%. The screw torque and melt viscosity were recorded during compounding using proprietary Xplore Micro Compounder software. Before compounding, PC beads and CNT powders were premixed so that the latter was well distributed in the former and dried overnight in

a vacuum oven at 80 °C. PC beads and CNT powder were simultaneously fed to the mixer in small amounts over a one-minute period, and the mixing time was started after all material had been injected. All composites were compounded at 200 rpm (shear rate of 53 s^{-1}) for 4 min at 280 °C. This temperature has been used previously for compounding CNTs in PC and is thought to represent the best tradeoff between viscosity and degradation [60, 65]. Similar mixing conditions, particularly the high-end rotational speed, have been shown to result in good CNT dispersion, resulting in low percolation thresholds [111]. The mixing time was chosen as the shortest time where the torque was roughly constant; the first 5-10 sec of mixing time was removed from recorded compounding data due to torque/viscosity readout instability. Extruded strands were pelletized by hand and compression molded at 280 °C for 5 min under ~5 MPa followed by cooling under pressure to near room temperature using a Carver Laboratory press. Polyimide film sprayed with Easy Release™ 200 general purpose release agent was applied above and below the sample to prevent the sample from sticking to the molding equipment. Air bubbles were removed from compression molded specimens by applying and releasing pressure multiple times before starting the 5 min molding process.

Table 3 presents composite nomenclature and CNT specifications. The number next to each VNT label corresponds to the average length of the sample in μm. Due to feed hopper volume constraints and the low bulk density of VNT100, the maximum VNT100 content in PC was limited to 2 wt%. Thus, a very low milling single impact energy, 3.5 mJ/impact (100 rpm with 10 mm grinding balls), was used to modify the bulk density of pristine VNT100 while retaining nanotube length to allow for greater than 2 wt% nanotube incorporation; these nanotubes are hereafter referred to as VNT100*. All other plain milling of VNT nanotubes were carried out using the 20 mm grinding media configuration. Dry mechanochemically functionalized (dfVNT5) and aqueous

mechanochemically functionalized (afVNT20) were subject to the same milling conditions (300 rpm for 36 min with 20 mm grinding balls) as mVNT5. Theoretical percolation thresholds were calculated by Equation 4 assuming PC and CNT specific gravities of 1.2 and 1.8, respectively. It should be noted that milling conditions were determined after full analysis of length reduction kinetics and mechanochemical functionalization effects. NC7000 CNTs were used as a low aspect ratio, commercial comparison to the laboratory synthesized CNTs.

Table 3: *PC composite nomenclature and CNT specifications.*

Composite	Milling Conditions			*L/D*	$\varphi_{c,theo}$ (wt%)
	ω_p (rpm)	t (min)	N_b x d_b		
PC-VNT100	-	-	-	6,667	0.01
PC-VNT100*	100	30	25 x 10 mm	6,667	0.01
PC-mVNT50	300	8	5 x 20 mm	3,333	0.02
PC-mVNT20	300	20	5 x 20 mm	1,333	0.06
PC-afVNT20	300	36	5 x 20 mm	1,333	0.06
PC-mVNT5	300	36	5 x 20 mm	333	0.24
PC-dfVNT5	300	36	5 x 20 mm	333	0.24
PC-NC7000	-	-	-	118	0.66

2.6 Polycarbonate composite characterization

CNT agglomeration in PC composites was characterized by optical microscopy. Thin (0.3 mm) compression molded discs were imaged with a Leica SP8 Confocal Laser Scanning Microscope using a 532 nm laser in transmission mode. To ensure optical transparency of samples,

only composites with 0.1 wt% CNTs were imaged. ImageJ image processing software was used to quantify CNT agglomerate size, and average agglomerate sizes for each sample were taken as the average of at least 50 individual CNT agglomerate diameter measurements. The dispersion of individual CNTs in the PC composites was characterized by SEM. Thin (0.3 mm) compression molded discs were lightly scored with a razor blade, submerged in liquid nitrogen for ~5 min, and fractured manually to obtain clean cross-sectional surfaces for imaging. The cross-sectional surfaces were sputter coated with a thin layer of iridium and placed in a Thermo Scientific Quattro S ESEM for imaging.

Bulk electrical conductivities of PC-CNT composites were characterized by two different methods. For composites with bulk electrical resistivities less than 10^7 Ω·cm, a four-point probe method was used. Four copper wire leads were attached equidistantly along compression molded composites (30 mm L x 10 mm W x 0.3 mm H) using conductive silver epoxy. Current and voltage were supplied to the outer and inner leads, respectively, using a Keithley 2000 Multimeter, and the resistance was measured. Resistance measurements were repeated for four different samples. The resistivity was calculated as

$$\rho = \frac{RHW}{D} \tag{17}$$

where R is the measured resistance, H is the sample thickness, W is the sample width, and D is the distance between the inner leads. For composites with bulk electrical resistivities greater than 10^7 Ω·cm, a two-point sandwich method was used. Compression molded discs (63 mm D x 1.5 mm H) were placed in a Keithley 6105 Resistivity Adapter between two stainless steel electrodes. Voltage was supplied by an ISCO Model 495 Power Supply and current was measured by a Keithley 6485 Picoammeter. For each sample, the current measurement was carried out twice on each side (four times total). The composite resistivity was calculated as

$$\rho = \frac{22.9V}{HI} \tag{18}$$

where V is the supplied voltage, I is the measured current, and H is the sample thickness.

Rheological properties of PC-CNT composites were measured using a TA Instruments Ares-G2 Rheometer. Compression molded discs (25 mm diameter x 1 mm thickness) were placed between two parallel plate fixtures and soaked at 280 °C for two minutes to allow the sample to reach testing temperature. Oscillation frequency sweeps from 600 to 0.1 rad/s at 5% angular strain were carried out isothermally at 280 °C.

Thermal properties of PC-CNT composites were characterized by TGA and differential scanning calorimetry (DSC). A TA Instruments TGA 550 was used to determine the thermal stability of PC-CNT composites. For a given sample, a ~5 mg pellet was placed in an aluminum pan and heated from 40 °C to 800 °C at 10 °C/min in nitrogen atmosphere, and the degradation temperature, T_d, was taken as the peak of the derivative of the weight loss curve. The glass transition temperature, T_g, and change in heat capacity at the glass transition, ΔC_p, were characterized by a TA Instruments DSC2500. Temperature calibration was via indium, tin and biphenyl while heat capacity calibration was via sapphire. After melting samples in the DSC pan and cooling at 80 °C/min, composites were heated from 40 °C to 250 °C at 10 °C/min, and the glass transition was taken as the fictive temperature, following the procedure described previously [112], to eliminate the effect of enthalpy relaxation. Five different measurements were made on five different processed PC samples to calculate the reproducibility of the various quantities (T_d, T_g, and ΔC_p); no dependence of reproducibility on sample identity was assumed.

Tensile mechanical properties of PC-CNT composites were characterized using a United Testing Systems SSTM tensile testing machine. Compression molded composites (0.3 mm thickness) were cut into microtensile dogbone specimens according to ASTM D1708 using a

Dewes Gumbs Die Co. Model 1.5T Expulsion Press. Specimens were fixed using pneumatic grips under no preload and extended at 0.5 in/min until break. For each composite, tensile tests were conducted on five different specimens, and the tensile strength, Young's modulus, and failure strain were taken as the average of the five tests.

2.7 Rubber compounding

Rubber composites were compounded using a Brabender Type 6 Mixer (60 cm^3) with roller blades connected to an Intelli-Torque Plasti-Corder® drive. Compounding temperature was 60 °C and blade rotational speed was 40 rpm. While the Type 6 mixer cannot be directly equated to a internal mixer used in industrial rubber compounding due to the absence of a ram, these mixing conditions (temperature and blade rpm) are in the typical range for similar compounds [113-115]. Batch size was kept constant at 42 g (~70% degree of filling). The rubber base was first added to the mixer and masticated for 1 min. Then, the fillers, processing aid, activators, antiozonant, and antioxidant were added to the mixer and compounded for 6 min. Due to feeding zone constraints, the total feeding time for these components took approximately 1 min, and the 6 min compounding time started after all components had been added. Finally, sulfur and accelerator were added to the mixer and compounded for 2 min before ending the compounding process. Thus, the total compounding time was 10 min for all rubber compounds, which is comparable to most commercial rubber compounding processes. For compounds containing sulfur functionalized CNTs, the unpurified milled composite CNT-sulfur powders were added with the rest of the components after mastication, and only the accelerator was added for the last 2 min of mixing.

Table 4 presents a typical passenger tire tread compound with carbon black filler and serves as the basis for which all rubber compounds in this study are derived [116]. To determine the effect

of filler content and type, the total filler content was varied between 12 and 72 phr. Carbon black (CB), NC7000 (NC), and VNT100 (VNT) were used as different filler types, primarily to determine the effects of filler aspect ratio. The effect of dual filler systems with varying ratios of CB to CNT (for example, notated as 48CB:6NC for 48 phr carbon black and 6 phr NC7000) was also investigated. Additionally, sulfur functionalized CNTs (sNC and sVNT) were compared to their unfunctionalized counterparts in select compounds (48CB:6sNC, 48CB:6sVNT, and 12sNC). As mentioned previously, these milled composite CNT-sulfur powders were left unpurified after milling, and the CNT-sulfur milling ratio was chosen such that the total sulfur content was the same in each compound (6:1.75 for 6 phr CNT and 12:1.75 for 12 phr CNT). In all cases, the content of all other components was kept constant.

Table 4: *Control passenger tire tread rubber compound.*

Component	Purpose	phr
Poly(styrene-butadiene) (SBR)	Rubber	60
Polybutadiene (BR)	Rubber	40
Carbon black (CB)	Filler	72
Paraffin oil	Processing aid	37
Zinc oxide	Activator	3
Stearic acid	Activator	2
N-(1,3-dimethylbutyl)-N′-phenyl-p-phenylenediamine	Antiozonant	2
Polymerized 1,2-dihydro-2,2,4-trimethylquinoline	Antioxidant	2
Sulfur	Vulcanizing agent	1.75
N-oxydiethylene-2-benzothiazole sulfonamide	Accelerator	0.75

2.8 Rubber compound characterization

The curing kinetics of rubber composites was studied using an Alpha Technologies ATD 1000 Rheometer. Approximately 4.5 g uncured rubber compound was compressed between grooved platens and held isothermally at 160 °C. The torque was measured as the sample was subject to oscillation by the bottom platen grooves (0.5° shear angle at 1.67 Hz). The vulcanization time for a sample was taken as t_{97}, which is the time required to reach 97% of the maximum torque. For subsequent characterization of cured rubber, compounds were vulcanized isothermally at 160 °C under ~10 MPa for the designated t_{97} time with a Carver Laboratory press. Polyimide film sprayed with Easy Release^{TM} 200 general purpose release agent was applied above and below the sample to prevent the sample from sticking to the molding equipment.

Tensile mechanical properties of rubber composites were characterized using a United Testing Systems SSTM tensile testing machine. Vulcanized rubber sheets (10 cm x 6 cm x 1 mm) were cut into microtensile dogbones according to ASTM D1708 using a die cutter. Samples were fixed using pneumatic grips under no preload and extended at 0.5 in/min until break. For each compound, tensile tests were conducted on five different specimens, and the tensile strength, Young's modulus, and failure strain were taken as the average of the five tests.

Dynamic mechanical analysis was carried out on rubber specimens using a TA Instruments Ares-G2 Rheometer with a linear tension fixture. Strip specimens (40 mm x 5.2 mm x 1 mm) were cut from vulcanized rubber sheets using a die cutter. The sample was stretched from an initial 5 mm gap to an initial force of 2 N and cooled to -80 °C. The sample was then heated from -80 °C to 100 °C while subject to linear tension oscillation (0.1% strain at 10 Hz). Data was recorded in 3 °C temperature steps.

Abrasion resistance of rubber composites was characterized using a homemade wear tester. A GardCO D12V Linear Washability and Wear Tester was retrofitted with a 100-grit sandpaper base and a rubber specimen (20 mm diameter x 10 mm thickness) holder. The test piece was pressed against the abrasion medium at a force of 10 N. The speed setting was selected such that the average velocity throughout testing was nearly 1 ft/s (~0.3 m/s), and the number of cycles was set to give a total abrasion path of 40 m. Test conditions were best selected to adhere to ASTM D5963. Specimen mass was measured before and after testing to determine mass loss from abrasion, and an average of four tests was used for each sample.

Chapter 3: Carbon nanotube aspect ratio modification by planetary ball milling

3.1 Low aspect ratio carbon nanotubes

3.1.1 Minimum single impact energy

The length reduction of four short, commercially available nanotube samples with respect to increasing rotational speed, and consequently increasing single impact energy, at constant milling time is shown in Figure 8. Length reduction behavior of NC7000 shows no significant differences among different sample masses and different initial bulk densities. The invariance of length differences with powder mass is not surprising. Magini et al. [86] stated that milling powder forms a coating on all surfaces of grinding balls and walls during the early stages of milling, and collisions between these balls entrap all the powder within the collision radius. Varying the sample mass effectively changes the coating thickness of the surfaces inside the grinding jar, and the results show that the breaking efficiency of these impacts is sufficient to break the nanotubes trapped in the collisions for even the thickest coating in this study. Another critical assumption is that the entire powder sample is coating a surface, and there is no unfixed powder in the jar during milling. Deviations on this assumption would likely result in less nanotube breakage as this free moving powder does not participate in the collisions. However, visual observations of the nanotube powder in the grinding jar after milling validates the assumption that little to no free moving powder exists under the conditions used in our experiments.

Length reduction behavior of NC7000, SMW200, and C150P are all very similar. A distinct horizontal step at low impact energies is followed by an exponential-type length decrease. Clearly, these nanotubes possess a minimum single impact energy, $E_{b,min}$, for which under that impact energy, no significant length reduction has occurred, and above that impact energy, fracture does occur. For NC7000 and SMW200, the minimum impact energy appears to be 10 mJ/impact,

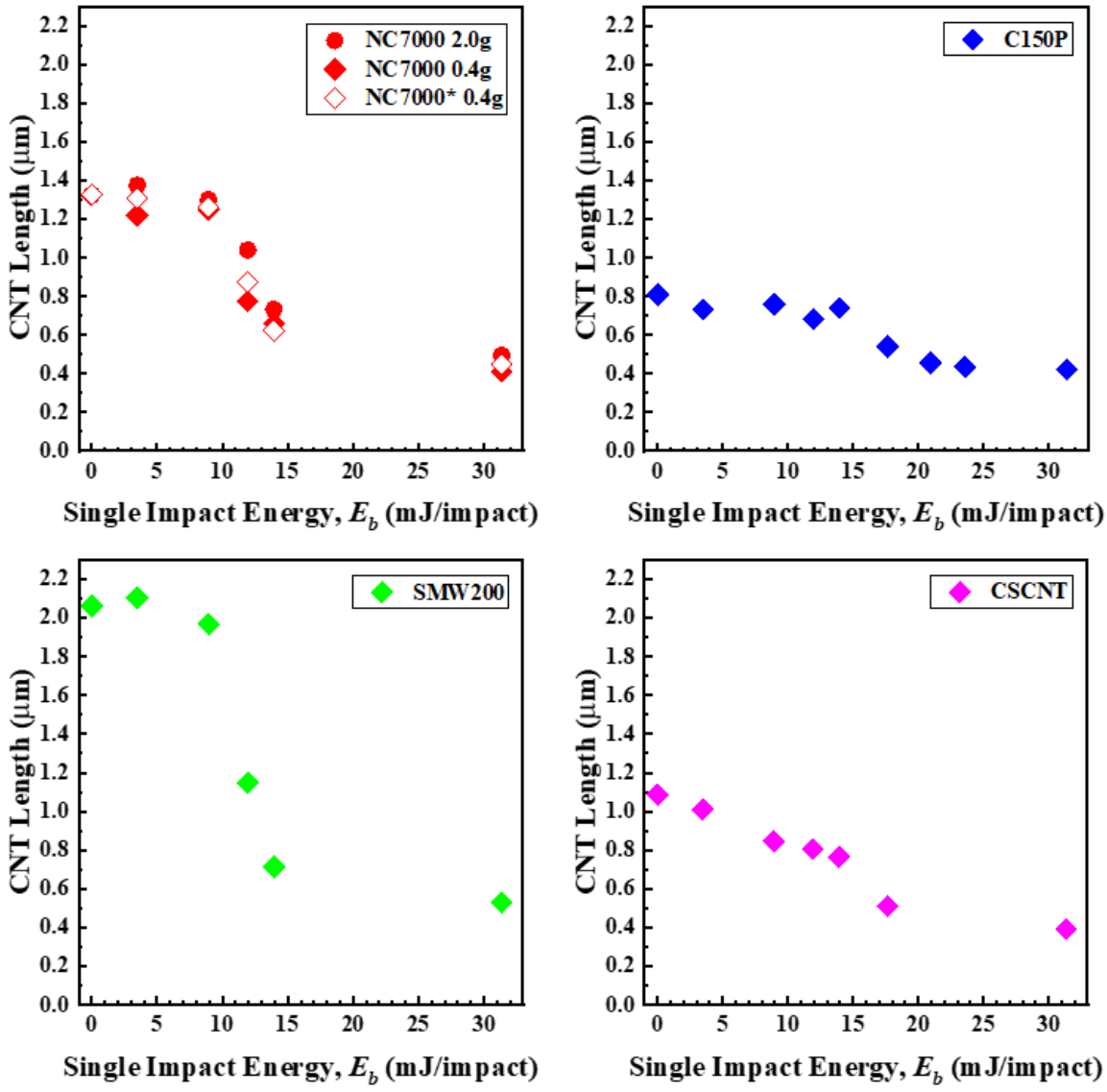

Figure 8: *Carbon nanotube length reduction with respect to single impact energy.*

while the minimum impact energy for C150P is 15 mJ/impact. This result suggests that the minimum energy for breakage of carbon nanotube is dependent on the diameter or number of walls. NC7000 and SMW200 both have very similar average diameters and number of walls and show similar minimum impact energies, while C150P has a larger diameter and number of walls and has a larger minimum impact energy. This increase is likely consistent with the findings of

Kozma et al. [90], who found that nanotubes of 30 nm in diameter possess a minimum single impact energy of 35 mJ/impact. The linear relationship between parallel walled nanotube diameter and is presented in Figure 9. TEM micrographs confirm that ball milling did not reduce carbon nanotube diameter for any of the nanotubes. This result is consistent with most studies [81], but others have shown high energy ball milling can result in partial wall damage or complete destruction of nanotubes [117].

The length reduction behavior of CSCNT has a somewhat different form than the other three commercial nanotubes. While there does appear to be a notable drop in length near 15 mJ/impact for CSCNT, data points under 15 mJ/impact display a linear type length reduction from 1.1 μm to 800 nm. This extent of length reduction at low single impact energies is greater than the other three CNTs studies, suggesting CSCNT likely possesses a minimum single impact energy below the 3.5 mJ/impact (lowest impact energy applied). This phenomenon could be explained by TEM micrographs of the virgin tubes shown previously in Figures 5 and 6 in which wall damage and alternative nanotube morphologies were seen. CSCNT nanotubes possess a high concentration of wall damage and dislocations compared to the other three nanotube samples. The presence of wall damage likely weakens the structural integrity of the nanotubes, leading to a reduced minimum impact energy. These defects could be a byproduct of the industrial synthesis process or of milling performed by the manufacturer to separate the nanotubes from the catalyst and support materials. Also, many nanotubes within the TEM micrographs appeared to have a cup-stacked or bamboo-like morphology. These layers could be more easily sheared apart due to open ends on the nanotube surface, also leading to lower ball impact energies required to fracture the nanotube. Linear length reduction with respect to increasing impact energy as found with CSCNT was consistent with the findings of Kozma et al. [90]. However, they identified the minimum with

Raman spectroscopy rather than with length measurements. The initial carbon nanotube product possessed a low concentration of defects, and there was a marked increase in I_D/I_G at 35 mJ, indicating an increase in sp^3 hybridized carbons. This observation was used as justification for identifying the minimum energy despite the length having already been reduced by nearly 50%.

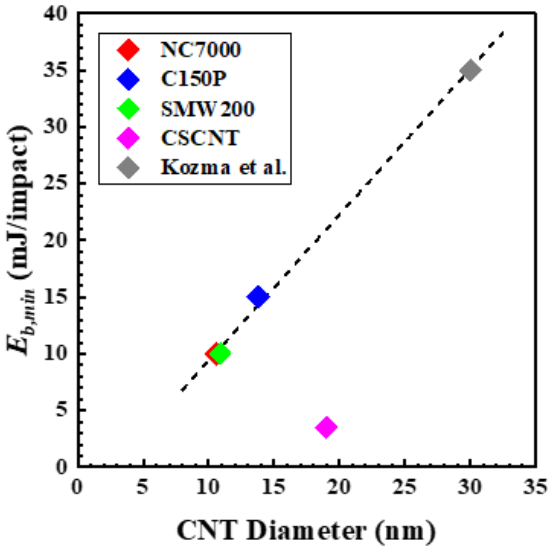

Figure 9: *Relationship between CNT diameter and minimum single impact energy for the four, short commercial carbon nanotubes and another parallel-walled CNT sample previously studied by Kozma et al. [90].*

Raman spectra and I_D/I_G values corresponding to the milled CNT samples in Figure 8 are given in Figure 10. Variations in the peak ratio have no clear correlation with average nanotube length considering the measured standard deviation of was generally around ± 0.1. For this peak ratio to be a proper measure of minimum impact energy determination, it would be expected that a distinct increase in I_D/I_G occurs when the average length of the CNTs reduces significantly. A primary concern was that nanotube healing may have occurred after ball milling of the nanotubes

and before Raman spectra acquisition (ball milling and spectra acquisition occurred months apart). To eliminate the possible effect of nanotube healing, Raman spectra of freshly milled NC7000s under the same conditions as stated for Figure 8 were acquired, and no appreciable changes in the spectra or peak ratios were observed.

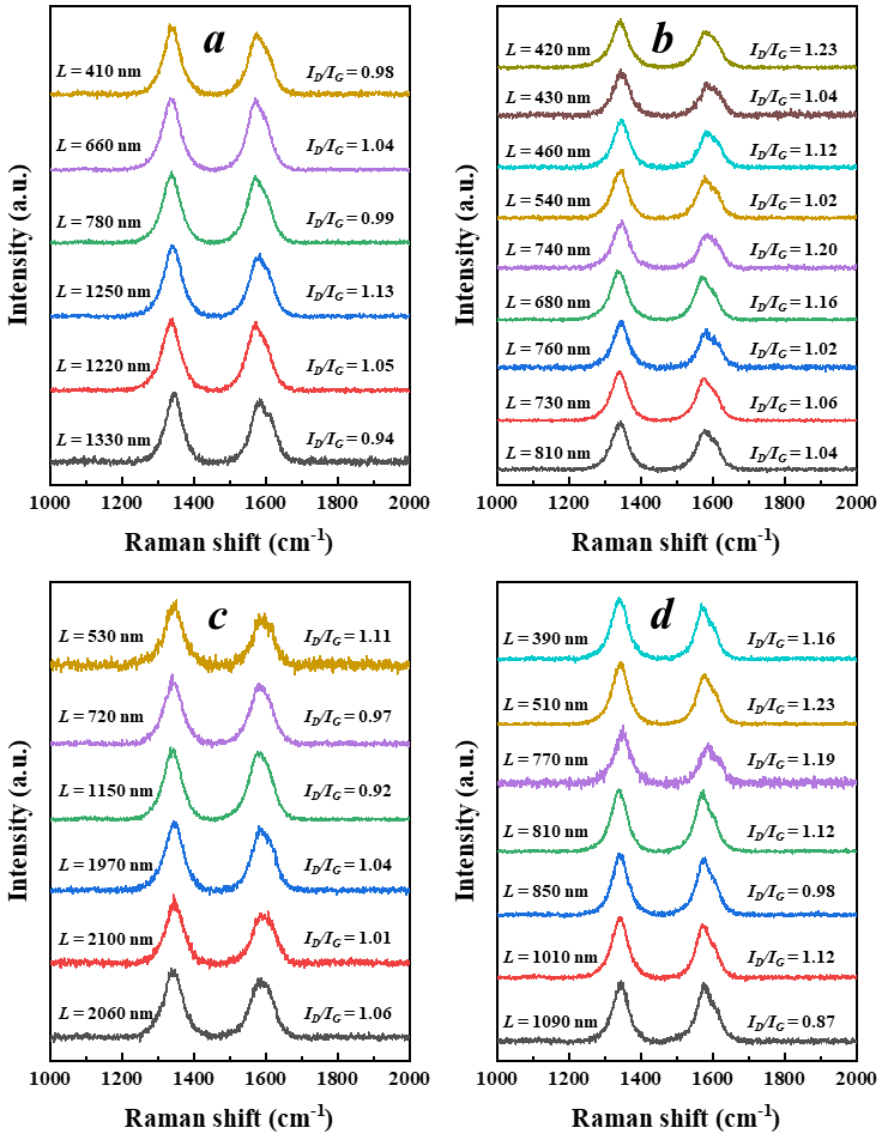

Figure 10: *Raman spectra of 0.4 g milled (a) NC7000, (b) C150P, (c) SMW200, and (d) CSCNT. Lengths correspond to data points in Figure 8 and I_D/I_G values are an average of five spectra.*

It is assumed that defect dense nanotube ends account for a large portion of the D band detected by Raman spectroscopy. Assuming the defect dense length of a nanotube accounts for 5 nm on each nanotube end, then for unmilled NC7000 (~1330 nm) approximately 0.8% percent of the nanotube length is defect dense. For NC7000 milled to their terminal length (~410 nm), the defect dense length fraction increases to approximately 2.4%. A marginal increase in defect dense length is not likely to produce notable changes in the Raman shift, so the peak ratio values obtained in this study are likely within the margin of error. However, we recognize that nanotube samples may experience wall damage and amorphization contributing further to D band amplification. Thus, we believe that length measurements should be the primary method of identifying the minimum single impact energy since $E_{b,min}$ has been defined as the energy required to fracture a nanotube into shorter segments.

3.1.2 Length reduction kinetics

To obtain a range of cumulative impact energies, the rotational speed of the mill was kept constant at 300 rpm, corresponding to a single impact energy of 31 mJ/impact, and the milling time was varied. The length reduction of NC7000 (0.4g trials) is evident based on the SEM micrographs given in Figure 11 and the corresponding length distributions, along with log-normal fit and distribution parameters μ and σ, given in Figure 12. Unmilled NC7000 nanotubes are clearly the longest upon visual observation and have the widest distribution of lengths. Some nanotubes on the order of 4-5 μm in length span a large portion of the field of view, and in many cases image stitching was necessary to measure full nanotube lengths. At 20 minutes of milling, all nanotubes appear to be at or below 2 μm in comparison to the scale bar shown, and this observation is reinforced by the length distribution given in Figure 12c. At 30 minutes of milling,

the distribution becomes very narrow and no further significant length reduction was seen. The goodness of the log-normal fit is most evident at higher milling times. Although the fits are not shown here, this same log-normal function type was able to fit the length distribution of all nanotubes well at higher milling times. Length reduction upon milling of all nanotubes tested in this study follow this same qualitative pattern with time. The tendency for ball milled carbon nanotubes to converge to a log-normal distribution has been shown previously [118], but other fits such as the Weibull distribution have been observed [119].

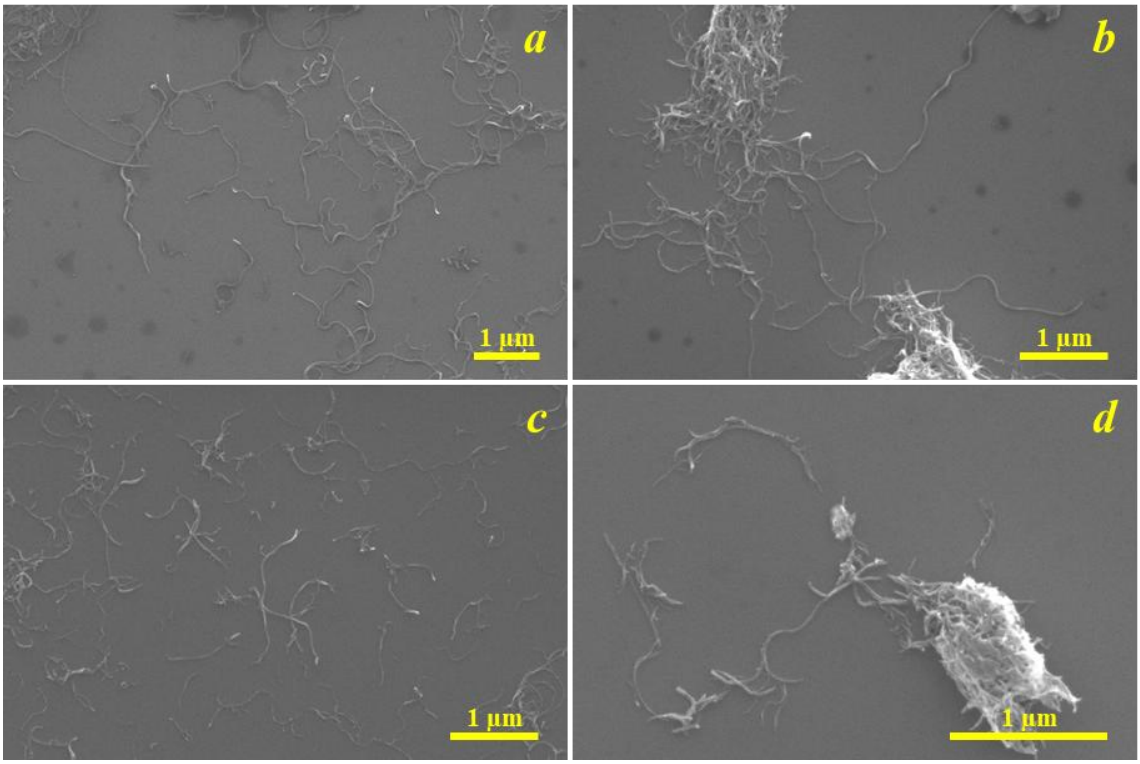

Figure 11: *SEM micrographs of (a) pristine NC7000 and 0.4 g trial milling times of (b) 10 min, (c) 20 min, and (d) 30 min.*

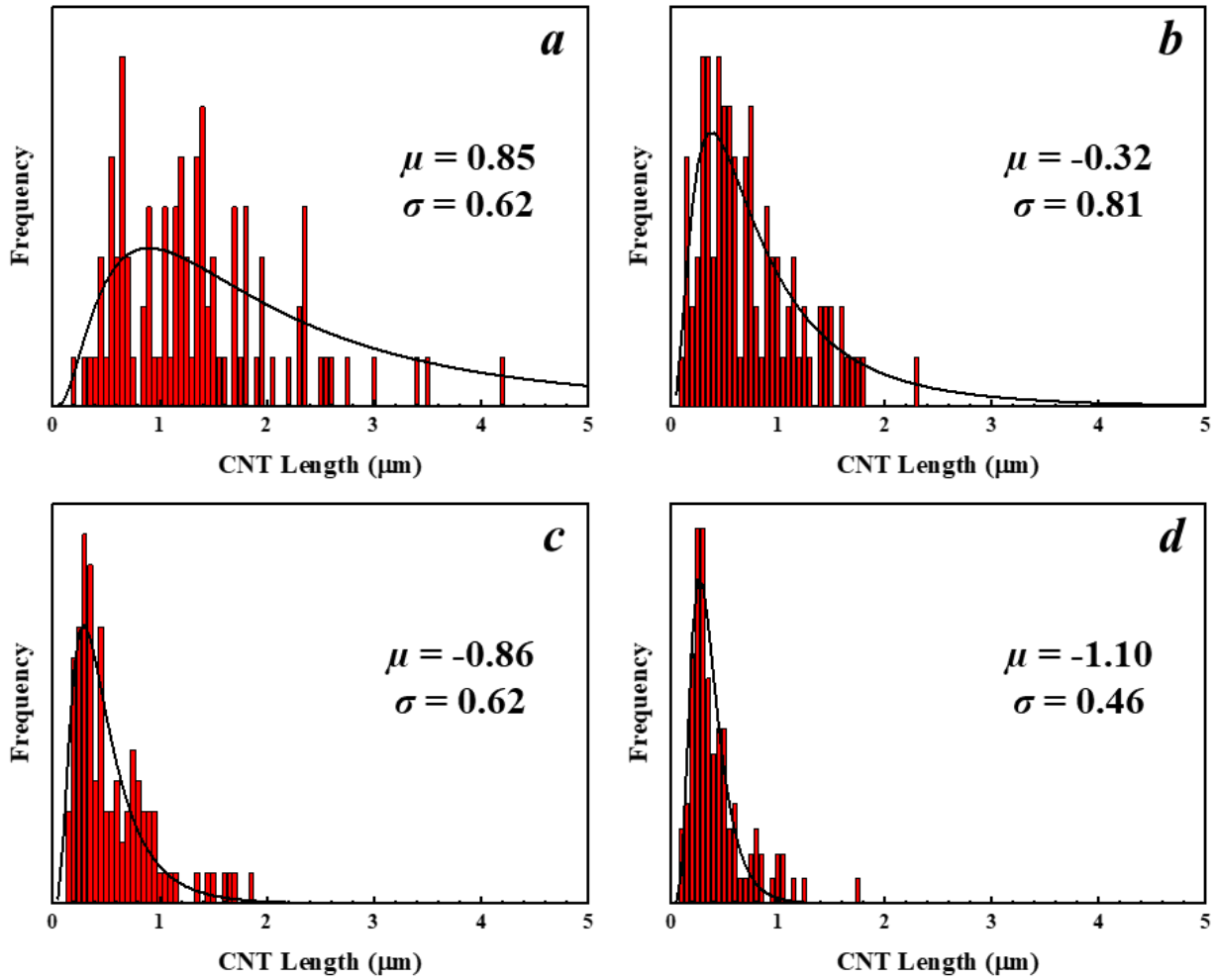

Figure 12: *Length distributions of (a) pristine NC7000 and 0.4 g trial milling times of (b) 10 min, (c) 20 min, and (d) 30 min with corresponding log-normal distribution parameters.*

Length reduction behavior of the four commercial carbon nanotube samples with respect to increasing cumulative impact energy is shown in Figure 13. The length reduction behavior of NC7000 shows no variance among the different sample masses and initial bulk densities. The appearance of a terminal length around 400 nm is consistent with the results of the curve shown in Figure 8. Also, the fact that changes in sample mass do not change the length reduction behavior with respect to cumulative energy validates the use of the non-mass averaged cumulative energy

expression given in Equation 15 as opposed to a mass averaged cumulative energy expression most often used elsewhere [90, 109].

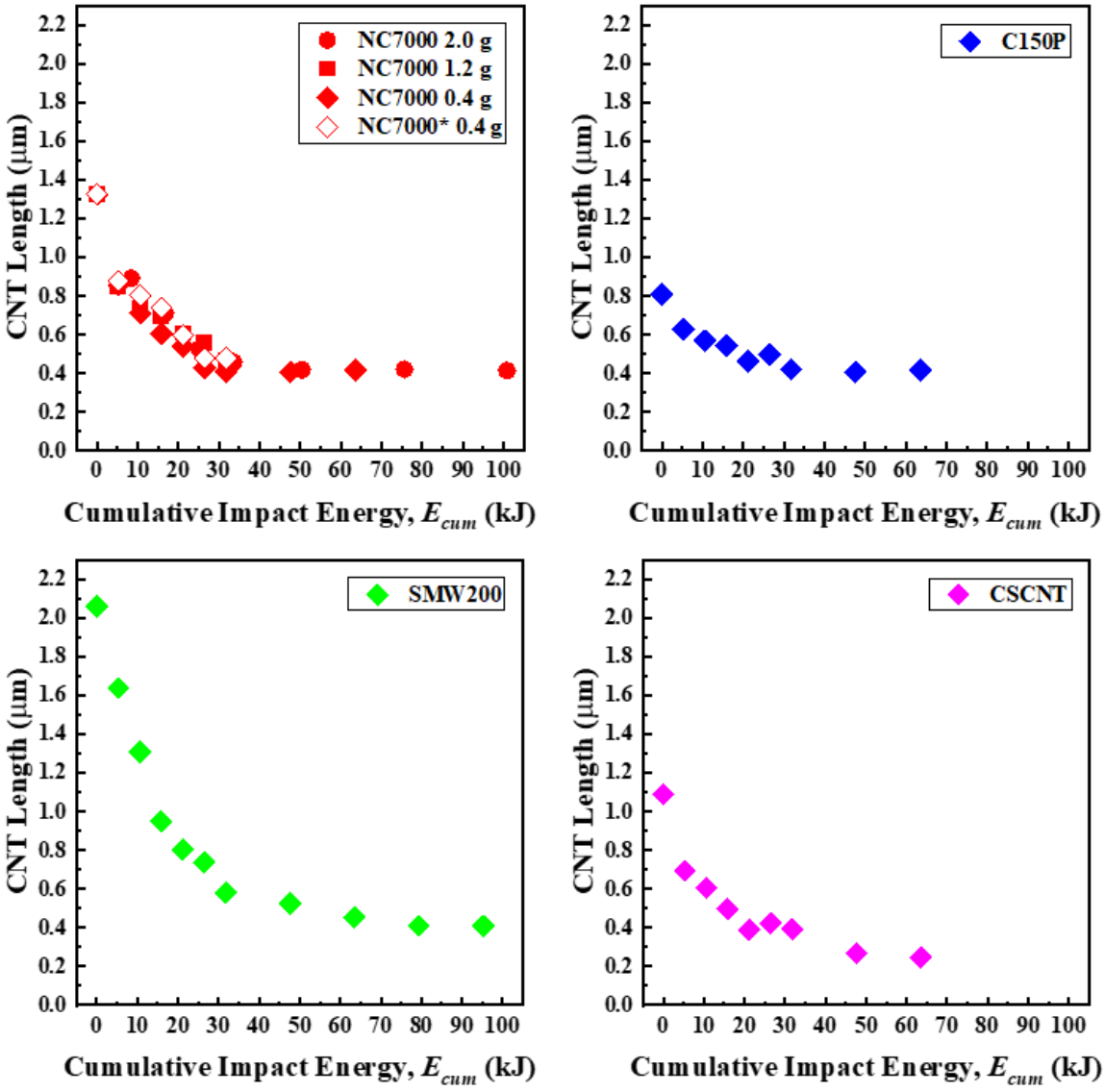

Figure 13: *Carbon nanotube length reduction with respect to cumulative impact energy.*

Each carbon nanotube sample undergoes exponential length reduction to a terminal length unique to each nanotube sample. For NC7000, C150P, and SMW200, the experimental terminal

length is nearly 400 nm, while CSCNT converge to approximately 200 nm. The shorter terminal length of the CSCNT indicates that cup-stacked wall morphologies may make nanotubes more susceptible to further length reduction to smaller aspect ratios. The terminal length for each nanotube is achieved by a cumulative impact energy of 350 kJ. The asymptotic behavior of carbon nanotube length reduction at high cumulative energies is consistent with what has been found in the literature for ball milling [118], although other high energy ball milling studies have shown carbon nanotubes can be further reduced to nanoparticles and amorphous carbon [120, 121].

An exponential equation relating carbon nanotube length to cumulative energy of milling was derived as shown

$$L = \left(L_o - L_f\right)e^{\frac{-E_{cum}}{E_{scale}}} + L_f \tag{19}$$

where L_o is the measured initial length of the raw commercial carbon nanotubes, L_f is the terminal length, and E_{scale} is a fitted parameter (termed "scaling energy") found by nonlinear regression (L_f also fitted in the regression). The limits were set so that at zero cumulative impact energy, the function is equivalent to the initial average length, and at sufficiently high cumulative energies, the function converges to the terminal length. Rearrangement of the Equation 11 yields a dimensionless length term which we will call the normalized length difference.

$$\frac{L - L_f}{L_o - L_f} = e^{\frac{-E_{cum}}{E_{scale}}} \tag{20}$$

At zero cumulative energy, the normalized length difference is 1, and at sufficiently high cumulative energy, the normalized length difference converges to 0.

Length reduction data given in Figure 13 for increasing cumulative energy was converted to the normalized length difference, and the four curves representing each commercial nanotube collapsed to a single master curve shown in Figure 14. The globally fitted scaling energy

parameter, E_{scale}, was found to be 13.9 ± 0.5 kJ. Visual observation of Figure 14 shows good agreement among the four commercial nanotube length reduction behaviors, and the exponential fit based on the cumulative energy of milling appears to describe the data well. While there is some clear discrepancy in the terminal behavior, the individually fitted terminal lengths fall well within the experimental error of the measured terminal lengths. In fact, fitting the individual data sets from Figure 13 for each nanotube resulted in scaling energy values all within three standard deviations of the globally fitted scaling energy.

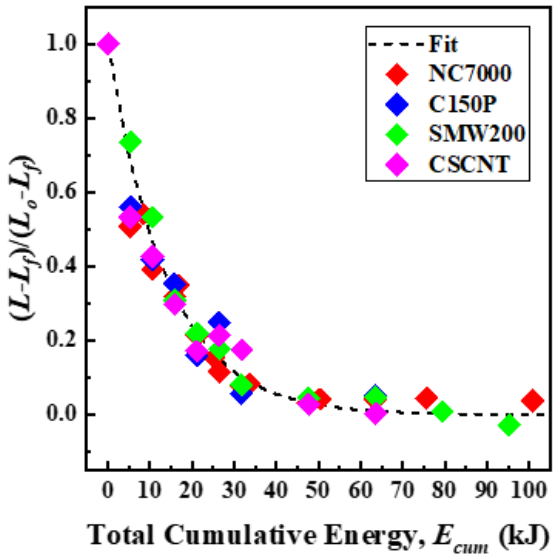

Figure 14: *Normalized length difference collapsed to a single curve with respect to total cumulative impact energy fitted by Equation 20.*

Instead of CNT length reduction being a function of the total single impact energy used during milling, another possibility is that the minimum single impact energy should be subtracted from the total single impact energy for a single collision. Hence, we then define the excess single

impact energy, $E_{b,ex}$, to be the difference between the total single impact energy, E_b, and the minimum single impact energy, $E_{b,min}$, as follows.

$$E_{b,ex} = E_b - E_{b,min} \tag{21}$$

The excess cumulative impact energy, $E_{cum,ex}$, can then be calculated by substituting $E_{b,ex}$ for E_b in Equation 15.

$$E_{cum,ex} = E_{b,ex} v_t t \tag{22}$$

An additional form of Equation 20 relating the normalized length difference to an exponential term was derived

$$\frac{L - L_f}{L_o - L_f} = e^{\frac{-E_{cum,ex}}{E_{scale,ex}}} \tag{23}$$

for CNT length reduction scaling with the excess cumulative impact energy with associated excess scaling energy, $E_{scale,ex}$. Figure 15 presents the normalized length difference with respect to excess cumulative impact energy, and $E_{scale,ex}$ was found to be 9.7 ± 0.3 kJ. The goodness of fit to the excess cumulative energy is statistically similar to that of Figure 14. If the single impact energy is sufficiently large, then subtracting $E_{b,min}$ from E_b appears to make no difference; Table 5 shows that E_b was significant compared to $E_{b,min}$ except for CSCNT. For CSCNT, the minimum impact energy is considered to be zero (under 3.5 mJ/impact detectable by our testing conditions). Consequently, the excess single impact energy is noticeably greater for CSCNT than for the other three nanotube samples. Visual observation of Figure 15 shows that CSCNT has slightly less agreement with the exponential model than the other three nanotube samples, especially at higher cumulative energies. To determine which model is more appropriate, impact energies closer to the minimum impact energy could be tested.

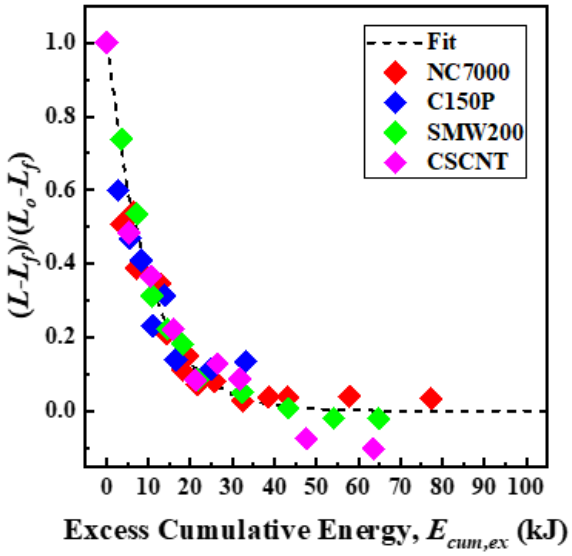

Figure 15: *Normalized length difference collapsed to a single curve with respect to excess cumulative impact energy fitted by Equation 23.*

Table 5: *Single impact energies associated with Figures 14 and 15.*

CNT	E_b	$E_{b,min}$	$E_{b,ex}$
NC7000	31 mJ	10 mJ	21 mJ
C150P	31 mJ	15 mJ	16 mJ
SMW200	31 mJ	10 mJ	21 mJ
CSCNT	31 mJ	< 3.5 mJ	31 mJ

3.2 Ultrahigh aspect ratio carbon nanotubes

3.2.1 Minimum single impact energy

The minimum single impact energy required to fracture a carbon nanotube was previously shown to dependent on CNT wall morphology and diameter. Because the VNT100 nanotubes are parallel walled and have an average diameter of 15 nm, the expected energy threshold for length

reduction is approximately 16 mJ/impact (see linear fit in Figure 9). To determine $E_{b,min}$ for VNT100, the ultrahigh aspect ratio nanotubes were milled at varying single impact energies, and SEM micrographs of milled CNTs are given in Figure 16. Milling at 3.5 mJ/impact, the lowest achievable single impact energy with 10 mm grinding balls at 100 rpm, shows the initial length was retained as expected (Figure 16a). However, even up to 125 mJ/impact, the highest achievable impact energy with 10 mm grinding balls at 600 rpm, significant length reduction cannot be detected by SEM micrographs (Figure 16b). Rather, the only major morphological change was the flattening of the large bundles to ribbon-like structures. Only when the grinding ball size was increased to 20 mm, subsequently increasing the impact energy to 175 mJ/impact at 300 rpm, is length reduction evident (Figure 16c), suggesting the minimum single impact energy for fracture is between 125 and 175 mJ/impact. Thus, we approximate $E_{b,min}$ of VNT100 to be 125 mJ/impact for subsequent analysis.

The order of magnitude larger energy threshold for fracture of these ultrahigh aspect ratio VNT100s suggests that powder morphology and/or agglomeration contribute to the milling characteristics of carbon nanotubes. The commercial carbon nanotubes studied previously were supplied in the form of roughly spherical agglomerates with small-bundled nanotubes randomly aligned and loosely packed within the agglomerates, while the ultrahigh aspect ratio VNT100 nanotubes synthesized in this study are almost exclusively aligned in loosely bundled arrays. According to impact induced CNT fracture simulations, fracture most readily occurs at the junctions of separate overlapping nanotubes [122]. Compared to randomly oriented commercial nanotubes, these ultrahigh aspect ratio CNTs have a much lower proportion of nanotube intersections, which could explain why length reduction occurs less readily. Or rather, their aligned nature distributes the force transferred from nanotube to nanotube along a greater distance,

reducing local force and breakage rates. Additionally, instead of correlating $E_{b,min}$ to the average individual nanotube diameter, perhaps it is more appropriate to correlate $E_{b,min}$ to the average bundle size. Based on SEM micrographs, the average bundle diameter for the VNT100 is approximately 10 µm, whereas most commercial CNTs, like NC7000, contain bundles up to 1 µm in diameter. This factor of ten increase in bulk diameter is comparable to the order of magnitude increase in energy threshold. So, for an industrially applied ball milling process for carbon nanotube length reduction, the bulk powder morphology must be considered in determining the minimum single impact energy necessary for nanotube fracture.

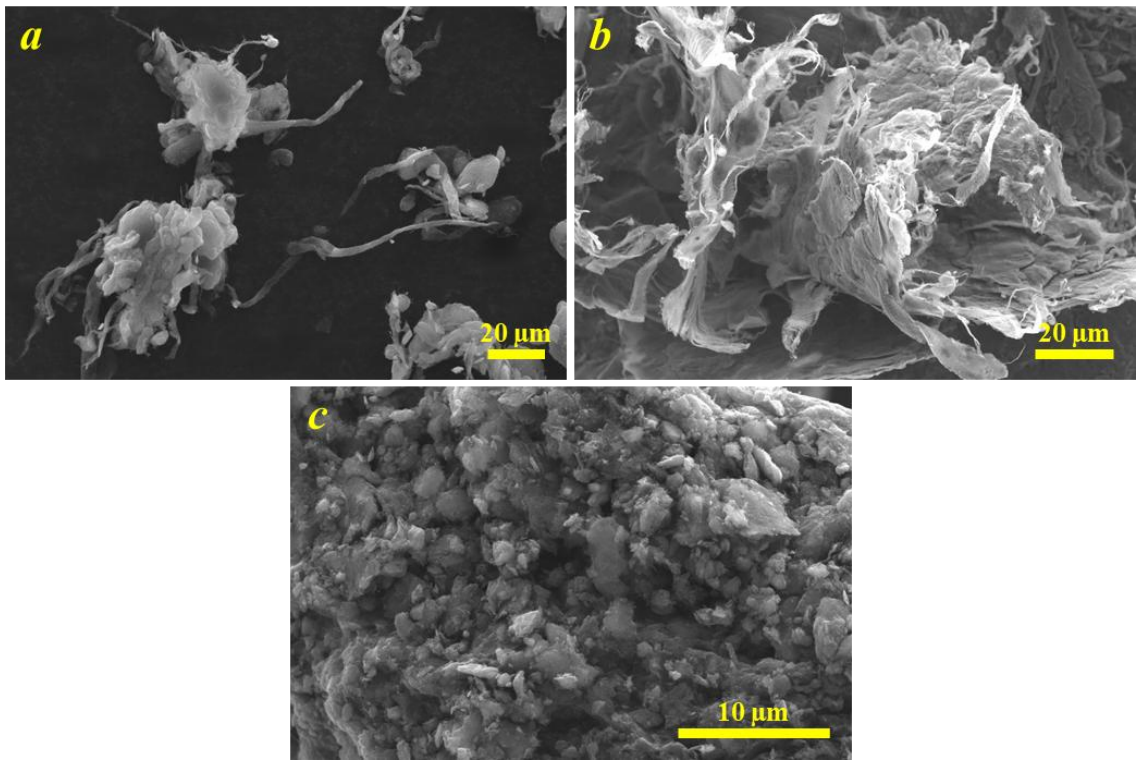

Figure 16: *SEM micrographs of VNT100 milled for 30 min at (a) 3.5 mJ/impact, (b) 125 mJ/impact, and (e) 175 mJ/impact.*

3.2.2 Length reduction kinetics

To evaluate the length reduction kinetics of ultrahigh aspect ratio CNTs, VNT100 nanotubes were milling at a fixed E_b of 175 mJ/impact for varying milling times ($E_{b,ex}$ of 50 mJ/impact according to Equation 21 assuming an $E_{b,min}$ of 125 mJ/impact). Figure 17 shows SEM micrographs of CNTs milled for varying durations, and Figure 18 displays measured VNT100 lengths compared to the kinetics predicted by Equations 20 and 23 considering the total and excess

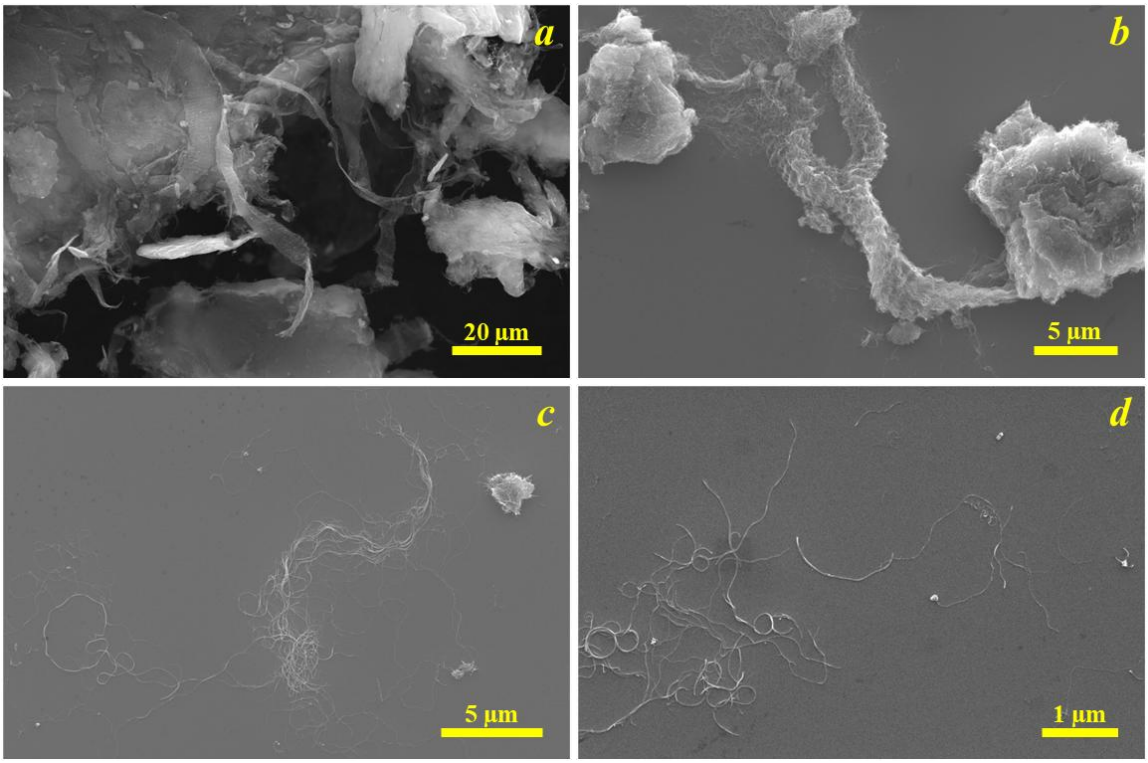

Figure 17: *SEM micrographs of CNTs milled at 175 mJ/impact for (a) 8 min, (b) 20 min, (c) 36 min, and (d) 60 min corresponding to the data points in Figure 18.*

cumulative impact energy, respectively. Clearly, the length reduction kinetics predicted by the total cumulative impact energy much better describe the measured lengths of the milled ultrahigh aspect ratio CNTs as compared to the excess cumulative impact energy. While the red curve

appears to slightly overestimate CNT length for the initial stages of milling, the measurements are well within the margin of error encompassing the predicted length reduction kinetics.

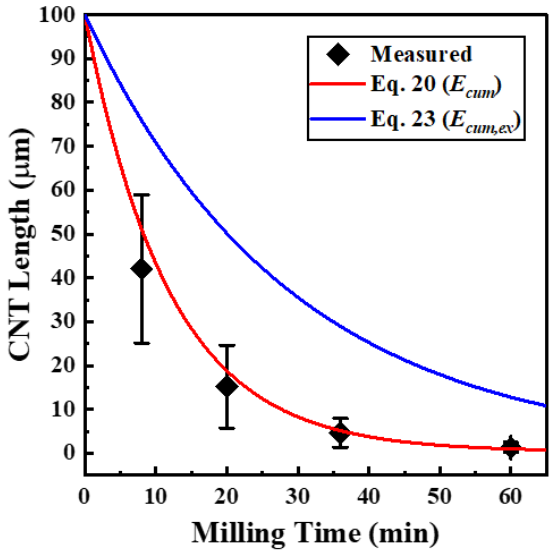

Figure 18: *Milling-induced length reduction of ultrahigh aspect ratio CNTs compared to length reduction kinetics predicted by Equations 20 or 23.*

While $E_{b,min}$ is an important consideration in the practical application of ball milling for CNT length reduction, Figure 18 suggests that the extent to which E_b exceeds $E_{b,min}$ is irrelevant as long as $E_b > E_{b,min}$. However, there are two considerations that could modify this assertion. First, because there is often a distribution of nanotube diameters, bundle sizes, and defect characteristics in a bulk CNT sample, there exists a theoretical distribution for $E_{b,min}$ on an individual CNT basis. For example, if an E_b is chosen that exceeds $E_{b,min}$ for some CNTs but is below $E_{b,min}$ for other CNTs, the length reduction kinetics would certainly change. Second, there logically exists a maximum single impact energy for which continuing to increase E_b results in no further CNT fractures within the impact area. Despite these possible deviations from the predicted behavior,

typical milling conditions used in laboratory and industrial settings are likely to fall within an acceptable range that adheres to the length reduction kinetics predicted by Equation 20 with the total cumulative impact energy. These results are promising for controlling length reduction of CNTs with widely varying initial lengths, diameters, wall morphologies, and bulk powder morphologies.

3.2.3 Defect density and electrical conductivity

The effects of ball milling on the electrical conductivity and defect density of VNT100 are shown in Figure 19. A notable observation is the increase in electrical conductivity and decrease in defect density upon short durations of milling. Initial rationale would suggest that any amount of impact induced change in CNT morphology would result in an increase in defect density due to the breakage of covalent carbon-carbon bonds, which would lead to a reduction in the electrical conductivity of the CNTs. While previously discussed results with short, commercial CNTs showed no notable variance in defect density upon milling, the decreases in defect density upon milling show here are initially unexpected. This phenomenon could be explained by a combination of different effects. First, the vermiculite sheets between CNT bundles effectively form an electron barrier, limiting the electrical conductivity of the CNTs in the bulk powder morphology. Upon short times of ball milling, vermiculite sheets break apart and could allow individualized nanotubes or nanotube bundles to form a conducting network or act as conductive bridges between larger vermiculite-capped bundles. Second, as carbon nanotube ends are dislodged from the catalyst sites upon vermiculite breakage, carbon radicals may undergo healing to a lower energy state (i.e., reforming closed or partially closed CNT ends) [123, 124]. Finally, and most probably, milling could strip CNT surfaces of amorphous carbon. Upon closer inspection of high-resolution TEM

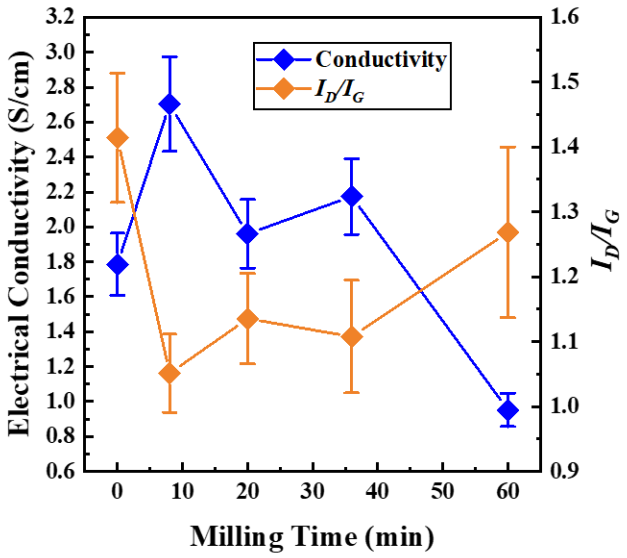

Figure 19: *Effects of planetary ball milling on CNT electrical conductivity and defect density.*

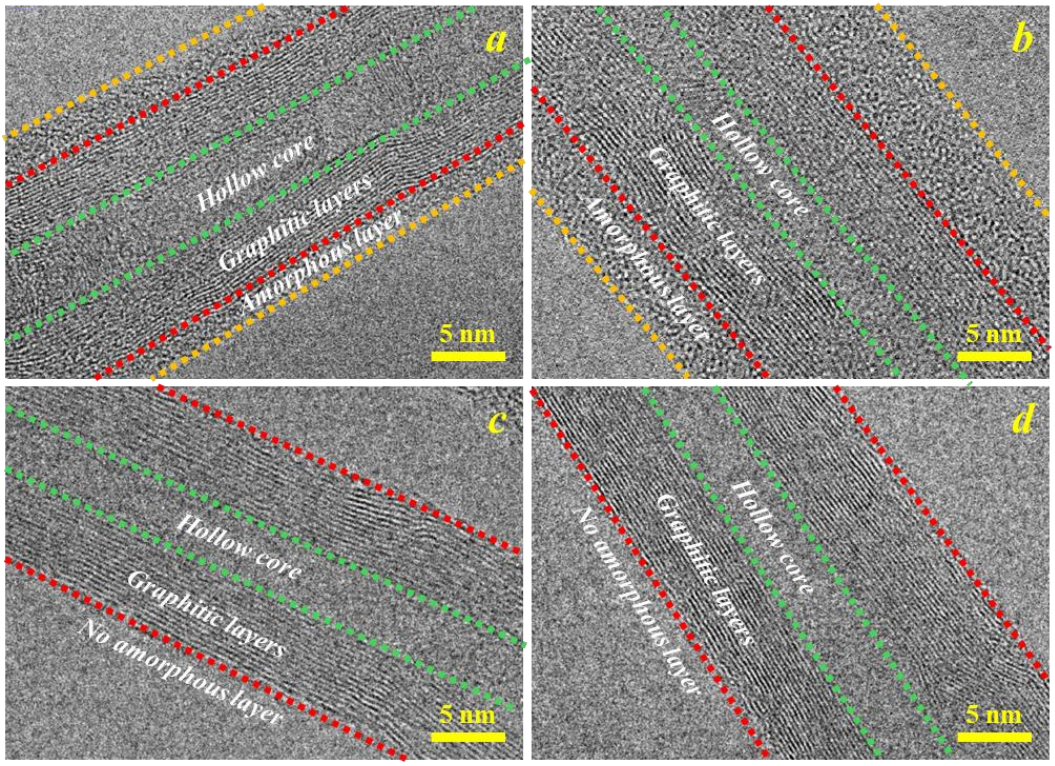

Figure 20: *Milling-induced stripping of surface impurities as evidenced by high resolutions TEM micrographs of (a-b) pristine C150P and (c-d) milled C150P.*

micrographs, a layer of amorphous carbon can be found on the outer surfaces of pristine, as-synthesized CNTs. The thickness of this amorphous carbon layer varied widely (between 0.5-5 nm) but was most pronounced for C150Ps. Figure 20 shows C150P nanotubes before and after milling, clearly demonstrating the elimination of the amorphous layer upon ball milling. However, as milling duration increased, the defect density slightly increased along with a decrease in electrical conductivity.

3.3. Comparison to length reduction by ultrasonication

3.3.1 Fracture mechanism

To our knowledge, sonication has been the only mode of carbon nanotube fracture other than ball milling in which the kinetics of length reduction have been studied. Initial studies on nanotube cleavage by sonication assumed a purely tensile mechanism by which the nanotubes orient radially as bubbles nucleate, grow, and collapse [75]. The critical force, F_c, for nanotube breakage derived by Hennrich et al. [73] and restated by Pagani et al. [76] based on the tensile strength, σ_{break}, of the nanotube is given by the following

$$F_c = \sigma_{break}\pi\frac{(2Dw - w^2)}{4} \tag{24}$$

where D is the CNT diameter and w is the thickness of the wall. The discussions surrounding this equation involved only SWCNTs, and the critical force was estimated to be 20 nN. Later studies utilizing Brownian dynamics simulations found that long nanotubes can experience axial compression [77] or align tangentially to bubbles and experience radial buckling [76]. As the nanotubes shorten to approximately 1 μm, the fracture mechanism can shift from buckling to tensile, which is shown in Figure 21.

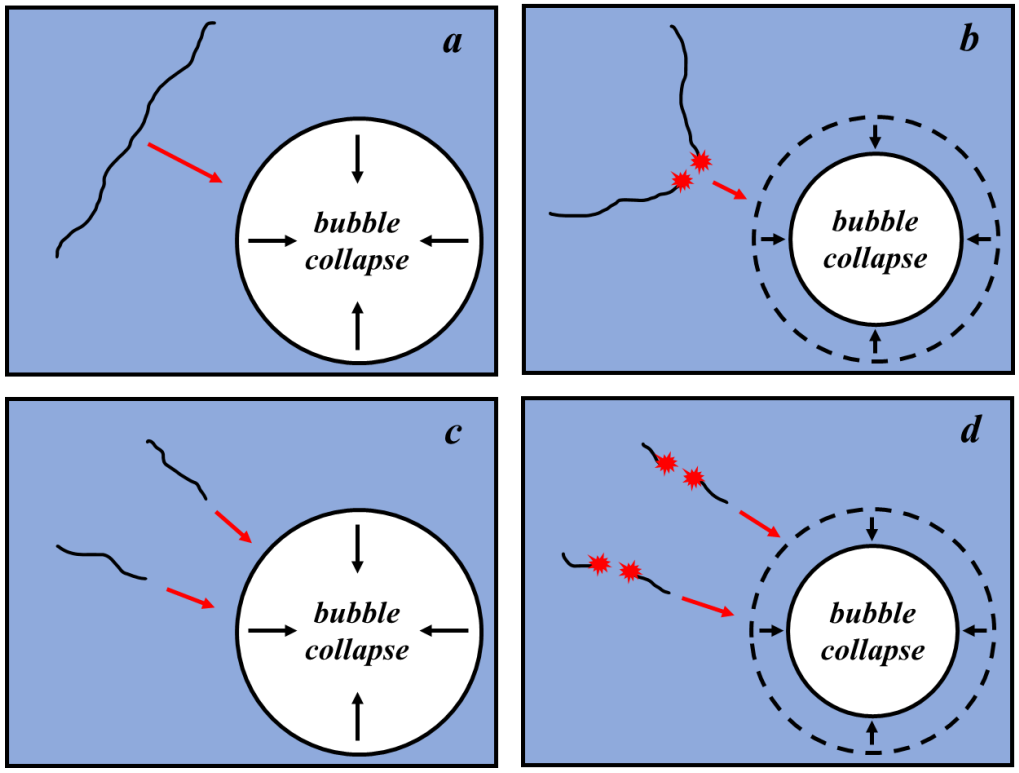

Figure 21: *Sonication of carbon nanotubes imparts (a-b) radial buckling on long carbon nanotubes and (c-d) axial tension for short nanotubes. Red arrows indicate the force experienced by the nanotubes, and red dots indicate points of fracture.*

Ball milling carbon nanotubes likely employs a buckling fracture mechanism. Because the carbon nanotube powder morphology consists of aggregates with randomly oriented and curved nanotubes, molecular dynamics simulations indicate that impact-induced fracture tends to occur at the intersections of adjacent nanotubes [122]. Attempts to relate the minimum single impact energy for CNT fracture to some physical characteristic of the nanotubes, as proposed in Equation 24 for sonication, were unsuccessful due to uncertainty in the characteristic length by which to translate energy into force and vice versa. As illustrated in Figure 22, for very long nanotubes, there are initially many nanotube intersections at which impact induced fracture can occur. As nanotubes shorten, the frequency of nanotube intersections decreases substantially, consistent with

exponential length reduction behavior with increasing cumulative impact energy. While the discovered scaling energy, E_{scale}, effectively represents the rate at which carbon nanotubes fracture from ball milling, attempts to translate the meaning of this term to some physical attribute of CNTs or the ball milling system proved unsuccessful.

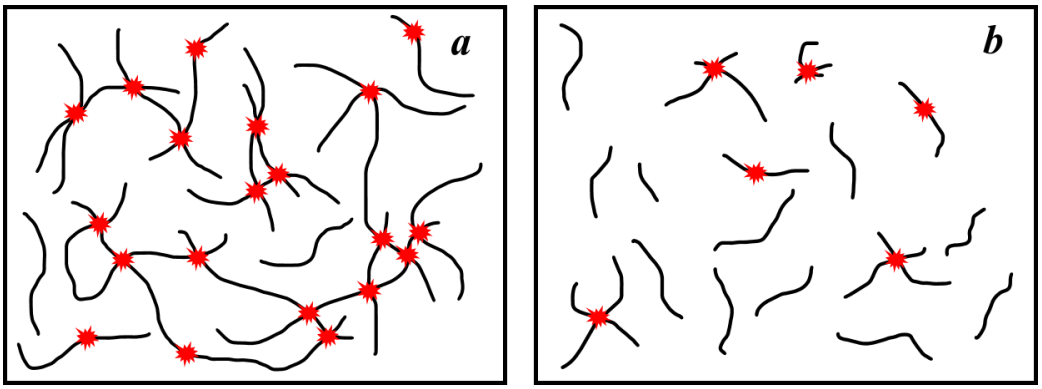

Figure 22: *Representative schematic of impact induced fracture of (a) long and (b) short carbon nanotubes. Red dots indicate points of fracture. Most CNTs fracture points occur at CNT-CNT intersections, but isolated CNTs may fracture as well.*

Figure 23 shows characteristic capped and open nanotube tip morphologies as observed by HRTEM. Pristine NC7000 appeared to have a relatively even distribution of capped and open ends as in Figure 13a and 13c, while pristine CSCNT had a much higher concentration of open ends. The wide cone end of the cup stacked nanotubes was observed to always be open as in Figure 23d, while the narrow cone end occasionally had a capped tip as in Figure 23b. Milled nanotubes that had been reduced to their terminal length contained a much higher concentration of open ends compared to the unmilled nanotubes. Regardless of wall morphology, the most common end morphology of milled nanotubes involved a notable collapsed restriction in CNT diameter at the

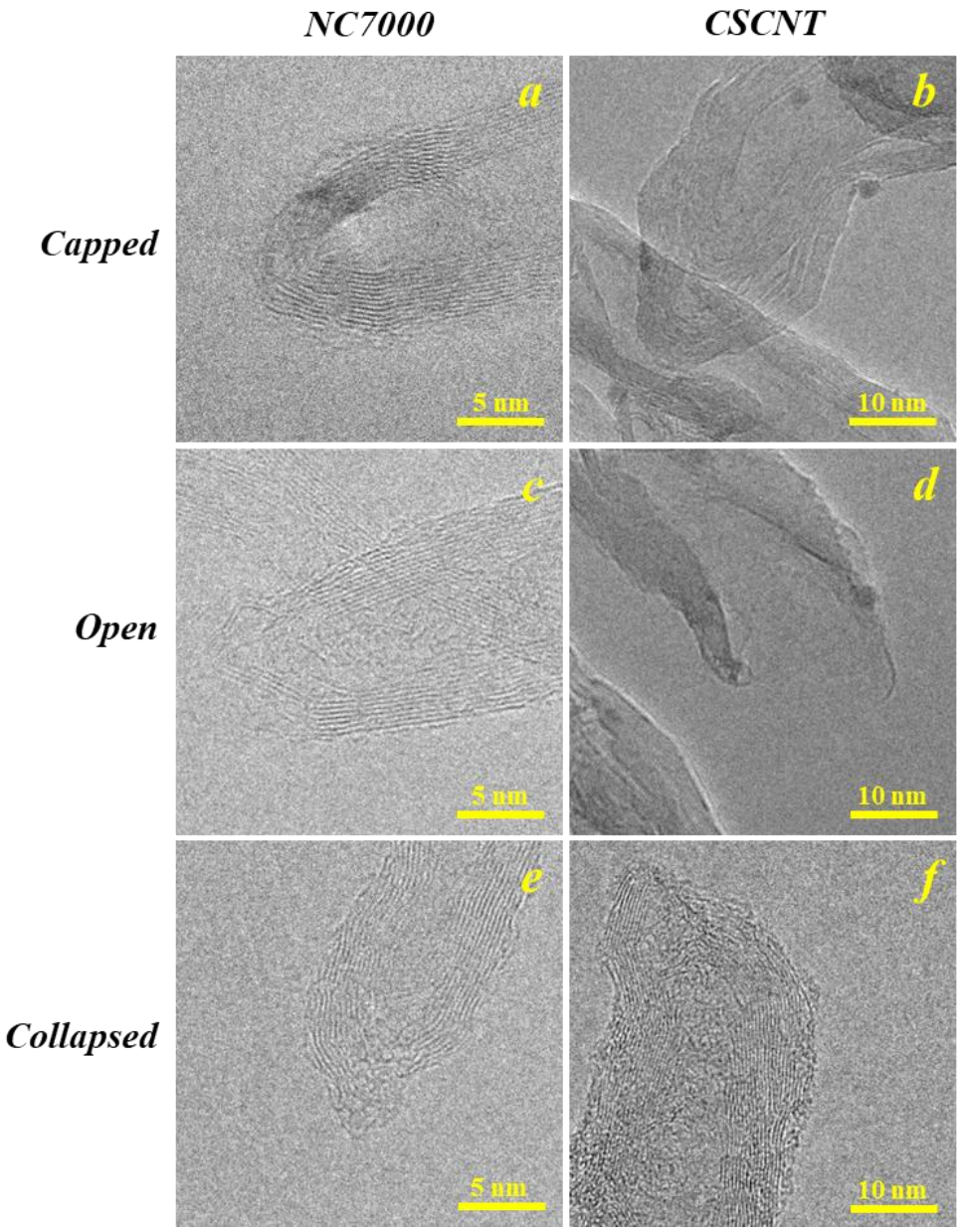

Figure 23: *Representative TEM micrographs of (a-b) capped, (c-d) open, and (e-f) collapsed CNT ends of parallel walled (NC7000) and cup-stacked (CSCNT) CNTs.*

tip as in Figures 23e-f. This smaller diameter could be evidence of the proposed mechanism by which fracture occurs by buckling at nanotube intersections. It should be noted that observation of this end morphology in TEM is sensitive to the nanotube orientation relative to the electron beam.

Also, caps on nanotube ends can reform after fracture due to being more configurationally favorable, so visual observation by TEM alone cannot validate the fracture mechanism. Capped nanotube ends present in milled samples could either be initially capped and undisturbed by milling or could be reformed after milling.

Many analogs exist between sonication of long nanotubes and ball milling. The increasing energy required for length reduction with increasing diameter appears to be consistent between the two processes. Also, both sonication and ball milling result in a terminal length, as experimental data from Lucas et al. [75] showed length reduction convergence to an apparent terminal length at high cumulative ultrasonic energies. A potential difference between the two processes is the possibility of diameter reduction or complete wall stripping. While ball milling can induce defects on nanotube surfaces and ends, we and most others have found that carbon nanotube diameters remain constant during milling [81]. However, wall stripping and slight diameter reduction has been reported for ultrasonication [125].

3.3.2 Power law length reduction kinetics

Previous sonication studies used a power law to describe the kinetics of carbon nanotube length reduction. To compare our data with previous studies, a power law was fit to the length reduction data given in Figures 13 and 18. As was done previously, experimental data points at high cumulative impact energies that show a very small change in length reduction compared to points at lower energies were eliminated. The power law fit for the four commercial nanotube samples and ultrahigh aspect ratio VNT100 is shown in Figure 24.

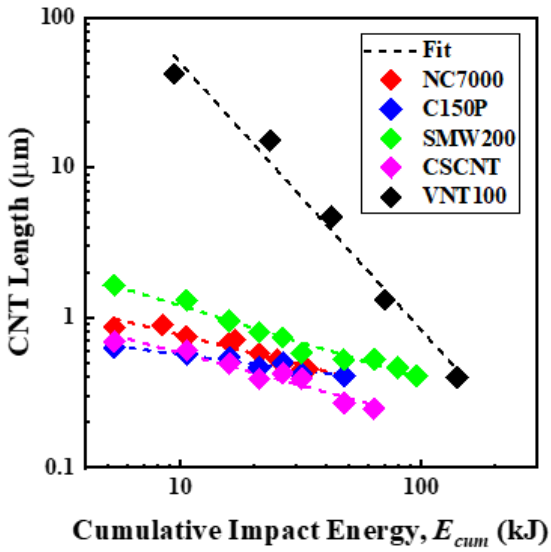

Figure 24: *Length reduction behavior of carbon nanotubes with respect to cumulative impact energy fit to a power law.*

The power law exponents that describe the length reduction kinetics of the nanotubes studied in this work are presented in Table 6 with comparisons to previous studies on sonication and ball milling. While the power law relationship in sonication studies was explicitly given, it was necessary to extract ball milling data from graphs in milling studies (minimum of four data points) and fit the data to a power law to obtain the power law exponent. To our knowledge, Table 6 encompasses all the kinetic length reduction data for sonication and milling in the current literature provided with sufficient detail with respect to sonication/milling time. The SMW200 power law exponent compares to the findings of Hennrich et al. [73] for sonication and Pierard et al. [126] for ball milling, while the C150P power law exponent is akin to the findings of Lucas et al. [75], Jang et al. [78], and other ball milling studies [81, 90, 127].

Table 6: *Power law relationships between sonication/milling E_{cum} and CNT length.*

Source	Power Law Relationship*
This Work (MWCNTs)	$L \propto E_{cum}^{-1.78}$ (VNT100) $L \propto E_{cum}^{-0.40}$ (NC7000) $L \propto E_{cum}^{-0.20}$ (C150P) $L \propto E_{cum}^{-0.49}$ (SMW200) $L \propto E_{cum}^{-0.43}$ (CSCNT)
Hennrich et al. (SWCNTs)	$L \propto E_{US}^{-0.5}$
Lucas et al. (SWCNTs)	$L \propto E_{US}^{-0.21}$ (#6077) $L \propto E_{US}^{-0.23}$ (#6078)
Jang et al. (MWCNTs)	$L \propto E_{US}^{-0.25}$
Pierard et al. (MWCNTs)	$L \propto E_{cum}^{-0.51}$
Kozma et al. (MWCNTs)	$L \propto E_{cum}^{-0.18}$
†Papp et al. (MWCNTs)	$L \propto E_{cum}^{-0.20}$
†Kukovecz et al. (MWCNTs)	$L \propto E_{cum}^{-0.20}$

*Ball milling studies are indicated by E_{cum} and sonication studies are indicated by E_{US}.

†A poor power law fit ($R^2 < 0.9$) was found for the data in these studies.

Comparison among the CNTs used in this study indicates the power law kinetics for length reduction by ball milling is dependent on the initial carbon nanotube length. The ultrahigh aspect ratio VNT100 nanotubes exhibited the fastest rate of length reduction (e.g. highest power law exponent), and conversely, the shortest nanotube sample, C150P, exhibited the slowest rate of length reduction. This result is consistent with the trend found in previous ball milling studies, as

Pierard et al. [126]. used initially very long nanotubes, while the other ball milling studies used shorter nanotubes [81, 90, 127]. Sonication studies also exhibited a dependence on initial carbon nanotube length; however, the relationship is the inverse of that found for ball milling. Simulation results of Pagani et al. suggested long and short nanotubes are described by power law exponents of roughly -0.22 and -0.5, respectively [76]. The difference between the two processes could be explained by the difference in mechanism for different length nanotubes in sonication, whereas ball milling is assumed to have a consistent fracture mechanism independent of nanotube length.

Chapter 4: Carbon nanotube surface chemistry modification by planetary ball milling

4.1 Dry mechanochemical functionalization with ammonium carbonate

Ball milling induces local hot spots at points of impact between grinding media and the grinding vessel wall. As milling time increases, so does the bulk temperature in the milling vessel. Because ammonium carbonate has a decomposition temperature well below 100 °C, it is assumed that ammonium carbonate readily decomposes into gaseous ammonia (NH_3), carbon dioxide (CO_2) and water (H_2O) during milling. Thus, because carbon nanotubes experience fracture and surface amorphizations during milling, carbon radicals formed from broken C=C bonds could readily react with ambient species to form oxygen and nitrogen containing functional groups. A schematic of the proposed dry mechanochemical functionalization method is presented in Figure 25.

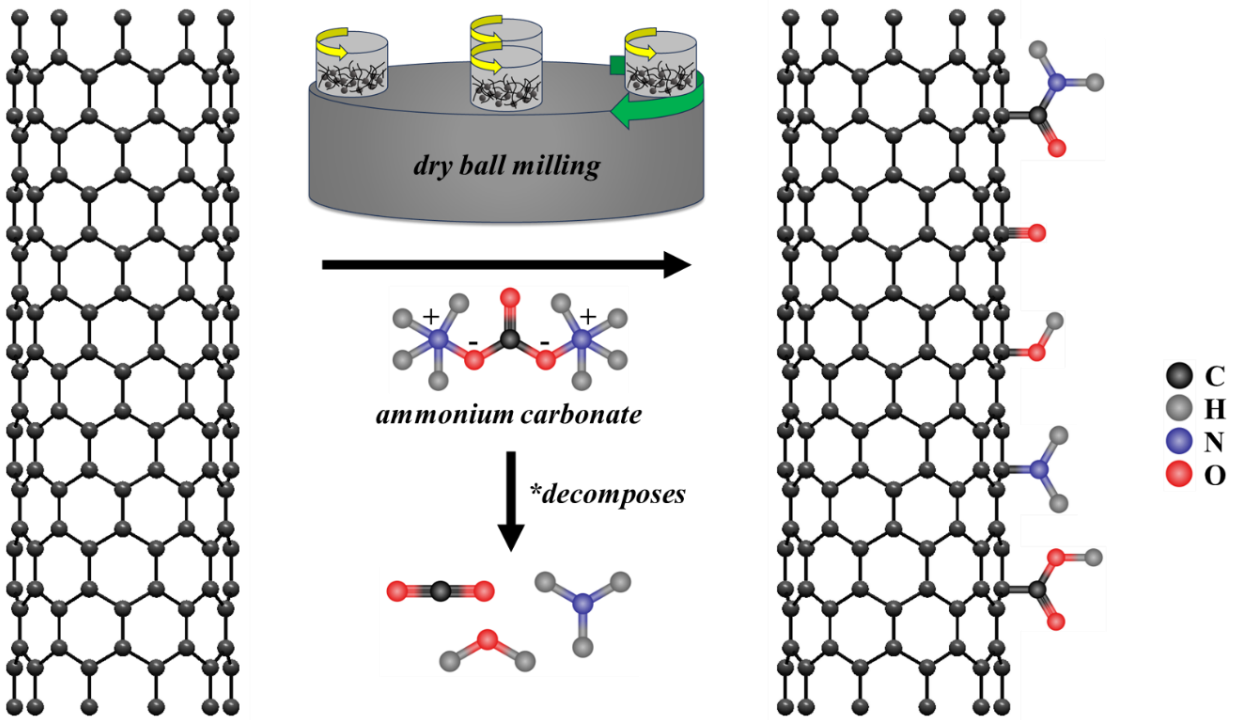

Figure 25: *Schematic of dry ball milling induced functionalization of CNTs with ammonium carbonate.*

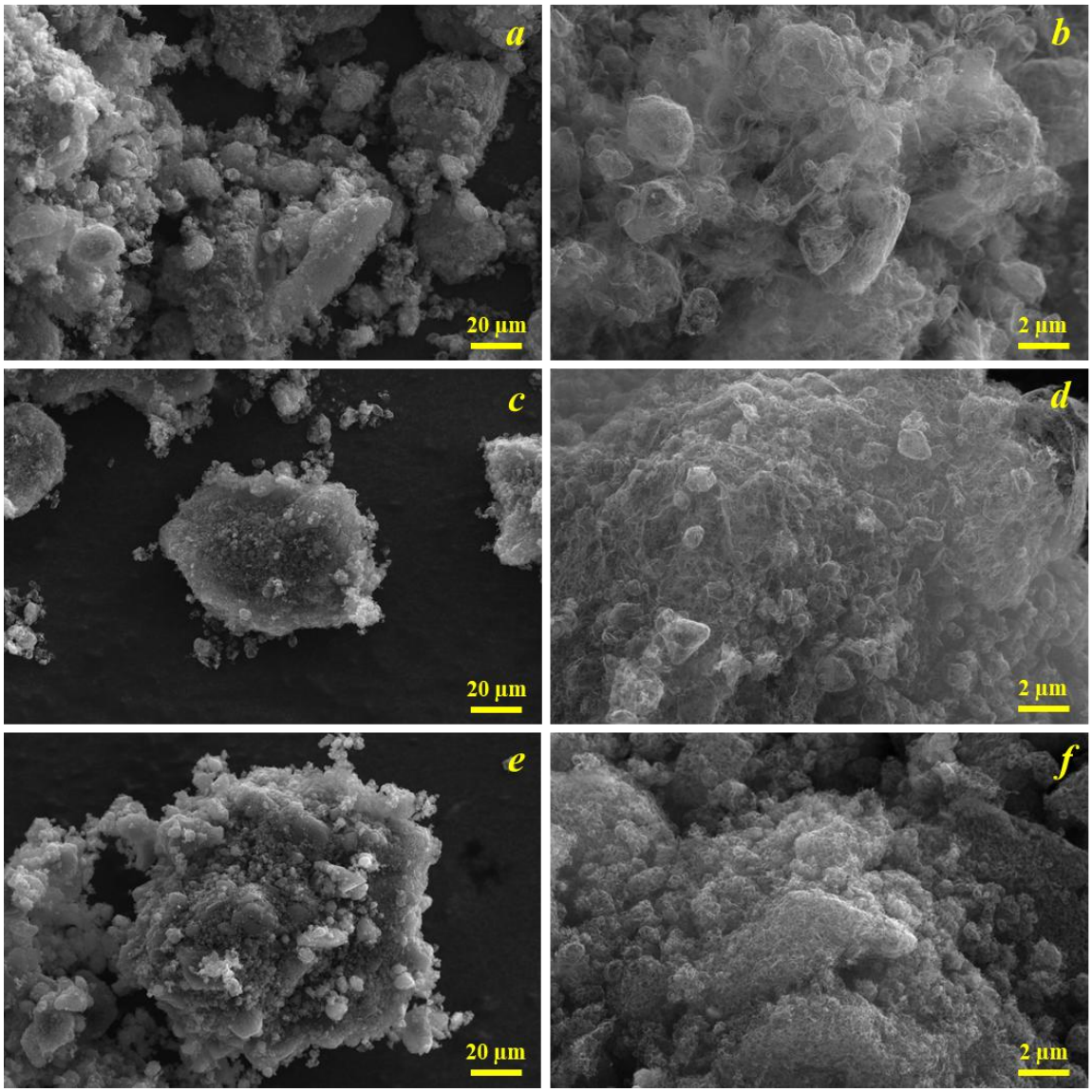

Figure 26: *SEM micrographs of dry mechanochemically functionalized VNT100 milled at 300 rpm for (a-b) 30 min, (c-d) 1 hr, and (e-f) 4 hr.*

The morphology of dry mechanochemically functionalized VNT100 (dfVNT) nanotubes can be seen in Figure 26. The agglomeration characteristics are quite different compared to the pristine VNT100 primarily due to the disappearance of large bundles. Rather, the dfVNTs appear to be randomly agglomerated in somewhat spherical agglomerates. Additionally, nanotube length

is significantly reduced compared to the originally long pristine VNT100. Milling for 30 min, 1 hr, and 4 hr at 300 rpm results in average CNT lengths of approximately 5 µm, 1 µm, and 400 nm, respectively. These values largely agree with the kinetic length reduction behavior found previously.

Figure 27 presents the thermal degradation curves for dfVNT samples milled at varying conditions. Because carbon nanotubes are generally thermally stable up to high temperatures well

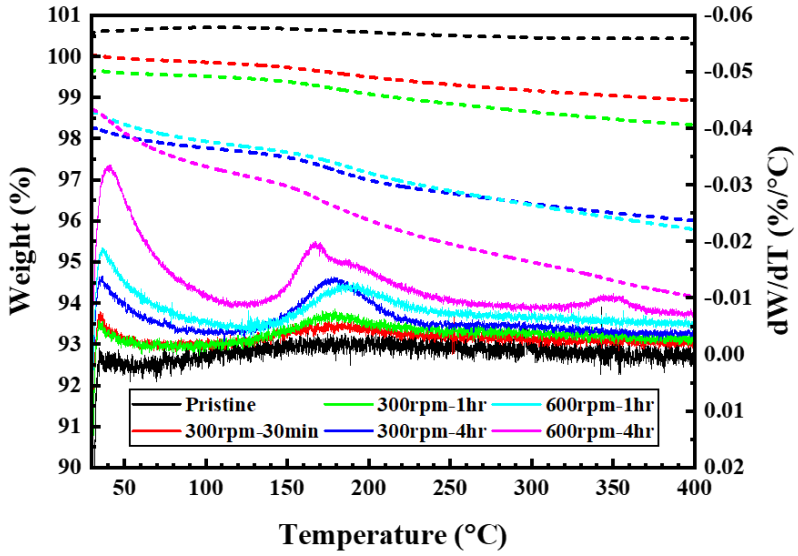

Figure 27: *Thermal degradation behavior of dry mechanochemically functionalized VNT100.*

above 400 °C, weight loss at low temperatures is typically indicative of desorption and/or degradation of adsorbed groups (like water) and covalently bonded functional groups. Pristine VNT100 shows negligible weight loss up to 400 °C whereas all dfVNT samples show different extents of thermal degradation behavior under 400 °C. For all dry mechanochemically functionalized CNTs, there is a consistent weight loss feature under 100 °C, and the size of this peak appears to scale with E_{cum}. This feature is likely indicative of the presence of physically

absorbed species on the surfaces of CNTs, most likely being the decomposed constituents of ammonium carbonate (NH_3, CO_2, and H_2O) as well as ambient moisture. All dfVNT samples show some thermal degradation around 180 °C as evidenced by a consistent peak location in in the derivative curves, possibly indicative of the introduction of a certain type of covalently bonded functional group to the surface of the CNTs. The size of this peak also appears to increase with increasing E_{cum}. For the highest cumulative milling energy applied (13,500 kJ corresponding to 600 rpm for 4 hr), additional weight loss features are present around 160 °C and 350 °C, possibly indicative of the presence of different functional groups.

The degree of functionalization can be calculated based on weight loss in given temperature regimes. Given that most small physiosorbed and chemisorbed oxygen and nitrogen containing groups desorb or decompose at temperatures below 400 °C [128, 129], degree of functionalization, θ_f, can be calculated by the following

$$\theta_f = \frac{m_{30°C} - m_{400°C}}{m_{30°C}} * 100\% \tag{25}$$

where and $m_{30°C}$ and $m_{400°C}$ are the masses of the sample at 30 °C and 400 °C, respectively. Figure 28 shows the relationship between cumulative energy of milling and degree of functionalization. The correlation behavior follows a power law of the following form

$$\theta_f = k_f E_{cum}^{n_f} \tag{26}$$

with rate coefficient, k_f, of 0.36 ± 0.03 and power law exponent, n_f, of 0.33 ± 0.01 (R^2 = 0.996). Because this dry mechanochemical functionalization phenomenon could result in both physisorption and chemisorption as well as yield multiple layers of adsorbed species, it may be appropriate to consider this power law behavior in the context of Freundlich-like adsorption [130]. While the Freundlich isotherm typically describes the power law dependence of surface coverage on partial pressure of adsorbate, the cumulative energy of milling in the case of this study may be

directly related to partial pressure of the decomposed ammonium carbonate species in the milling vessel. While it is initially assumed that ammonium carbonate fully decomposes during milling, there is certainly a period of partial decomposition in the early stages of milling, meaning the partial pressure changes in this milling period. Additionally, if full decomposition of ammonium carbonate does not occur after 30 min, increasing the milling time to 1 hr and 4 hr would effectively increase the partial pressure of the decomposed species in the vessel. It should be noted that because ball milling fractures carbon nanotubes, the total adsorption area increases during the process. Thus, accurate modeling of CNT adsorption behavior during ball milling would need to involve more detail than a simple empirical power law model like the Freundlich isotherm.

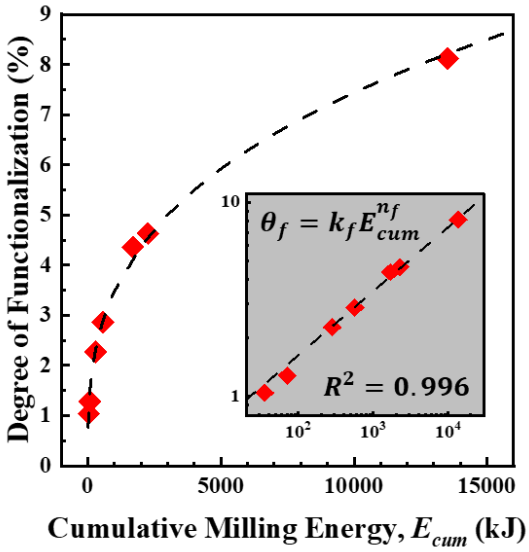

Figure 28: *Degree of functionalization of dry mechanochemically functionalized VNT100 correlated to cumulative impact energy.*

Full XPS spectra and C1s core level scans are presented in Figures 29 and 30, respectively, along with C1s peak deconvolution analysis in Table 7. Pristine VNT100 shows a relatively low

oxygen content as expected based on negligible weight loss from TGA, whereas dfVNT samples display increasing oxygen content with increasing milling time. However, no significant nitrogen content is detected up to 4 hr milling time at 300 rpm. This is somewhat surprising as previous studies using similar functional species (ammonium bicarbonate) asserted that mechanochemically functionalized CNTs were primarily doped with amine and amide functional groups [131]. Plausible explanation for this discrepancy could lie in the longer milling times used and different

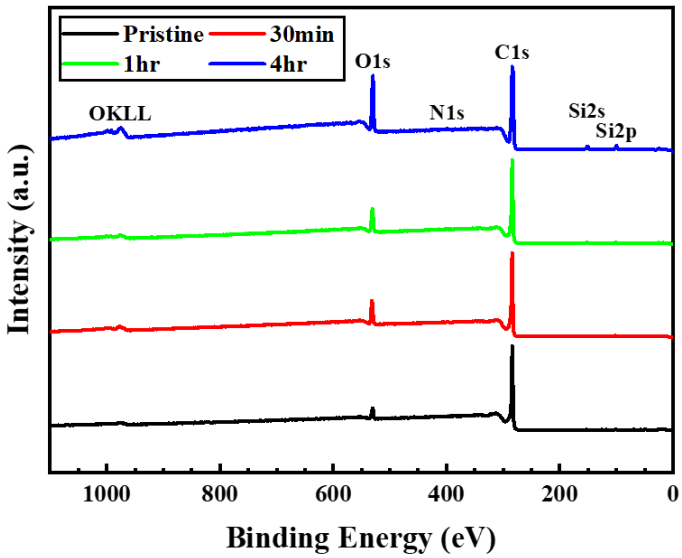

Figure 29: *XPS spectra of pristine and dry mechanochemically functionalized VNT100.*

grinding media configurations that could impart higher cumulative milling energies. However, XPS spectra presented in these previous studies do exhibit increased oxygen content compared to pristine CNTs, confirming the addition of oxygen-containing moieties. The most prevalent oxygen-containing carbon binding state, C-O, is confirmed by the peak located at 286.0-286.3 eV and is likely evidence of hydroxyl groups (R-OH) added to CNT surfaces, although ethers (R-O-R) could also be present. The peak located around 287.0-287.1 eV, attributed to the C=O binding

state, could be evidence of ketones (R=O) or aldehydes (R-COH). Additionally, the peak located at 288.0-288.5 eV attributed to the O-C=O binding state is likely evidence of carboxyl groups (R-COOH). The reduction in π-π* transition satellite peak located between 290.0-290.8 eV is indicative of the disruption of the conjugated π network due to the presence of functional groups.

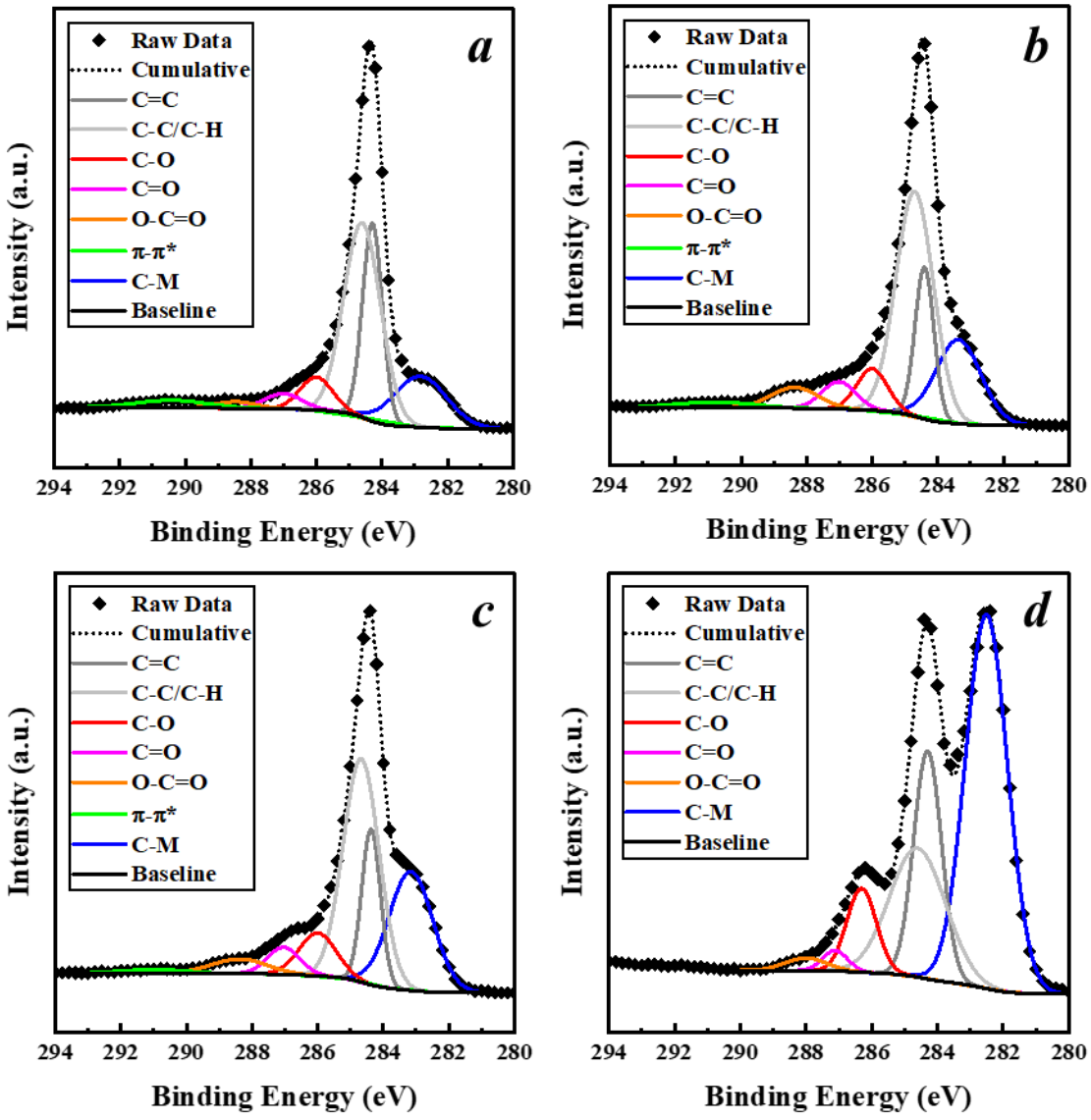

Figure 30: *C1s core level deconvolution for (a) pristine and dry mechanochemically functionalized VNT100 milled at 300 rpm for (b) 30 min, (c) 1 hr, and (d) 4 hr.*

While the evidence of functionalization and reduced bulk agglomeration is promising for application in polymer composites, a perhaps undesired byproduct of the process is seen from the increasing peak located at 282.8-283.4 eV representing carbide bonds (C-M; M represents metal or metalloid). Pristine VNT100 displays a notable peak in this region which can be attributed to C-Fe and C-Co bonds. Because the VNT100 nanotubes are not purified, nanotubes are still attached to the vermiculite supports at their catalyst sites which are composed of iron and cobalt. Upon mechanochemical functionalization, the carbide peak significantly increases, which could also be attributed to the formation of carbide bonds with silicon or aluminum native to the vermiculite supports. Mechanochemical synthesis of Si-C carbides via co-milling of nanocarbons

Table 7: *C1s peak deconvolution analysis corresponding to Figure 30.*

Species	VNT100		dfVNT (30 min)		dfVNT (1 hr)		dfVNT (4 hr)	
	eV	at%	eV	at%	eV	at%	eV	at%
C=C	284.3	24.10	284.4	15.32	284.4	14.82	284.3	19.37
C-C/C-H	284.6	44.36	284.7	45.24	284.7	40.86	284.6	21.91
C-O	286.0	6.62	286.0	6.82	286.0	8.15	286.3	7.52
C=O	287.0	3.48	287.0	4.96	287.0	4.49	287.1	1.56
O-C=O	288.5	1.61	288.4	5.17	288.4	4.11	288.0	1.57
π-π*	290.4	3.23	290.8	2.15	291.0	1.09	-	-
C-M	282.8	16.59	283.4	20.33	283.1	26.49	282.5	48.07

and silicon powders has been reported previously [132]. Thus, for dry milling, extent of functionalization should possibly be balanced with the undesired formation of carbide bonds in

the case of milling unpurified CNT powders containing catalyst and support materials. Considering also the significant length reduction experienced by the CNTs during milling, shorter dry mechanochemical functionalization times may be more beneficial in the context of polymer-CNT composites.

4.2 Aqueous mechanochemical functionalization with ammonium carbonate

Whereas dry milling CNTs induces surface functionalization through decomposition of ammonium carbonate due to local hot spots and bulk temperature rise, the introduction of water into the milling vessel causes the dissolution of ammonium carbonate into ammonium (NH_4^+) and carbonate (CO_3^-) ions. These ions in solution would allow for their reaction with carbon radicals

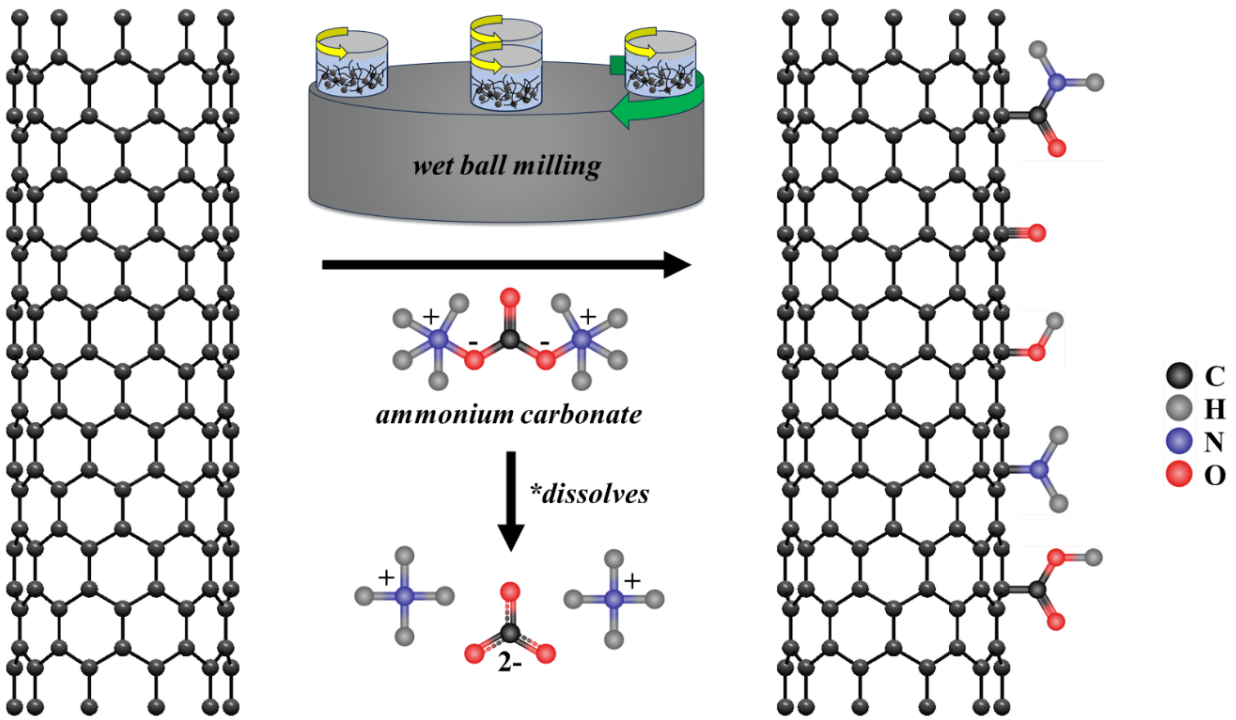

Figure 31: *Schematic of wet ball milling induced functionalization of CNTs with ammonium carbonate.*

formed from CNT fracture, introducing functional groups to CNT surfaces. A schematic of the proposed aqueous mechanochemical functionalization method with ammonium carbonate is presented in Figure 31.

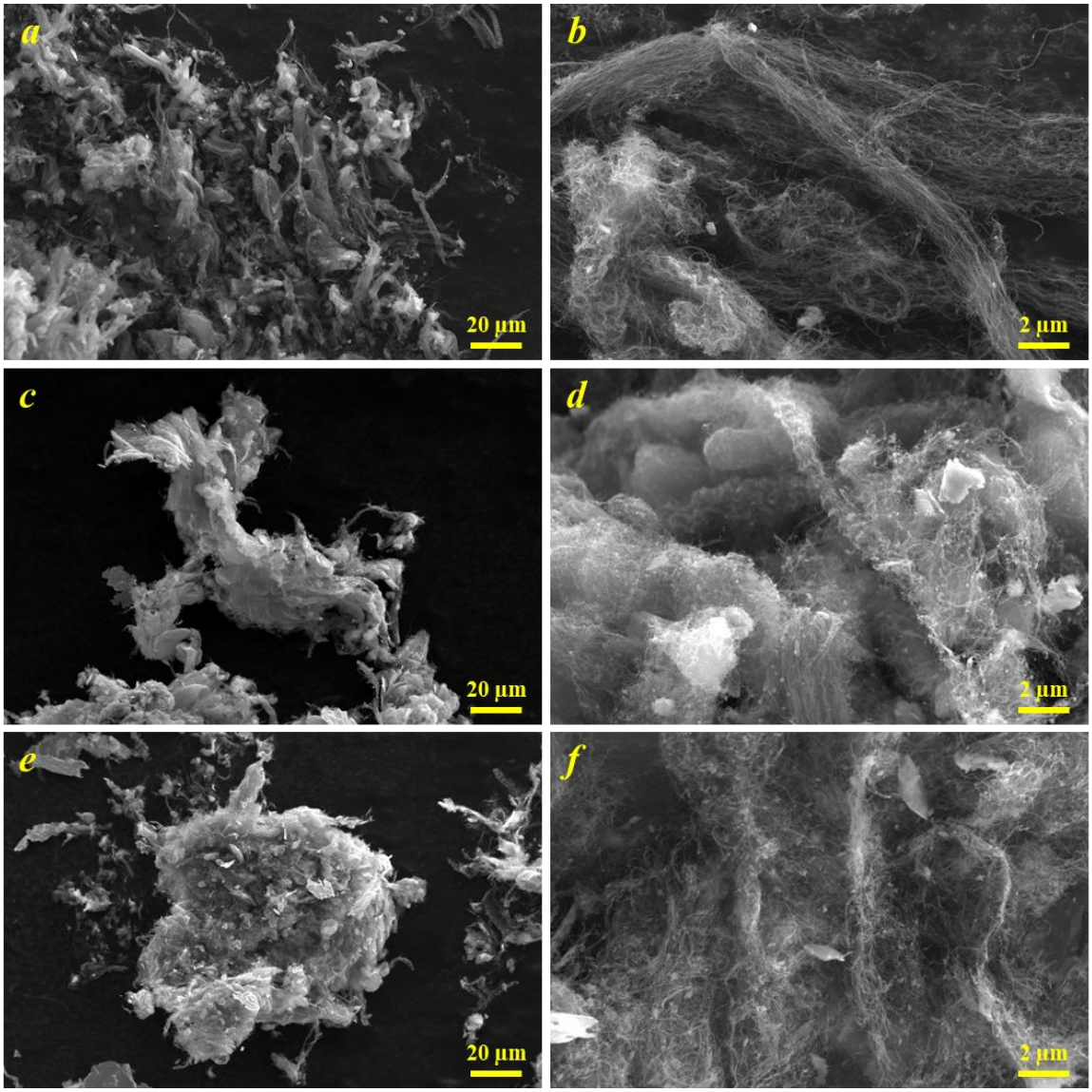

Figure 32: *SEM micrographs of aqueous mechanochemically functionalized VNT100 milled at 300 rpm for (a-b) 30 min, (c-d) 1 hr, and (e-f) 4 hr.*

The morphology of aqueous mechanochemically functionalized VNT100 (afVNT) nanotubes can be seen in Figure 32. The length and bulk morphology of the afVNT nanotubes is much better preserved compared to dfVNT nanotubes. Because the presence of water in the milling vessel introduces a significant drag force on the grinding media, the energy dissipated to the powder upon ball-wall impacts is significantly reduced, thus slowing the kinetics of CNT length reduction. The average length of afVNT nanotubes milled for 30 min is roughly 20 μm and further decreases down to roughly 5-10 μm for 4 hr milling time.

Weight loss and weight loss derivative profiles of aqueous mechanochemically functionalized CNTs are presented in Figure 33. Whereas dfVNTs show consistent weight loss behavior at similar temperatures, afVNTs show seemingly more random thermal degradation behavior. The absence of a weight loss feature below 100 °C suggests there are little to no physiosorbed species on the surfaces of CNTs, whereas the weight loss features in the 150-400 °C range indicate the presence of functional groups. The degree of functionalization of afVNTs is presented in Figure 34 with respect to milling time. Whereas the degree of dry mechanochemical functionalization produces a power law relationship with cumulative milling energy, afVNTs show a linear relationship with milling time. As noted previously, the presence of water in the milling vessel introduces a significant resistance to grinding media kinetic energy, reducing single impact energies and hence E_{cum}. Thus, application of Equations 2-3 in this case would not be valid; however, a linear relationship between θ_f and E_{cum} would be expected for ball milling in water as well assuming an appropriate energy calculation could be performed. While there is some difference in degree of functionalization between 300 rpm and 600 rpm milled for 1 hr, θ_f is nearly equivalent for both rotational speeds at 4 hr milling time, suggesting aqueous mechanochemical functionalization is largely independent of single impact energy within the conditions studied.

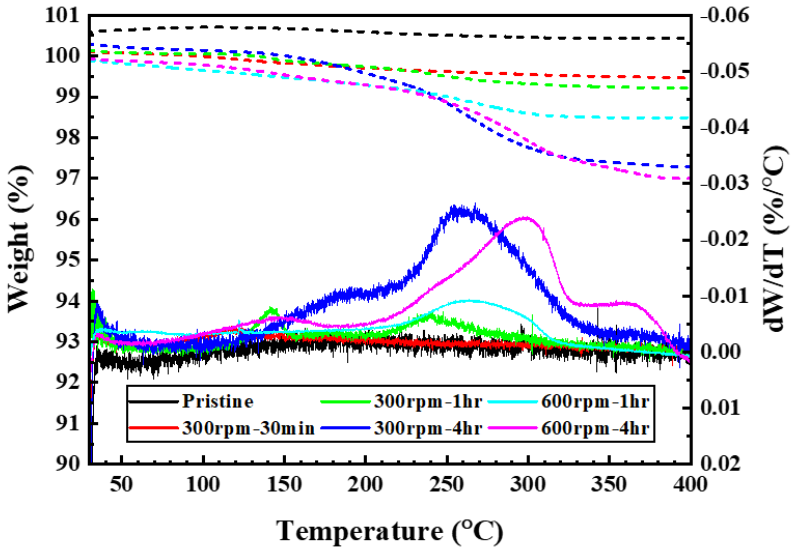

Figure 33: *Thermal degradation behavior of aqueous mechanochemically functionalized VNT100.*

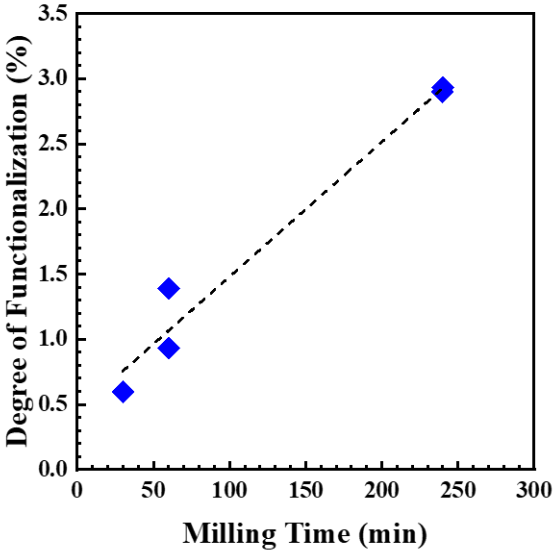

Figure 34: *Degree of functionalization of aqueous mechanochemically functionalized VNT100 correlated to milling time.*

Full XPS surveys and high resolution C1s scans of aqueous mechanochemically functionalized CNTs are presented in Figures 35 and 36 along with C1s peak deconvolution analysis in Table 8. Similar to dry functionalized CNTs, aqueous functionalized CNTs show no

appreciable nitrogen content; only oxygen functionalities appear to be added. Milling at 300 rpm for 30 min for afCNTs results in a notably higher oxygen content compared dfVNTs milled at the same conditions. Further, while dry milling results in XPS contributions from C-O, C=O, and O-C=O binding states, aqueous milling for 30 min and 1 hr results in only C-O and O-C=O contributions, strongly suggesting CNT surfaces are rich with only hydroxyl (R-OH) and carboxyl (R-COOH) groups. Additionally, the elimination of the carbide peak around 283 eV for aqueous functionalized CNTs suggests that wet milling strips the nanotubes from the catalyst sites on vermiculite support, possibly due to the higher shear forces experienced by nanotube bundles during milling in water versus milling in air.

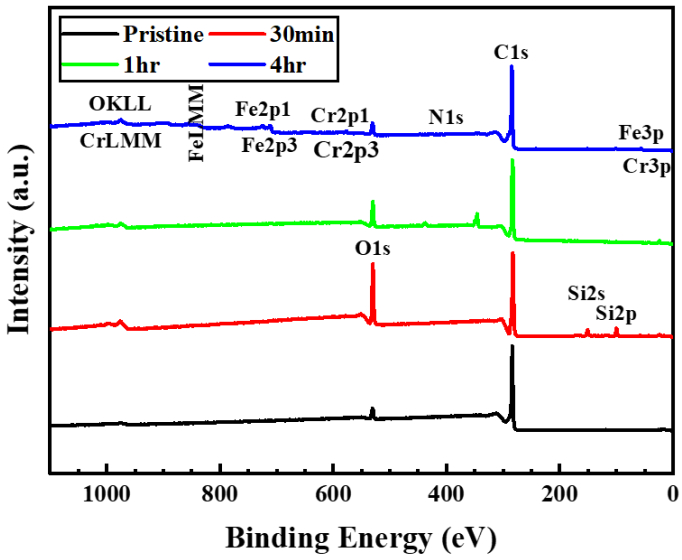

Figure 35: *XPS spectra of aqueous mechanochemically functionalized VNT100.*

Interestingly, the oxygen content of the afVNT nanotubes decreases with increasing milling time. Simultaneously, increasing milling time in an aqueous environment appears to result in the stripping of stainless steel from the grinding media and vessel as evidenced by iron (Fe2p1,

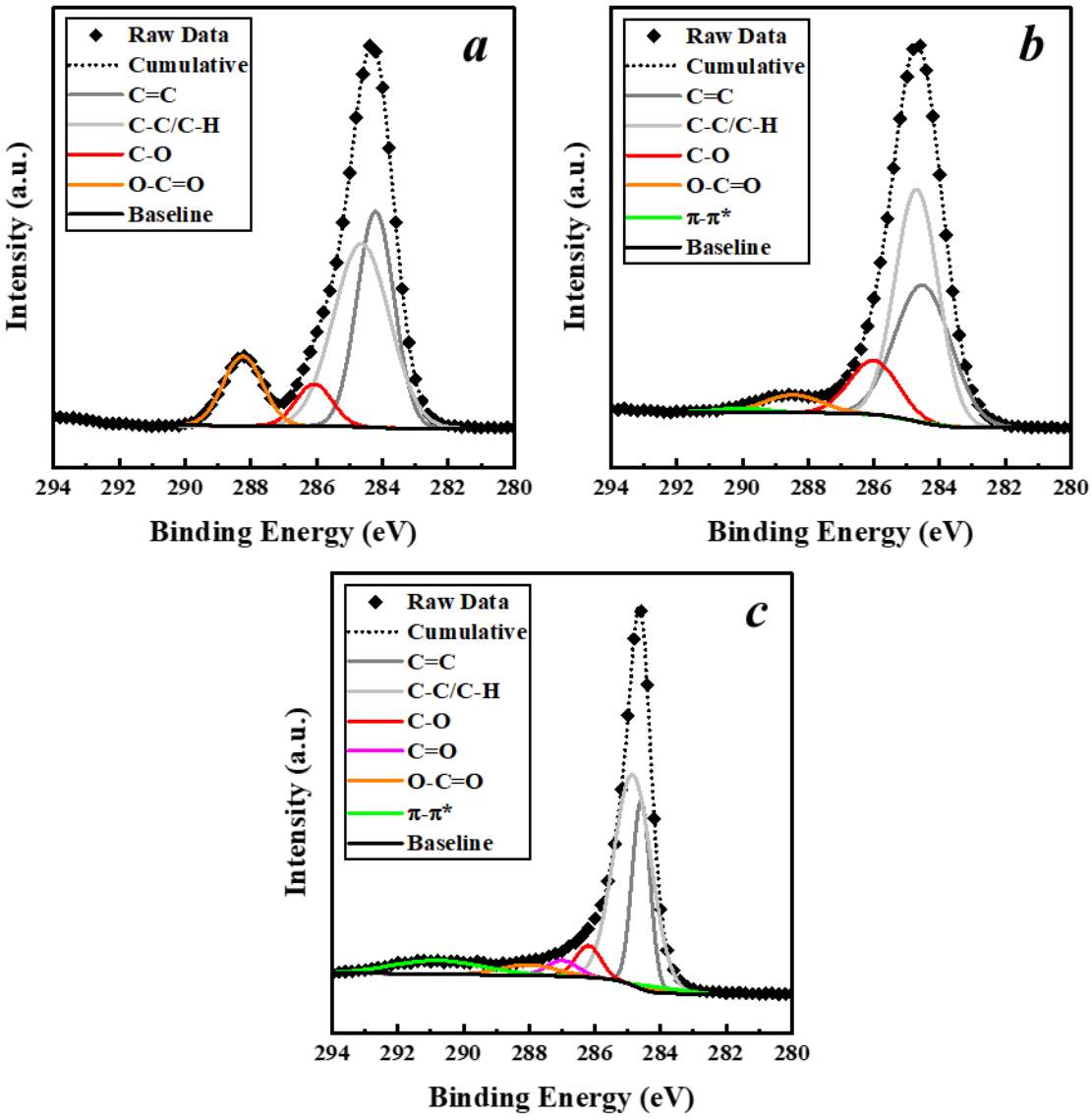

Figure 36: *C1s core level deconvolution for aqueous mechanochemically functionalized VNT100 milled at 300 rpm for (a) 30 min, (b) 1 hr, and (b) 4 hr.*

Fe2p3, Fe3p, and FLMM) and chromium (Cr2p1, Cr2p3, Cr3p, CrLMM) contributions in the XPS spectra. This could explain the small fragments seen throughout Figures 32d and 32f. Contamination in milled CNT samples from stainless steel grinding materials has been reported

previously [133]. Thus, for aqueous milling, short milling times appear to be most beneficial for oxygen content and reduced stainless steel contamination.

Table 8: *C1s peak deconvolution analysis corresponding to Figure 36.*

Species	afVNT (30min)		afVNT (1hr)		afVNT (4hr)	
	eV	at%	eV	at%	eV	at%
C=C	284.2	35.49	284.5	35.69	284.6	23.27
C-C/C-H	284.6	45.56	284.7	46.71	284.8	55.22
C-O	286.1	6.77	286.0	12.12	286.2	5.53
C=O	-	-	-	-	287.0	3.40
O-C=O	288.2	12.19	288.5	4.59	288.0	4.11
π-π*	-	-	290.0	0.88	290.8	8.48
C-M	-	-	-	-	-	-

4.3 Noncovalent mechanochemical functionalization with melamine

Noncovalent mechanochemical functionalization can occur via a variety of interactions such as electrostatic interactions and van der Waals forces. Considering a molecule like melamine, the aromatic triazine ring can participate in π-π stacking with the outer graphitic CNT layer. Fracture of melamine molecules due to mill impacts could also lead to covalent interactions with carbon radicals on CNT surfaces due to CNT fracture, leading to the introduction of nitrogen-containing functional groups, such as amines. Additionally, it is possible that existing functional groups on CNT surfaces, such as carboxylic acid groups, could interact with melamine and undergo a milling-induced partial substitution reaction to transform into an amide, for instance. A

schematic of the proposed noncovalent mechanochemical functionalization method with melamine is presented in Figure 37.

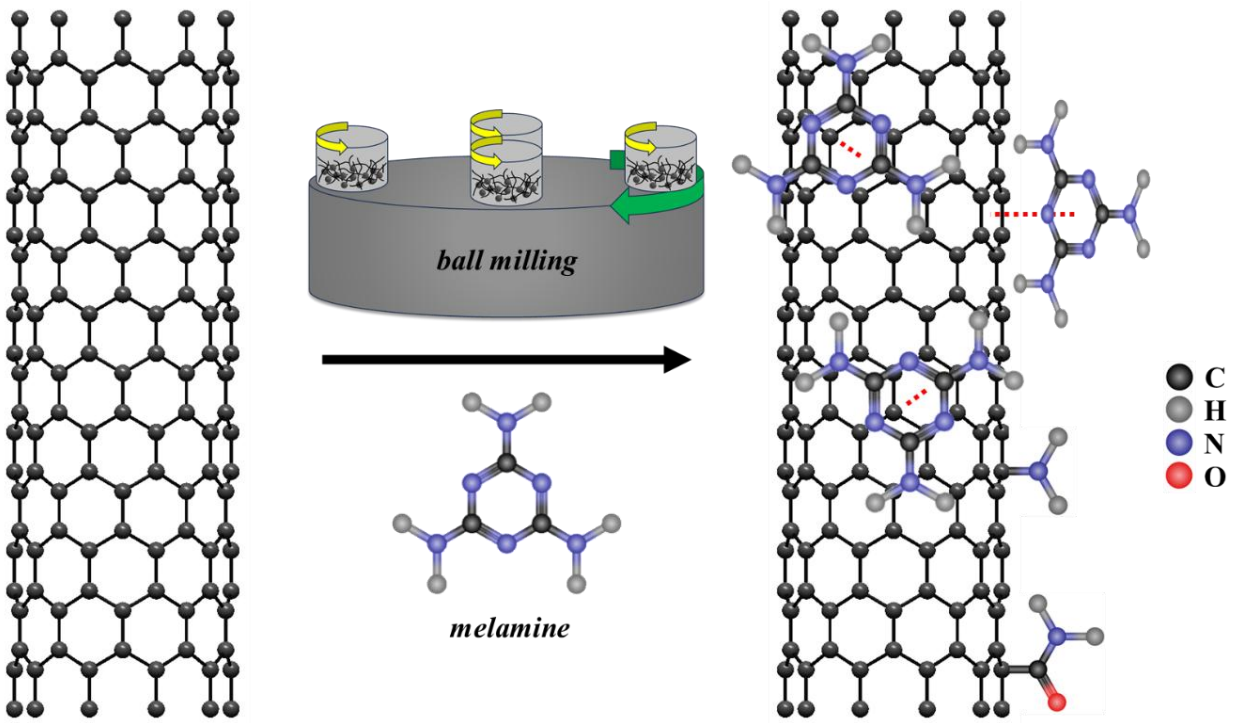

Figure 37: *Schematic of ball milling induced functionalization of CNTs with melamine.*

The morphology of melamine functionalized NC7000 (melNC7000) milled at 300 rpm for varying durations is presented in Figure 38. For melNC7000 milled for 30 min, the length of nanotubes appears to be better retained compared to what would be expected according to length reduction kinetics previously studied. Milling NC7000 for 30 min at 300 rpm (31 mJ/impact) was previously shown to reduce the length of NC7000 to its terminal length of ~400 nm. However, the length of NC7000s milled in the presence of melamine is longer at roughly 800 nm. Thus, the presence of another material in the mill (melamine) appears to slow the kinetics of CNT length reduction, possible due to the formation of a physical barrier protecting the nanotubes. After 1 hr

of milling, however, the length of melNC7000s appears to reach a terminal length of 400 nm, and longer milling durations appear to more densely pack the CNT powder without greatly affecting the length further.

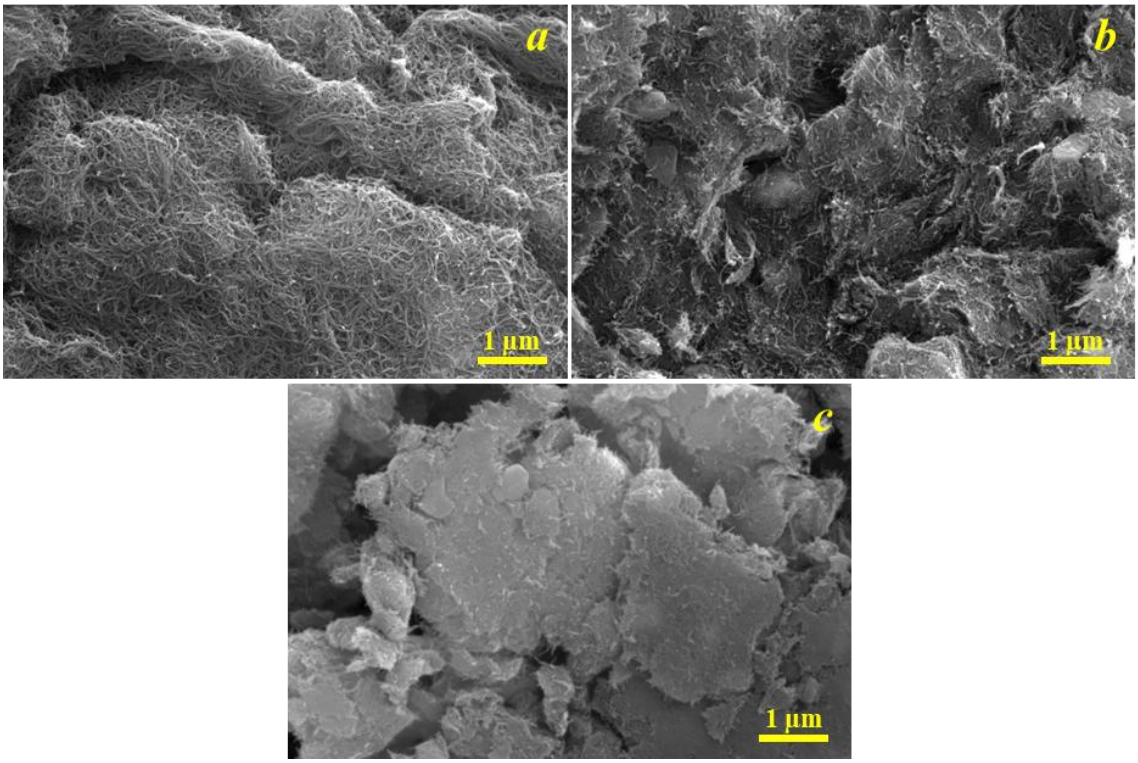

Figure 38: *SEM micrographs of melamine functionalized NC7000 milled at 300 rpm (31 mJ/impact) for (a) 30 min, (b) 1 hr, and (c) 4 hr.*

The thermal degradation behavior of melNC nanotubes is presented in Figure 39. The degradation temperature of pure melamine is approximately 330 °C. The thermal degradation of pristine NC7000 is negligible up to high temperatures, similar to that of pristine VNT100. Milling NC7000 in the presence of melamine results in three distinct weight loss features. Small weight loss features below 100 °C are indicative of desorption of adsorbed moisture, like how dfVNT nanotubes displayed evidence of adsorbed species. Between 200-350 °C, melNC nanotubes

display significant weight loss indicative of the degradation of melamine that is π-π stacked on NC7000 surfaces. The amount of weight loss in this region scales with milling time. The percent weight loss corresponding to the melamine content of melNC milled for 30 min, 1 hr, and 4 hr is 5.8 wt%, 9.8 wt%, and 13.9 wt%, respectively. Finally, each mechanochemically functionalized NC7000 sample displays a small weight loss feature at higher temperatures between 400-500 °C, possibly indicative of the formation of covalently bonded functional groups as a result CNT and melamine cleavage. This weight loss feature at higher temperatures also scales in size with milling time, indicating the degree of functionalization increases with cumulative impact energy.

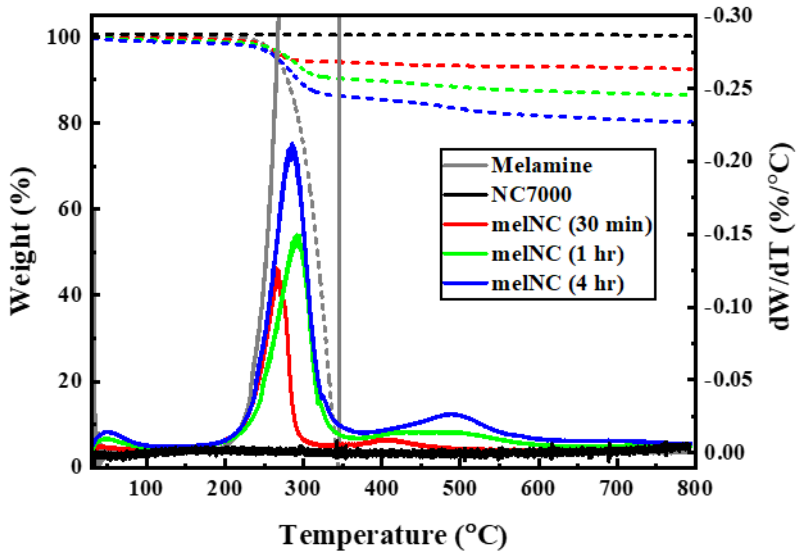

Figure 39: *Thermal degradation behavior of melNC CNTs.*

XPS spectra of melNC nanotubes milled for varying durations are presented in Figure 40. High resolution C1s scans are presented in Figure 41, and the corresponding deconvolution analysis is given in Table 9. Pristine NC7000s show low oxygen content as expected based on the lack of thermal degradation in TGA curves. The initial oxygen content of pristine NC7000 can be

attributed to a variety of moieties including hydroxyl (R-OH), ketone (R=O), and carboxyl (R-COOH) groups, as evidenced by Figure 41a. Upon milling NC7000 in the presence of melamine

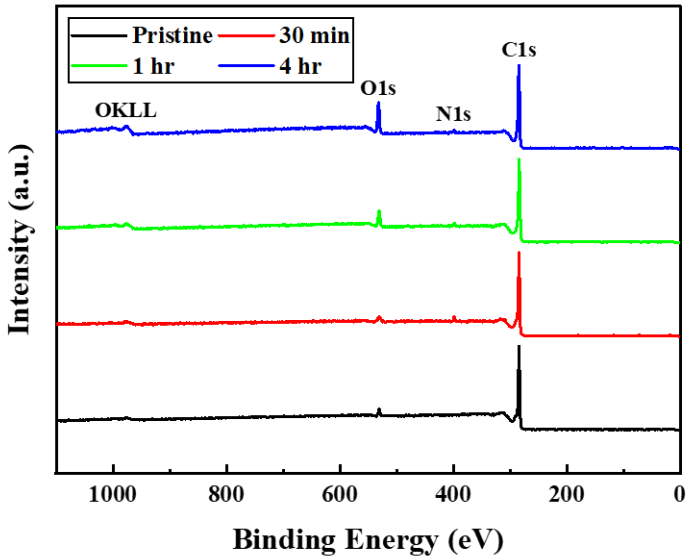

Figure 40: *XPS spectra of NC7000 CNTs mechanochemically functionalized with melamine.*

for 30 min, the oxygen content does not change. However, increasing milling time upwards of 4 hr does result in a notable increase in oxygen content. Because melamine contains no oxygen, it can be assumed that ambient oxygen participates in the formation of functional groups on CNT surfaces. For milling NC7000s with melamine, a small but clear contribution from N1s appears in the XPS spectra, likely indicative of the presence of melamine on CNT surfaces. In these cases, the peaks assigned to C-O (285.9-286.1 eV), C=O (270.0-270.4 eV), and O-C=O (288.4-289.0 eV) binding states can also be attributed to C-N, C=N, and N-C=N binding states. These contributions likely arise from the amine groups and triazine ring of adsorbed melamine. Additionally, these peaks may include contributions from covalently bonded nitrogen groups on CNT surfaces, such

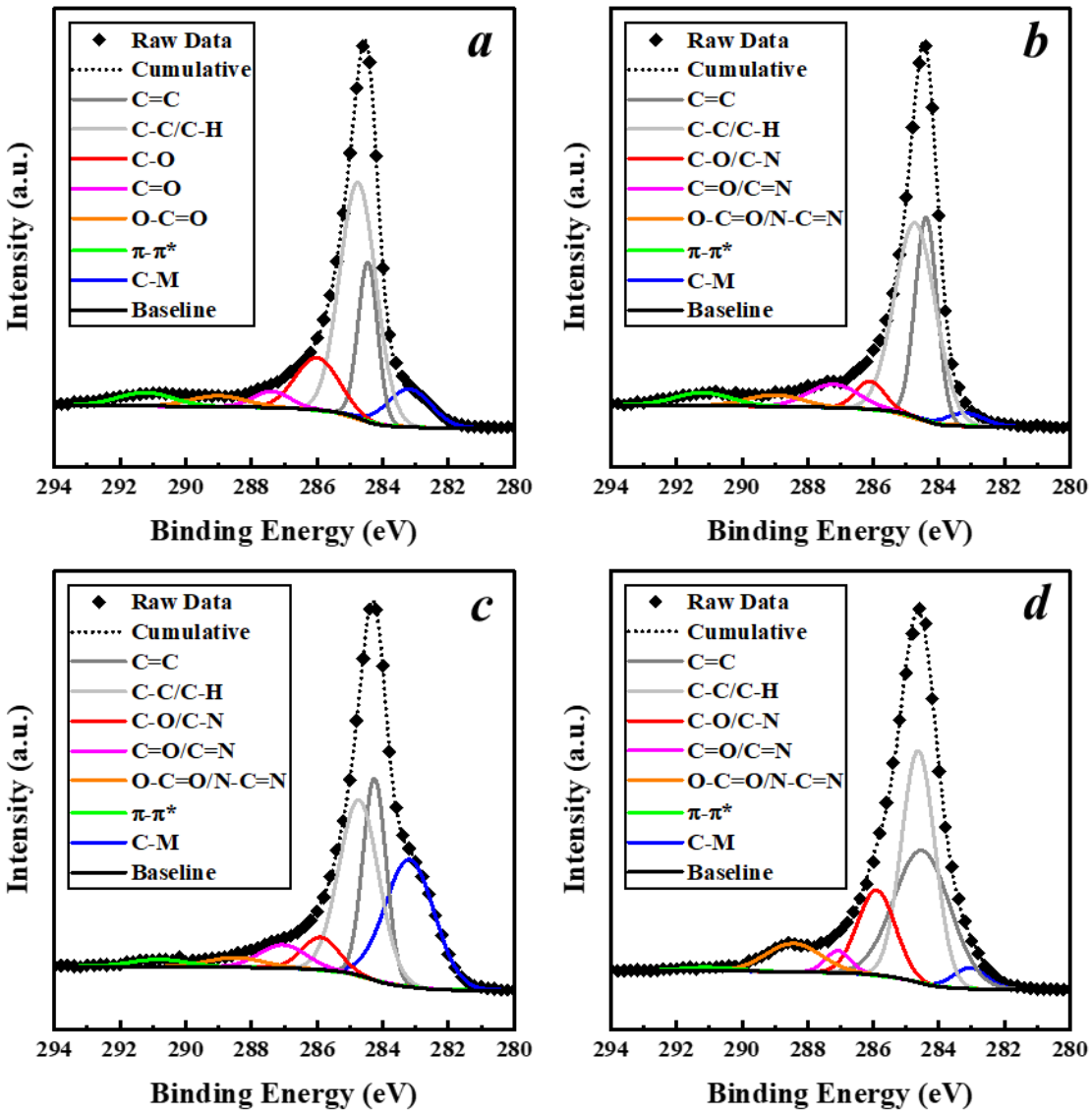

Figure 41: *C1s deconvolution for (a) pristine NC7000 and (b-d) melNC milled at 300 rpm for (a) 30 min, (c) 1 hr, and (d) 4 hr.*

as amines and amides; however, decoupling nitrogen contributions from the melamine molecule and from surface groups cannot easily be achieved. Because the oxygen content was seen to increase with milling time, it can be assumed that covalently bonded functional groups on CNT surfaces are mostly oxygen rich with some contribution from nitrogen. While NC7000 nanotubes

are purified by the manufacturer, there still may be catalyst particles (Fe, Co, etc.) present, as evidenced by the presence of a C-M peak around 283.0-283.2 eV. The variability of the carbide peak magnitude may be explained by the uneven distribution of catalyst particles throughout the carbon nanotube sample, thus changing drastically depending on the sampling area chosen during spectral acquisition.

Table 9: *C1s peak deconvolution of melamine functionalized NC7000.*

Species	NC7000		melNC (30min)		melNC (1hr)		melNC (4hr)	
	eV	at%	eV	at%	eV	at%	eV	at%
C=C	284.5	17.87	284.3	27.54	284.3	22.19	284.5	34.74
C-C/C-H	284.8	48.49	284.7	48.89	284.7	32.96	284.6	36.16
C-O/C-N	286.0	12.98	286.1	4.93	285.9	5.60	285.9	14.96
C=O/C=N	287.4	3.45	287.2	7.32	287.0	5.16	287.1	2.57
O-C=O/N-C=N	289.0	3.47	289.0	3.90	288.5	2.52	288.4	7.33
π-π*	291.2	4.24	291.2	4.39	290.8	1.90	291.1	0.95
C-M	283.2	9.49	283.2	3.03	283.1	29.68	283.0	3.28

4.4 Mechanochemical sulfur-doping for vulcanized rubber additives

The modification of graphene derivatives with sulfur has been studied previously for applications in batteries and vulcanized rubber composites [134, 135]. Mechanochemical functionalization of carbon nanotubes by milling in the presence of elemental sulfur can decompose S_8 rings and allow for the interaction of these shortened sulfur molecules or individual sulfur molecules with carbon radicals formed from CNT fracture, thus creating covalent carbon-

sulfur bonds in the forms of thiols (R-SH) or thioketones (R=S). Sulfur can also be incorporated into the CNT backbone in the form of thioethers/sulfides (R-S-R). Given that ambient oxygen has previously been shown to participate in CNT mechanochemical functionalization, the formation of oxygen containing sulfur groups like sulfoxides (R-SO-R) and thiocarboxylic acids (R-COSH/CSOH) is also plausible. Additionally, milling sulfur with graphite has shown to result in a large degree of physically adsorbed sulfur on graphitic surfaces without covalent interaction with carbon [98]. A schematic of the proposed mechanochemical functionalization method with sulfur is presented in Figure 42.

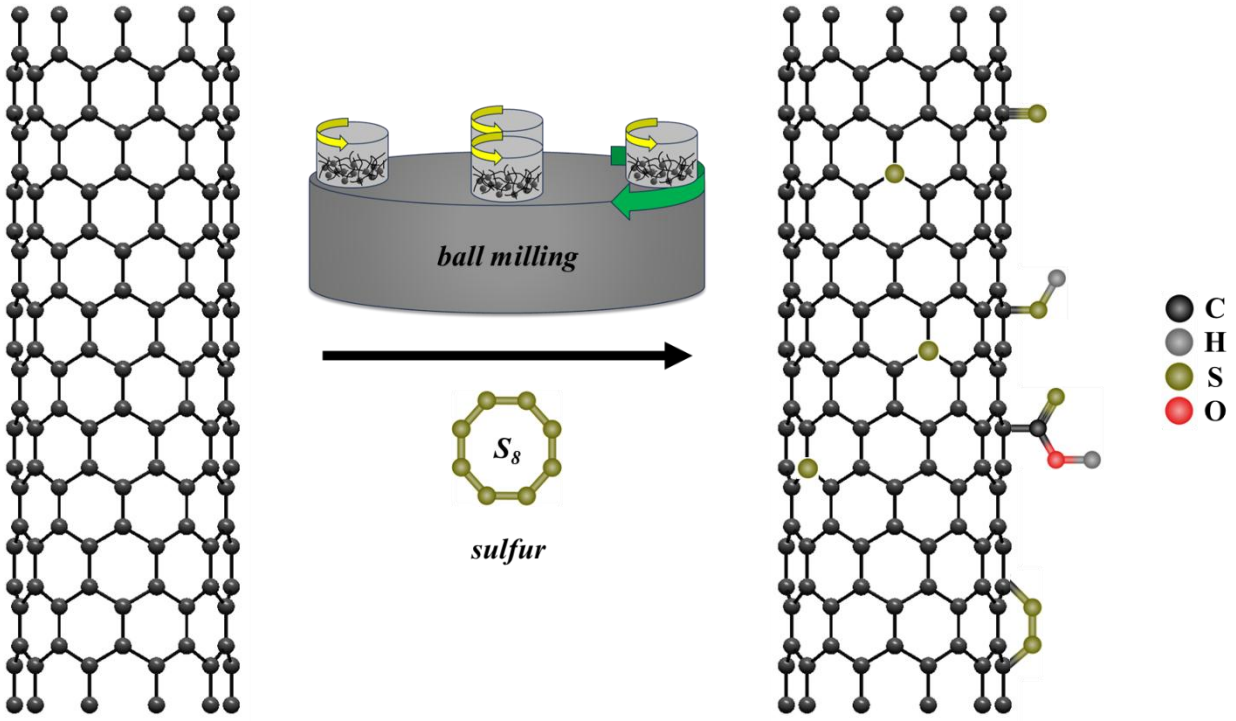

Figure 42: *Schematic of ball milling induced functionalization of CNTs with sulfur.*

The morphology of CNTs mechanochemically functionalized with sulfur is presented in Figure 43. Upurified sNC powder shows good mixing between sulfur and NC7000 nanotubes, and

the diameters of the CNTs appear larger than the measured value (11 nm), suggesting a coating of sulfur has been added (Figure 43a). After purification, sNC CNTs show evidence of length reduction down to roughly 700 nm due to milling (Figure 43b); however, the extent of length reduction is less than would be expected based on kinetics previously discussed in Chapter 3. Additionally, purified sVNT nanotubes exhibit length reduction down to approximately 20 µm bundle lengths (Figure 43c), which is much larger than would be expected based on 1 hr milling (refer back to Figure 18). Thus, the presence of sulfur in the milling vessel likely slows the kinetics of CNT length reduction, acting as a physical barrier from impact induced fracture. These findings show similar agreement with the effects of milling CNTs with melamine as shown previously.

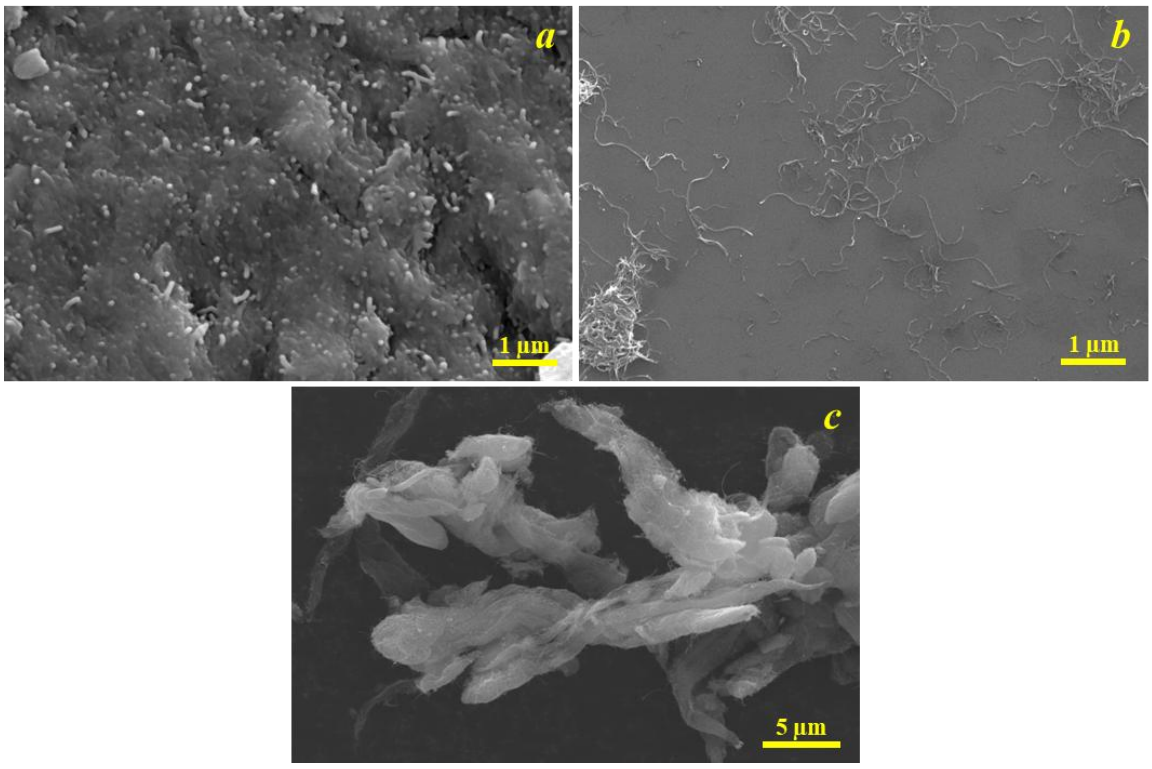

Figure 43: *SEM micrographs of (a) unpurified sNC, (b) purified sNC, and (c) purified sVNT.*

Figure 44 presents the thermal degradation behavior of mechanochemically sulfur functionalized VNT100. Elemental sulfur (S_8) fully decomposes between roughly 150 and 330 °C. For unpurified sVNT100 milled at a 1:1 mass ratio for 1 hr at 300 rpm, a significant weight loss feature is seen between 150 and 380 °C, which is indicative of the full decomposition of the sulfur portion of the composite sVNT-sulfur powder. The residual weight of unpurified sVNT is nearly 50%, confirming the 1:1 milling ratio. Upon purification of sVNT with carbon disulfide, it is found that roughly 80% of the sulfur in the milled composite sVNT-sulfur powder is extractable as evidenced by only a 10% weight loss feature for purified sVNT (10% weight loss translates to 20% of the milled sulfur applying the 1:1 milling ratio). Similar to the melamine functionalized CNTs, the fraction of sulfur remaining after extraction of free sulfur can represent both physically adsorbed sulfur and sulfur-containing functional groups.

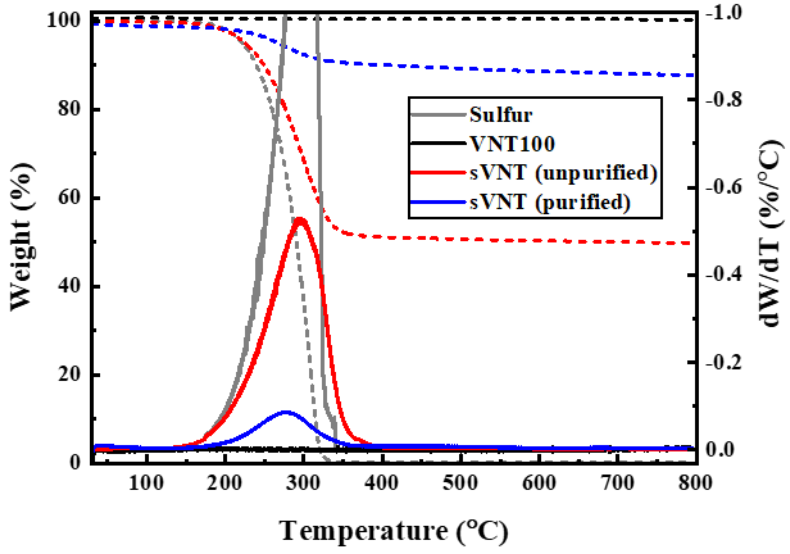

Figure 44: *Thermal degradation behavior of sVNT CNTs milled at 300 rpm (31 mJ/impact) for 1 hr.*

Figure 45 presents FTIR spectra of pristine and mechanochemically sulfur functionalized VNT100. The peak at 480 nm^{-1} represents S-S stretching, possibly arising from adsorbed elemental sulfur or from multiple sulfur molecules covalently attached to the CNT surface (e.g., C-S-S-C). The slight peak at 660 cm^{-1} could be indicative of C-S stretching, while the stronger peak at 1070 likely indicates C=S stretching [136]. Because all CNTs contain some amount of oxygen content, signal in the 1000-1200 cm^{-1} can also be an indication C-O stretching. However, because pristine VNT100 shows little to no signal in this range, the peak in the sVNT spectra can be attributed to C=S. It should be noted that the apparent transmission signals displayed in the 2000-2500 cm^{-1} range are an artifact of the measurement and/or instrument that varied significantly from sample to sample and do not accurately represent the chemical composition of the CNTs.

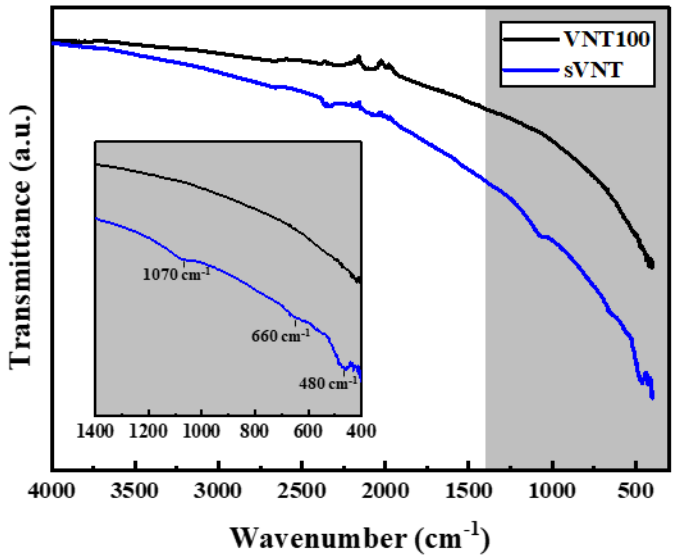

Figure 45: *FTIR spectra of pristine VNT100 and purified sVNT.*

A full XPS survey as well as deconvoluted high resolution C1s and S2p scans of sulfur functionalized VNT100 are presented in Figure 46. In Figure 46a, the oxygen content of the sulfur

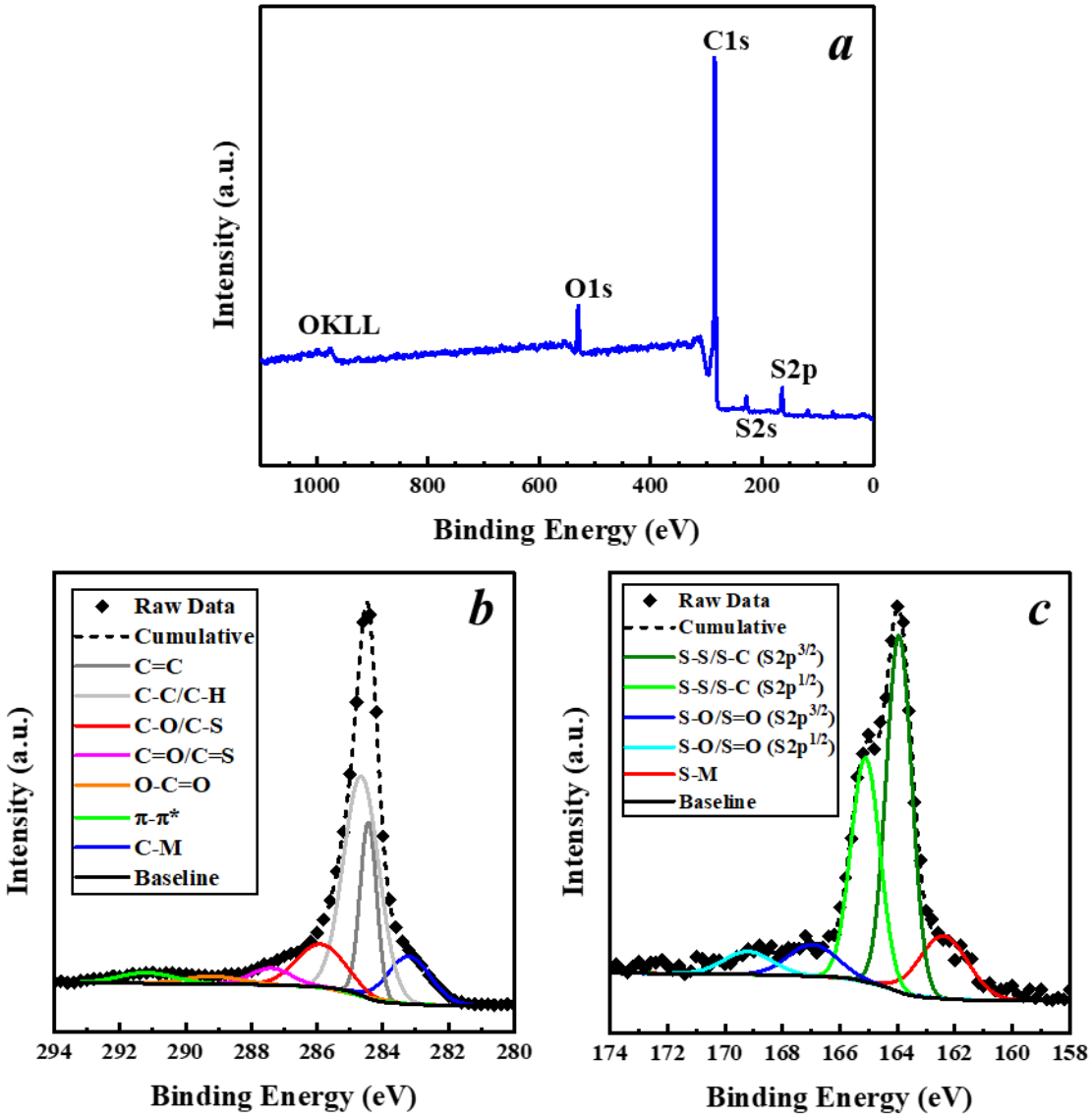

Figure 46: *(a) Full XPS spectra and high resolution (b) C1s and (c) S2p scans of sVNT.*

functionalized VNT100 is marginally increased relative to the pristine VNT100 (presented earlier), but there are clear contributions from sulfur as evidenced by S2s and S2p peaks. In Figure 46b, the peaks associated with C-O (285.9 eV) and C=O (287.4) binding states can also be assigned to C-S and C=S, respectively. The elevated C-O/C-S peak relative to pristine VNT100 could indicate the formation of additional hydroxyl groups (R-OH) as well as thiol (R-SH) or thioether (R-S-R)

groups. Figure 46c presents the S2p core level deconvolution displaying typical spin orbital splitting ($S2p^{3/2}$ and $S2p^{1/2}$). The primary peaks located at 163.9 eV and 165.1 can be assigned to both S-S and S-C. The two peaks at higher binding energies, 167.0 eV and 169.2 eV, are indicative of sulfur oxidation, either in the physically adsorbed state, i.e., adsorbed sulfur dioxide (SO_2), or as functional groups covalently bonded to the CNT surface, i.e., thiocarboxyl (R-COSH) or sulfoxide (R-SO-R) groups. While decoupling the adsorbed sulfur from the covalently bonded sulfur is difficult to assume from XPS spectra, the small contributions from C-S and C=S from FTIR spectra confirm these signals can be partially attributed to sulfur covalently bonded to CNT surfaces. An additional peak located at 162.2 eV could be indicative of the formation of metal sulfides. Existing catalyst particles (Fe and Co) as well as vermiculite support (Si and Al) in the pristine VNT100 can interact with elemental sulfur during milling and form metal sulfides. The mechanochemical synthesis of metal sulfides via co-milling of metals/metal complexes and elemental sulfur has been reported previously [137, 138].

Chapter 5: Aspect ratio and surface chemistry effects on polycarbonate-nanotube composites

5.1 Compounding

The primary concern in processing polymer composites with ultrahigh aspect ratio fillers is the possibility of high melt viscosities, which can lead to overloading the extruder motor and polymer degradation. Figure 47 shows the screw torque curves recorded during compounding for composites with 5 wt% CNTs, and Figure 48 shows the relationship between CNT length and melt viscosity at ejection according to software provided by the manufacturer. Incorporation of 5 wt% VNT100* in PC nearly reaches the screw force limit for the laboratory scale micro compounder (4000 N) and the viscosity at ejection is 0.93 kPa·s. This result confirms our initial hypothesis that the large agglomerate morphology and ultrahigh aspect ratio of the CNTs could impart high melt viscosities, resulting in processing difficulties. High energy ball milling for CNT length reduction before compounding leads to notable drops in melt viscosity. For 50% nanotube length reduction (mVNT50), the viscosity is reduced by 26% to 0.69 kPa·s (PC-mCNT50). Further reducing nanotube length to 20 μm results in a 52% reduction in melt viscosity to 0.45 kPa·s relative PC-VNT100*. Remarkably, while the initial viscosity of PC-mVNT5 is higher than neat PC in the initial stages of mixing as expected, the melt viscosity at ejection for PC-mCNT5 is similar to neat PC (~0.39 kPa·s), a 58% reduction relative to the dCNT100 composite. Additionally, the mechanochemically functionalized CNTs (afVNT20 and dfVNT5) show similar viscosity to their plain milled counterparts with similar aspect ratios, suggesting surface chemistry does not greatly affect polymer-CNT melt viscosity. Previously discussed models relating filler aspect ratio to suspension viscosity significantly overestimate the aspect ratio contribution to increased melt

viscosity relative to the neat polymer found here experimentally, likely due to a combination of factors including non-ideal dispersion and nanotube curvature.

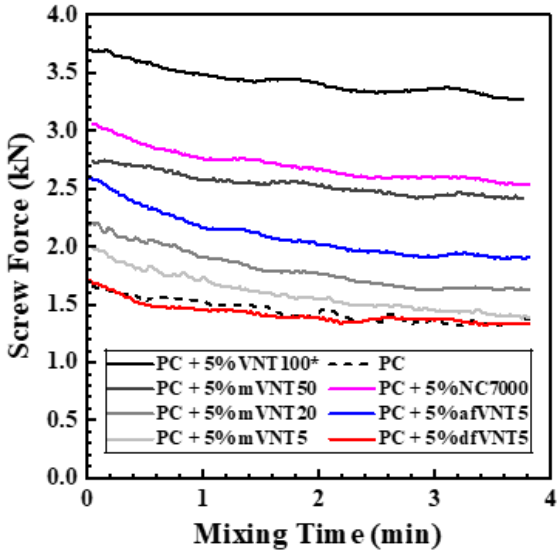

Figure 47: *Screw torque curves recorded during PC-CNT compounding.*

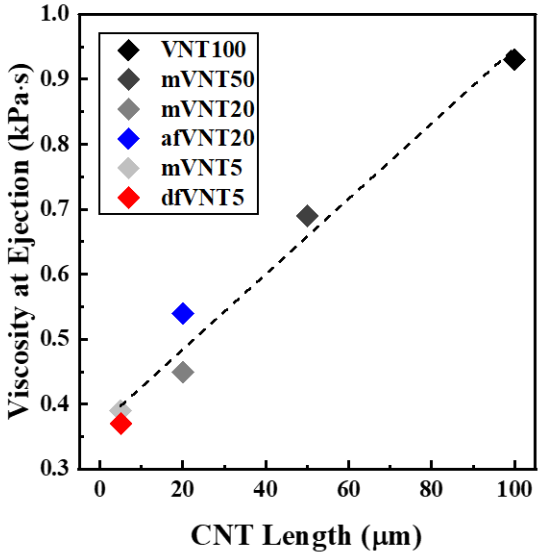

Figure 48: *Linear relationship between CNT length and composite melt viscosity at ejection.*

Interestingly, pristine NC7000 CNTs result in a significantly higher melt viscosity (0.71 kPa·s) compared to all ball milled CNT composites despite having a significantly lower aspect ratio, suggesting the ball milling procedure induces additional morphology changes other than aspect ratio reduction that directly affect melt processability. According to optical micrographs in Figure 49, ball milling significantly reduces the agglomeration of the CNTs in the composites. Pristine VNT100 in PC show a wide distribution of agglomerate sizes with many large agglomerates on the order of 50 µm in diameter as seen in Figure 49a. The original nanotube bundle morphology can even be observed, as seen in Figure 49b. Interestingly, while low energy milling does not reduce the length of the CNTs, the resulting agglomerate size in PC is noticeably

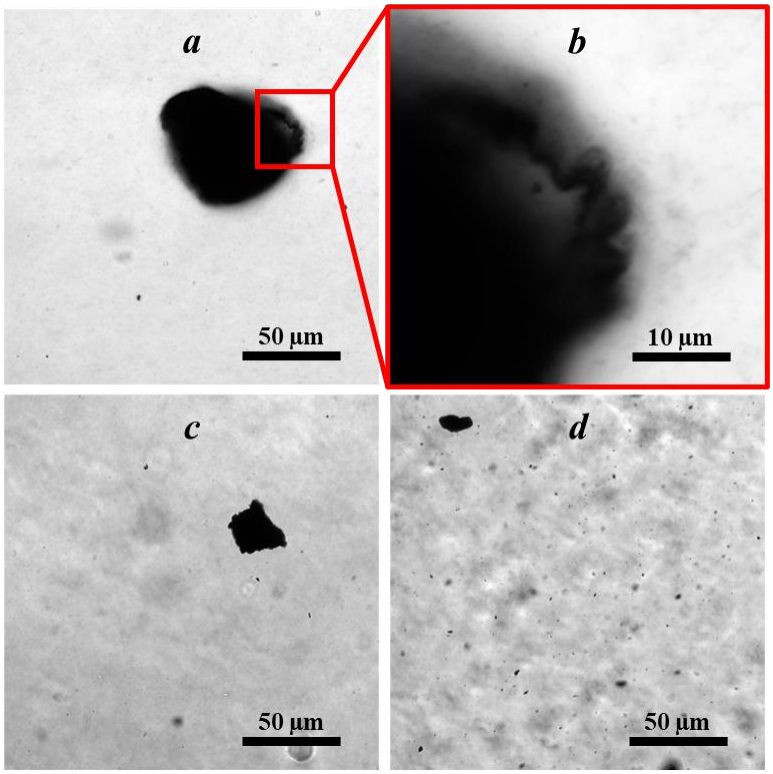

Figure 49: *Optical micrographs of PC filled with 0.1 wt% (a-b) VNT100, (c) VNT100*, and (d) mVNT5.*

decreased, as seen in Figure 49c. This observation could be explained by the disruption of multilayered CNT arrays separated by thin vermiculite sheets. Milling at high energies further reduces agglomerate size to approximately 1 μm, as seen in Figures 49d.

SEM micrographs of cryo-fractured PC-CNT composites shown in Figure 50 elucidate information about individual level CNT dispersion. The size of agglomerate (~50 μm) seen in Figure 50a for PC-VNT100 parallels that seen in Figure 49a. Additionally, vermiculite sheets with the bases of grown carbon nanotubes can be seen in Figure 50b, suggesting nanotubes do not easily strip off vermiculite surfaces during compounding. Rather, to disperse individually in the polymer as seen in the areas surrounding the vermiculite sheets, nanotubes must fracture at some point along their length to dislodge themselves from the vermiculite support. Agglomerate size reduction down to ~1 μm for ball milled nanotubes is also evident in Figures 50c-d. However, the individual level CNT dispersion appears to be worse than that of VNT100 comparing Figure 50b to Figure 50d. Interestingly, dfVNT5 nanotubes display larger agglomerates (~10 μm) than mCNT5 as seen in Figure 50e; however, the individual level of dispersion is significantly improve as evidenced by Figure 50f. The afVNT20 nanotubes show similar agglomerate size to mVNT5 on the order of 1 μm but also display a much higher density of individual CNTs in the areas surrounding the small agglomerates, suggesting a higher degree of dispersion compared to mVNT5. The parallel reductions in CNT agglomeration and melt viscosity show promise for using planetary ball milling to significantly improve the processability of initially ultrahigh aspect ratio CNTs in polymers and allow for high carbon loadings (i.e., masterbatch applications); however, the effects of individual CNT dispersion on composite properties warrant further study.

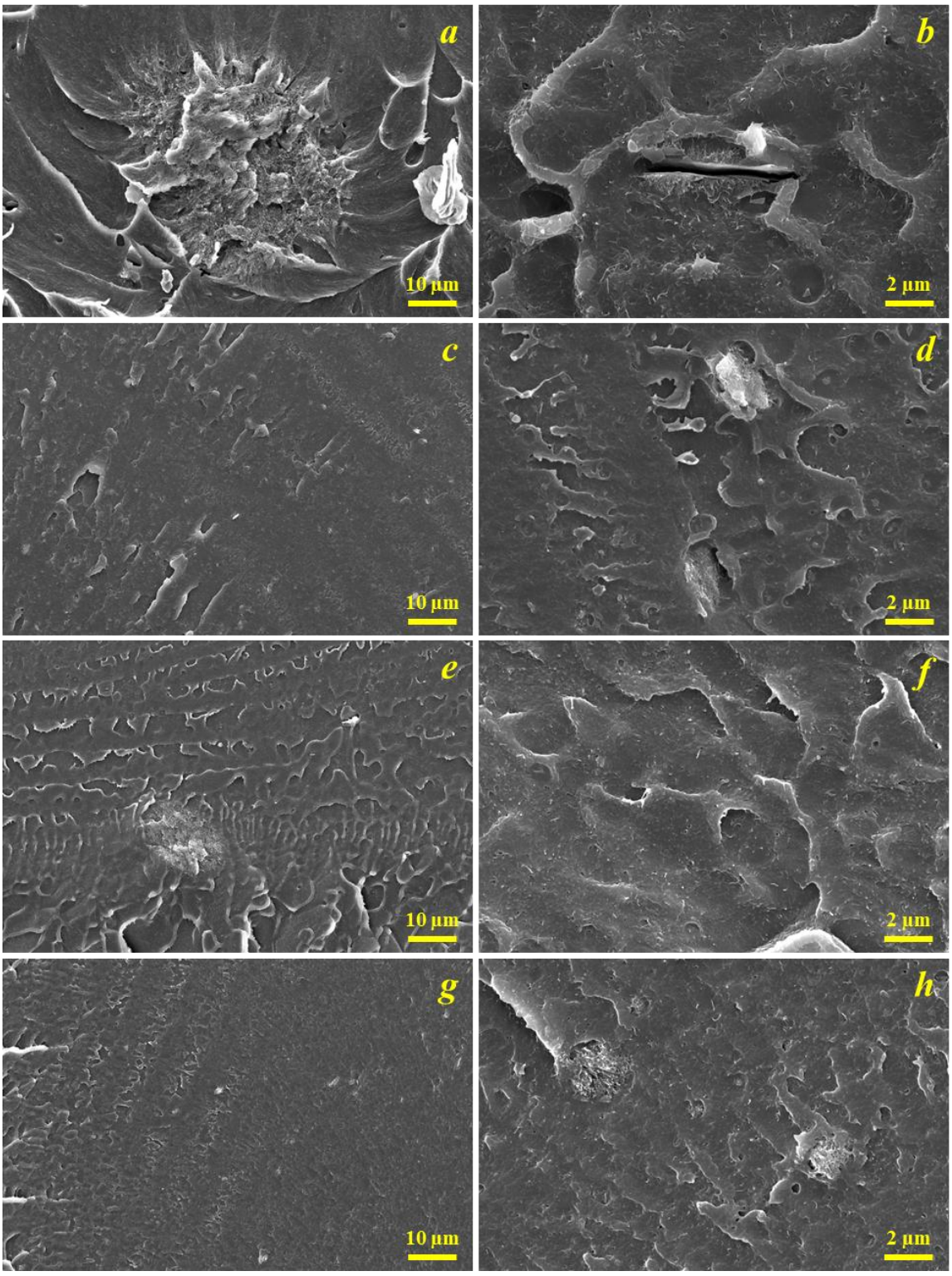

Figure 50: *SEM micrographs of PC filled with 2 wt% (a-b) VNT100, (c-d) mVNT5, (e-f) dfVNT5, and (g-h) afVNT20.*

5.2 Percolation behavior

5.2.1 Aspect ratio effects

Storage modulus, loss modulus, and complex viscosity curves for PC composites filled with varying amounts of VNT100 are given in Figure 51. The complex viscosity of neat PC displays typical shear thinning behavior at high shear (greater than 10^2 rad/s) and a Newtonian plateau at low shear. The storage modulus of neat PC shows slight plateauing behavior with decreasing angular frequency, which is an initially surprising result given that most thermoplastics exhibit a steady decrease in storage modulus at low shear. This result could be explained by competing degradation and crosslinking of PC during compression molding at high temperatures (280 °C). The formation of a crosslinked network would likely result in an increase in molecular weight and subsequently storage modulus. Proposed mechanisms of the thermal crosslinking of polycarbonate include, but are not limited to, unselective free radical crosslinking [139], branching via peroxide formation [140], and hydrolysis from trace ambient moisture followed by recondensation at added carboxyl group sites (forming ester linkages) [141, 142]. Figure 52 presents multiple oscillation frequency sweep tests run consecutively on a single neat PC sample at 280 °C. The steadily increasing storage modulus at low shear for each successive test suggests a higher degree of crosslink formation as the time at elevated temperature increases. To further demonstrate this effect, the same frequency sweeps were conducted at a lower temperature (260 °C), for which little to no change in storage modulus is detected for consecutively run tests as seen in Figure 52b, suggesting a temperature dependence. The plateauing behavior of storage modulus at low shear and temperature dependence has been reported previously for various grades of polycarbonate [143, 144].

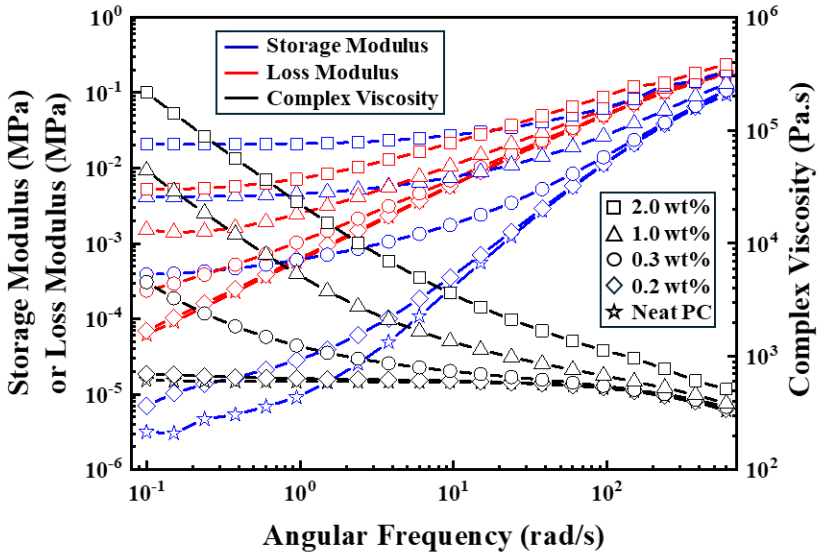

Figure 51: *Oscillation frequency sweep curves of PC-VNT100.*

Upon addition of 0.2 wt% VNT100 to PC, the rheological properties of the composite, primarily complex viscosity and loss modulus, are largely unchanged. Increasing VNT100 content from 0.2 wt% to 0.3 wt% results in a significant shift from viscous to solid like behavior of the composite at low shear as evidenced by the crossover of storage and loss modulus at ~0.3 rad/s. Consequently, the complex viscosity deviates from the typical Newtonian plateau behavior at low shear rates and rather increases significantly. Continuing to increase VNT100 content upwards of 2 wt% results in a nearly straight-line complex viscosity increase with decreasing shear rate, along with a nearly four orders of magnitude increase in storage modulus at low shear relative to neat PC.

Because the storage modulus at low shear is particularly sensitive to CNT percolation, plotting storage modulus against CNT content can aid in the identification of the rheological percolation threshold. Figure 53 presents the storage moduli of PC-CNT composites at low shear

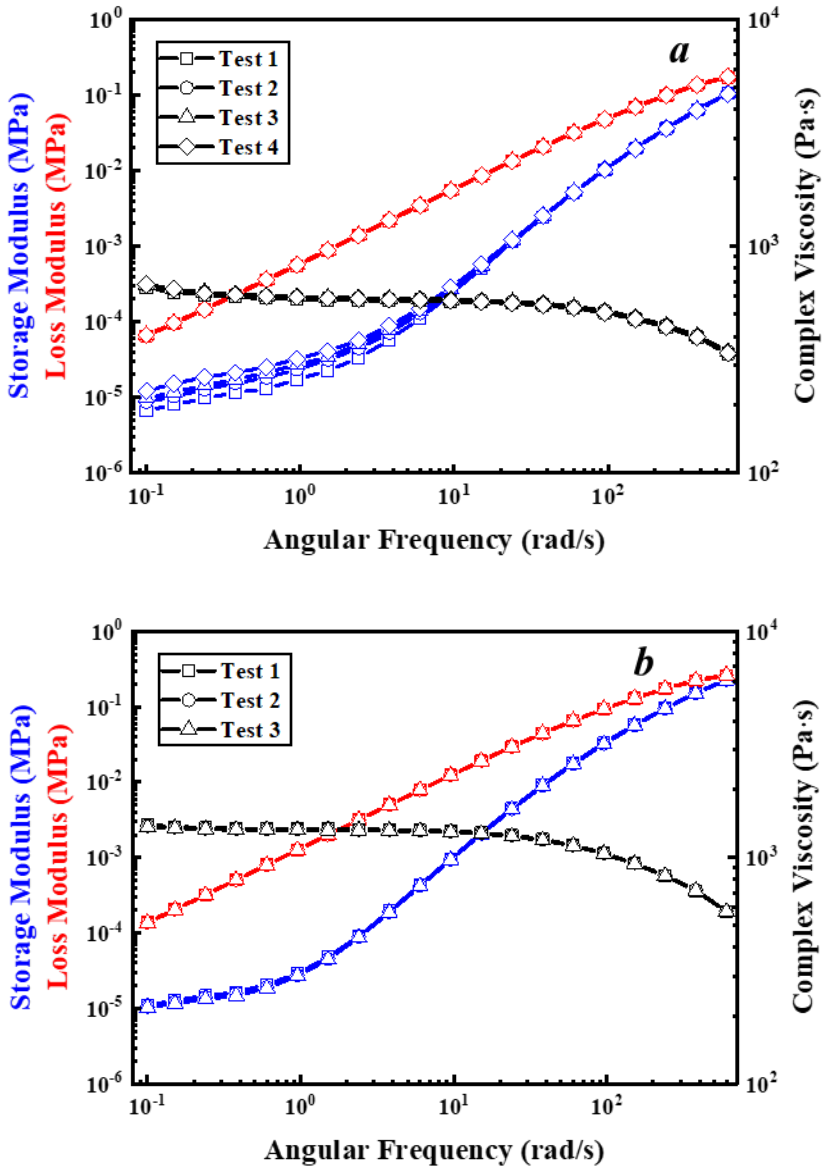

Figure 52: *Consecutive oscillation frequency sweep tests on neat PC at (a) 280 °C and (b) 260 °C.*

rates (0.1 rad/s) versus CNT content for pristine and milled CNTs along with power law fits according to Equation 8 (fitting parameters in Table 10). Both PC-VNT100 ($\varphi_{c,G'}$ = 0.18 wt%) and PC-VNT100* ($\varphi_{c,G'}$ = 0.20 wt%) show similar rheological percolation behavior, confirming that aspect ratio is preserved during low energy ball milling. However, the storage moduli, and

consequently the complex viscosities, of PC-VNT100* composites at CNT contents above the percolation threshold are significantly reduced compared to PC-VNT100. Thus, given that PC-VNT100* nearly reached the screw torque limit for the laboratory scale micro compounder, compounding the pristine ultrahigh aspect ratio VNT100 nanotubes in PC at contents near 5 wt% would be near impossible due to the torque limitation. The rheological percolation threshold for mVNT50 ($\varphi_{c,G'}$ = 0.23 wt%) is not very different than those for VNT100 and VNT100*, indicating that Equation 4 does not apply in this case. But for other samples, the scaling relationship implied by Equation 4 roughly holds when mCNT20 ($\varphi_{c,G'}$ = 0.62 wt%) and mCNT5 ($\varphi_{c,G'}$ > 3 wt%) are compared to mCNT50.

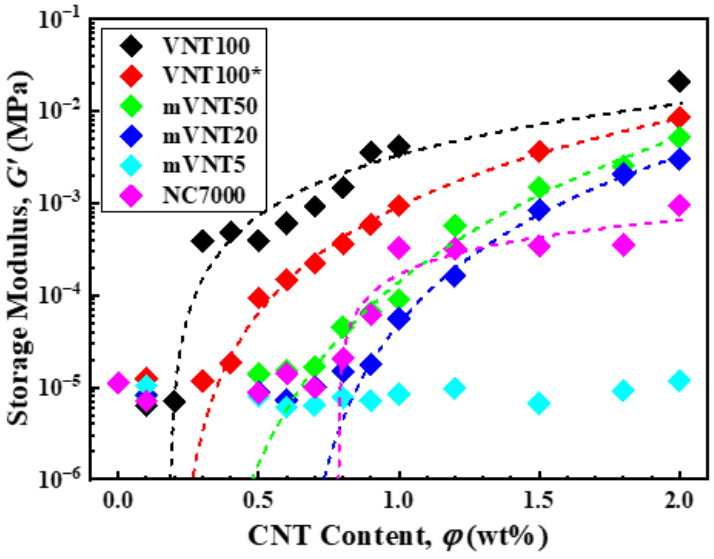

Figure 53: *Rheological percolation behavior of CNTs in polycarbonate as measured by composite storage modulus at 0.1 rad/s shear rate. Dotted lines show fits according to Equation 8.*

The electrical conductivities of PC-CNT composites are shown in Figure 54 along with power law fits according to Equation 5 (fitting parameters presented in Table 10). Trends in

electrical percolation behavior largely match trends in the rheological percolation behavior of these composites. All electrical percolation thresholds are notably higher than the rheological percolation thresholds, in agreement with previous studies [144-146]. This ordering occurs because nanotubes can influence the rheological properties (complex viscosity, storage modulus, etc.) of a polymer composite without the nanotubes being in close proximity to one another because of an immobilized polymer layer near the surface of the nanotubes; however, the distance between

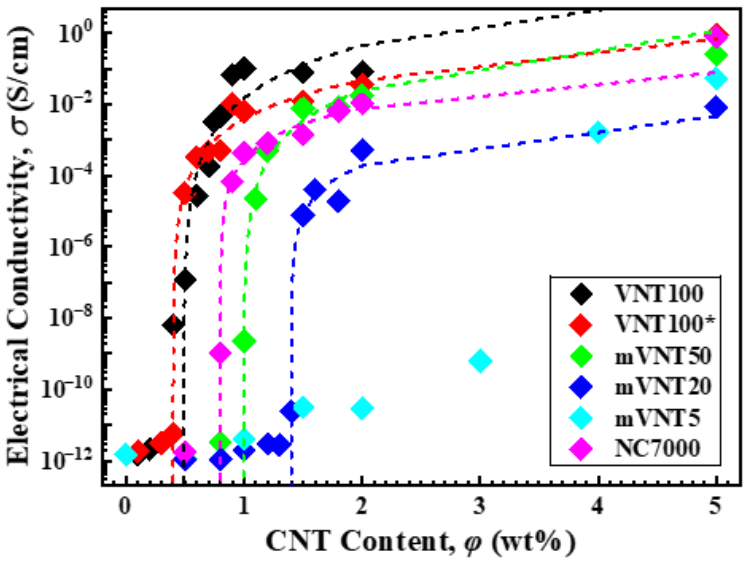

Figure 54: *Electrical percolation behavior of CNTs in polycarbonate as measured by electrical conductivity. Dotted lines show fits according to Equation 5.*

nanotubes must be smaller for efficient electron transfer by tunneling or direct electron transport as discussed previously [147-149]. The composites with the highest aspect ratio CNTs (VNT100 and VNT100*) show the lowest electrical percolation thresholds. While the fitted electrical percolation threshold for dCNT100 ($\varphi_{c,\sigma}$ = 0.40 wt%) is slightly lower than for CNT100 ($\varphi_{c,\sigma}$ = 0.49 wt%), the two data sets are quite similar. Ball milling the CNTs to 50 µm, 20 µm, and 5 µm

results in electrical percolation thresholds of 1 wt%, 1.4 wt%, and greater than 3 wt%, respectively, once again confirming percolation threshold dependence on aspect ratio. Additionally, the trend in maximum composite electrical conductivity at high CNT contents above the percolation threshold also follows that of Figure 19. Longer milling durations result in both lower CNT powder conductivities and lower PC-CNT composite conductivities.

Table 10: *Fitted rheological and electrical percolation parameters.*

CNT	Rheological			Electrical		
	$\varphi_{c,G'}$ (wt%)	G'_o (MPa)	$\beta_{G'}$	$\varphi_{c,\sigma}$ [wt%]	σ_o [S/cm]	β_σ
VNT100	0.18	4.6×10^{-3}	1.6	0.49	1.2×10^{-1}	3.2
VNT100*	0.20	1.7×10^{-3}	2.7	0.40	1.4×10^{-2}	2.5
mVNT50	0.23	4.3×10^{-4}	4.3	1.00	2.4×10^{-2}	2.8
mVNT20	0.62	1.1×10^{-3}	3.3	1.40	4.8×10^{-4}	1.8
mVNT5	> 3	-	-	> 2	-	-
NC7000	0.79	5.6×10^{-4}	0.8	0.80	5.5×10^{-3}	1.8

The trend of increasing percolation threshold with precursory CNT milling time has been reported previously for short carbon nanotubes in which ~50% length reduction resulted in a 31% increase in $\varphi_{c,\sigma}$ and ~67% length reduction resulted in a 49% increase in $\varphi_{c,\sigma}$ [150]. While the experimental percolation thresholds of the CNTs in this study are very good compared to low aspect ratio carbon fillers like carbon black [151, 152], we find significantly worse experimental percolation behavior compared to predicted values from Equation 4 as seen in Figure 55. This disagreement is further highlighted given the behavior of the PC composites filled with NC7000s,

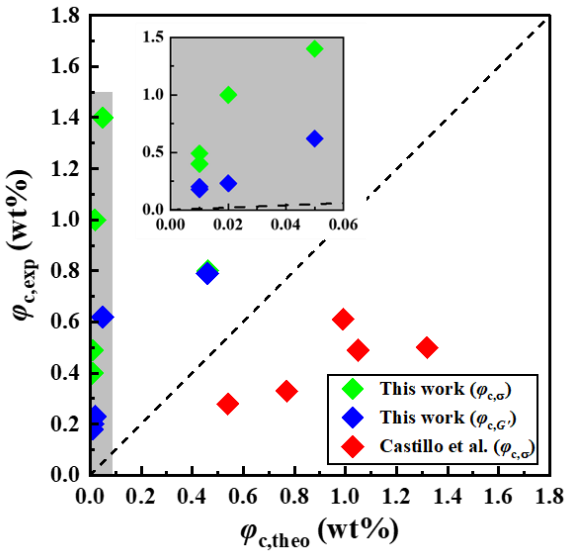

Figure 55: *Theoretical (see Equation 4) vs. experimental percolation thresholds from this work and previous work on various short ($\alpha \approx 100$) MWCNTs [60].*

which have an aspect ratio of about half that of mCNT5 but possess an electrical percolation threshold between that of VNT100 and mVNT50. While many have reported percolation thresholds near 1 wt%, nearly all studies consider CNTs with much lower aspect ratios (α << 1,000) than studied here [61, 153-155]. Additionally, some studies show experimental percolation thresholds lower than any found here ($\varphi_{c,\sigma} < 0.40$ wt%), albeit with different polymer matrices and dispersion methods [60, 156-158].

The large discrepancies between the theoretical and experimental percolation thresholds for the as-synthesized ultrahigh aspect ratio VNT100 nanotubes are likely due to the shear-resistant properties of the highly aligned and entangled bundles, as depicted in Figure 56. Shear forces imparted to nanofillers during melt mixing are typically high enough to disrupt the randomly ordered agglomerates typically seen in commercial CNTs, yet the original bundle morphology of

the CNTs synthesized on vermiculite is not greatly disrupted by the compounding process. The shear resistance of VNT100 bundles can be likened to interleaved pages of a book that are extremely difficult to separate due to extreme friction forces [159]. While individual level CNT dispersion of VNT100 is confirmed in SEM micrographs, the individually dispersed CNTs make up a small portion of the total CNT content in the composite, resulting in percolation thresholds

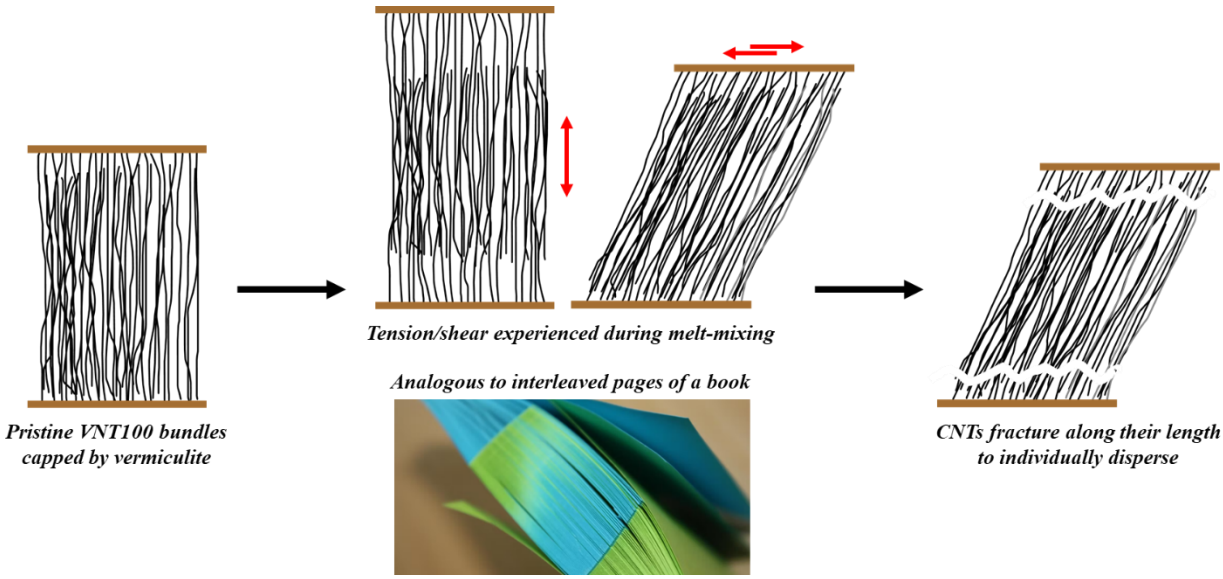

Figure 56: *Schematic illustration of dispersion mechanism of pristine VNT100 bundles.*

higher than anticipated. Upon ball milling, the bundle morphology appears to be completely disrupted based on small agglomerate sizes in the composites, initially suggesting the individual level CNT dispersion may be improved. However, Figure 50d confirms how small aggregates composed of shortened CNTs are surrounded by neat PC. In other words, the agglomerate size decreases, but the apparent percentage of CNTs participating in agglomeration increases, resulting in much higher CNT required for the formation of a percolated network. Thus, plain ball milling is detrimental to the dispersion and percolation behavior of polymer-CNT composites.

5.2.2 Surface chemistry effects

Storage modulus, loss modulus, and complex viscosity curves for PC composites filled mechanochemically functionalized CNTs are given in Figure 57. The complex viscosity of PC containing 1 wt% dfVNT5 is less than that of neat PC at high shear, which could be an indication of reduced PC molecular weight in the PC-dfVNT5 composite (to be discussed later in Section 5.3). However, increasing dfVNT5 content from 1 wt% to 2 wt% yields a notable transition from viscous to solid like behavior as indicated by elevated complex viscosity and storage modulus at low shear, indicating that the rheological percolation threshold for PC-dfVNT5 is below 2 wt%, which is a noted reduction compared to mVNT5 ($\varphi_{c,G'} > 2$ wt%) shown previously in Figure 53. Additionally, for PC-afVNT20, percolation appears to occur under 1 wt% as evidenced in Figure 57b. While the rheological percolation threshold of mVNT20 was shown to also be below 1 wt%, the storage modulus of PC-afVNT20 at this CNT content (~2 x 10^{-3} MPa) is significantly higher than that of PC-mVNT20 (~5 x 10^{-5} MPa), suggesting 1 wt% is further above the rheological percolation threshold of afVNT20 compared to mVNT20.

Bulk electrical conductivities of PC composites containing mechanochemically functionalized CNTs are presented in Figure 58 along with composites containing plain ball milled CNTs of the same aspect ratio. Electrical percolation thresholds of composites made with functionalized CNTs are lower than those made with unfunctionalized CNTs. The electrical percolation threshold of mVNT20 was previously shown to be 1.4 wt%. For afVNTs of the same aspect ratio, the electrical percolation threshold decreases to below 1 wt%. Similarly, for mVNT5, the electrical percolation threshold is above 3 wt%, and for dfVNTs of similar aspect ratio, the electrical percolation threshold decreases to below 2 wt%.

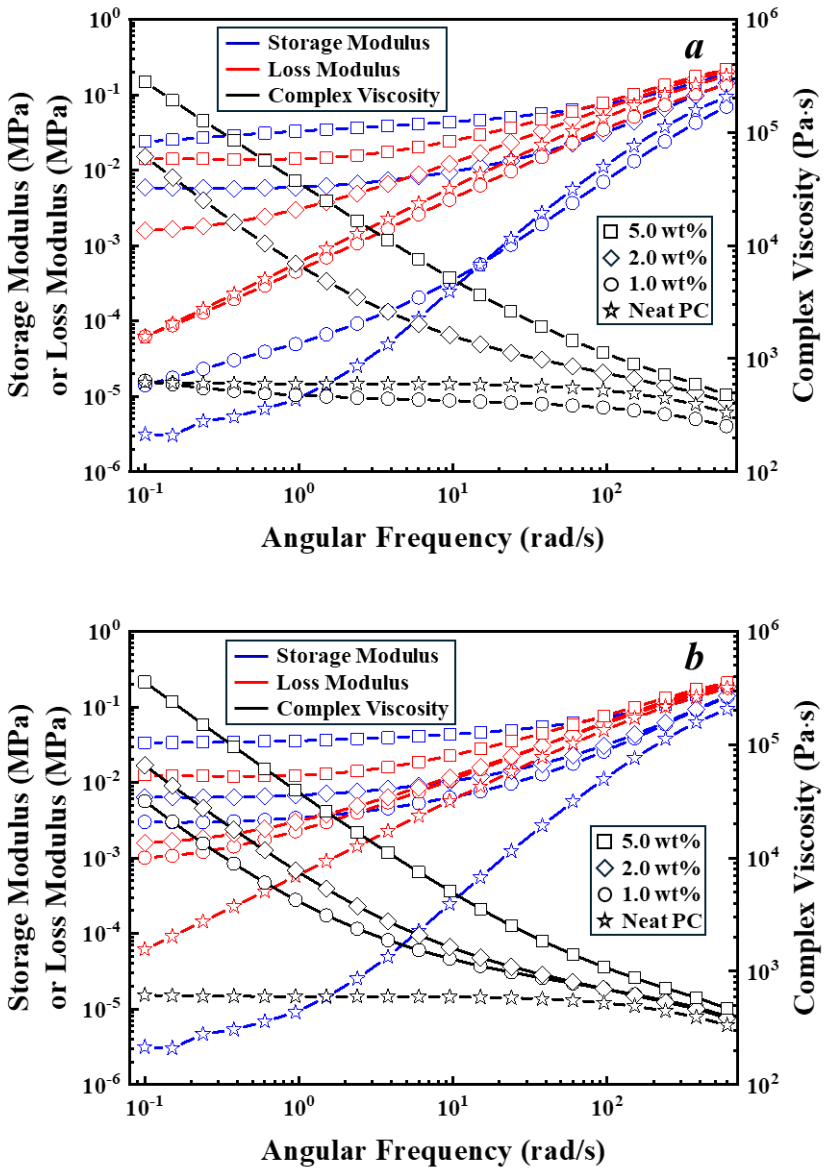

Figure 57: *Oscillation frequency sweep curves of (a) PC-dfVNT5 and (b) PC-afVNT20.*

The reduction in CNT content necessary for the formation of a percolated network is a positive sign that the dispersion of mechanochemically functionalized CNTs is improved compared to plain milled CNTs of the same aspect ratio. Most often for CNTs with covalently bonded oxygen-containing functional groups, the mechanism by which dispersion is improved in polymer composites is through improved polymer-CNT adhesion via hydrogen bonding. Hydroxyl

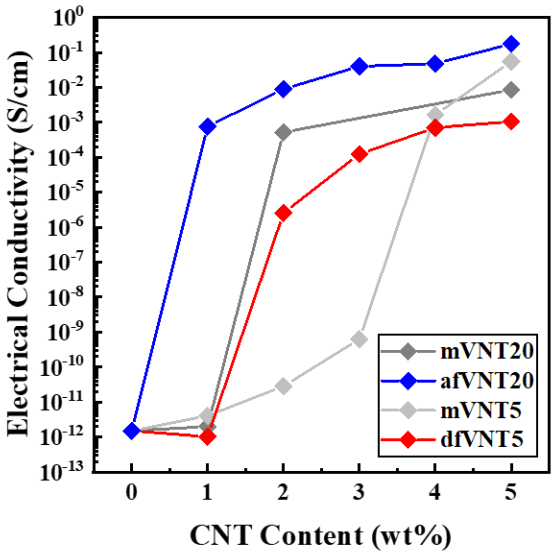

Figure 58: *Effect of mechanochemical functionalization on electrical percolation behavior of CNTs compared to plain milled CNTs of the same aspect ratio.*

(R-OH) and carboxyl (R-COOH) groups on CNT surfaces can participate in hydrogen bonding with oxygen atoms of the ether (C-O-C) and carbonyl (C=O) groups that compose the carbonate segments of the polycarbonate chain as depicted in Figure 59. While the strength of hydrogen bonding interactions is weak compared to the covalent bonds that compose polymer chains and CNT backbones, their prevalence among the polymer-CNT system can yield significant improvements in dispersion and percolation as seen here. It should be noted that these enhanced polymer-CNT interactions would not be expected for polymers that do not contain strong hydrogen bonding acceptors, such as polyethylene and polypropylene.

5.3 Thermal properties

Table 11 presents relevant thermal properties measured by DSC and TGA, and Figure 60 displays the TGA profiles of PC-CNT composites. The glass transition temperature, T_g, of neat PC

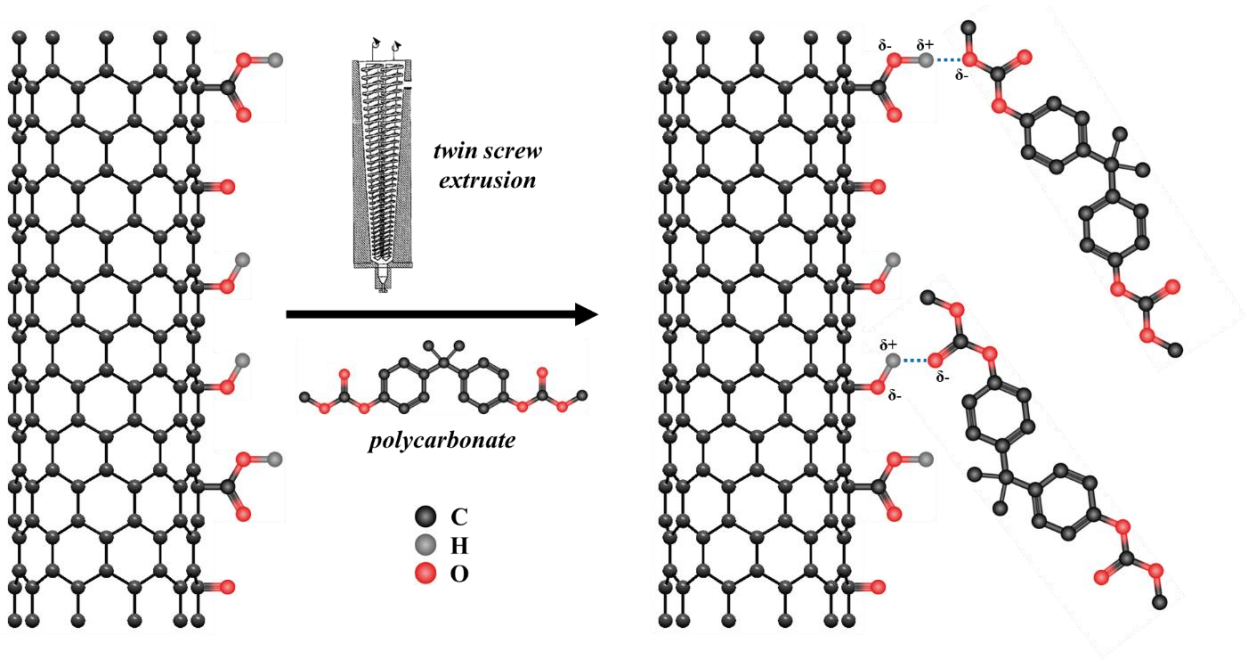

Figure 59: *Hydrogen bonding between CNT surface groups and polycarbonate chains.*

is 143.3 °C ± 0.2 °C and does not change after the extrusion processing step with no nanotube incorporation. A constant glass transition temperature in this case would typically suggest that the molecular weight of polycarbonate is constant. However, the degradation temperature, T_d, notably decreases from 505.8 °C to 494.5 °C (± 1.1 °C assumed for all samples) upon processing, most likely indicating molecular weight reduction. The degradation temperature decreases from 494.5 °C for processed PC to 477.2 °C upon addition of 5 wt% VNT100*, further indicating a higher extent of polymer chain degradation due to viscosity increase. However, for composites filled with milled CNTs, T_d increases moderately but consistently as nanotube length is reduced from milling. For PC containing 5 wt% mVNT5, the degradation temperature nearly approaches that of the processed PC, mimicking the similarity in melt viscosity reported previously. These results demonstrate that ball milling does in fact improve the processability of PC-CNT composites containing high aspect ratio CNTs by reducing melt viscosity and polymer degradation. However,

Table 11: *Thermal properties of PC-CNT (5.0 wt%) composites measured by DSC/TGA.*

Composite	T_d (°C)	T_g (°C)	ΔC_p (J/g·°C)	*RAF* (%)
†PC (neat)	505.8	143.3	0.261	-
PC (processed)	494.5	143.4	0.261	-
PC-VNT100*	477.2	143.5	0.229	7.3
PC-mVNT50	479.4	143.3	0.239	3.6
PC-mVNT20	482.9	143.1	0.235	5.1
PC-mVNT5	485.1	143.5	0.239	3.6
PC-dfVNT5	474.9	141.8	0.224	9.1
PC-afVNT20	441.4	142.6	0.230	6.9
PC-NC7000	489.2	143.3	0.220	10.9

†Errors in T_d, T_g, and ΔC_p as measured from duplicate neat PC trials are ± 1.1 °C, ± 0.2 °C, and ± 0.004 J/g·°C, respectively. *RAF* error is ± 1.6 wt% as a result of compounded ΔC_p error.

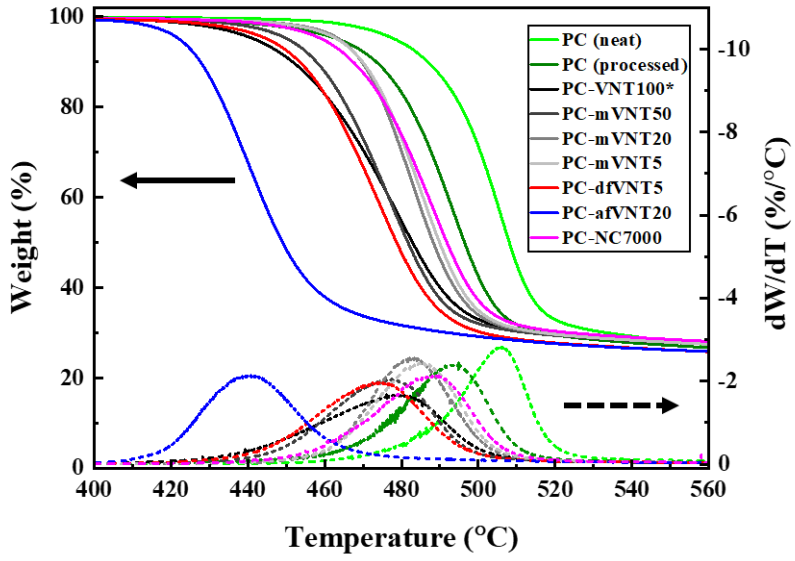

Figure 60: *TGA curves of PC-CNT composites.*

composites made with mechanochemically functionalized CNTs show notable drops in T_d (474.9 °C for dfVNT5 and 441.4 °C for afVNT20) and T_g (141.8 °C for dfVNT5 and 142.6 °C for afVNT20), indicating a significant increase in polymer degradation compared to plain milled CNTs. Although a nitrogen blanket is applied in the micro compounder to reduce oxidation, physiosorbed species on the surfaces of CNTs may desorb at the high compounding temperature and oxidize the polymer. Covalently bonded oxygen-containing functional groups may also decompose during processing, leading to similar issues. While the reduced thermal stability of PC filled with mechanochemically functionalized CNTs is undesired, the degradation temperature for these composites is still comparable to or higher than many engineering plastics like acrylonitrile butadiene styrene (ABS) [160], polymethylmethacrylate (PMMA) [161], and polyamide 6 (PA6) [162].

The change in heat capacity at the glass transition of neat PC is 0.261 J/g·°C ± 0.004 J/g·°C and does not change upon processing. While the addition of CNTs results in a negligible change in the glass transition, there are clear reductions in ΔC_p that are consistent with previous work with polymer-CNT composites [60, 65, 163, 164]. Upon addition of 5 wt % VNT100*, ΔC_p decreases substantially to 0.229 J/g·°C (normalized for PC fraction only). Similarly, milled and mechanochemically functionalized CNTs show a notable decrease in ΔC_p relative to neat PC. However, composites with plain milled CNTs (mVNT50, mVNT20, and mVNT5) show a slightly elevated ΔC_p relative to PC-VNT100* while composites with mechanochemically functionalized CNTs (dfVNT5 and afVNT20) have a noticeably lower ΔC_p. For polymer composites, ΔC_p can be used as a measure of polymer-filler interactions. While the rigid amorphous fraction, *RAF*, of polymers is traditionally discussed in relation to the immobilization of polymer chains near crystalline regions of semicrystalline polymers [165], *RAF* has also been used to describe the

immobilization of polymer chains due to interactions with filler particles by the following expression

$$RAF = 1 - \varphi - \frac{\Delta C_p}{\Delta C_{p,pure}} \quad (27)$$

where ΔC_p is for the composite and $\Delta C_{p,pure}$ is for the neat polymer [166]. Effectively, *RAF* increases as the polymer-nanotube contact area increases. Thus, when comparing different composites with equivalent CNT loadings, a higher *RAF* indicates a higher degree of CNT dispersion. At 5 wt% VNT100, the *RAF* of PC is 7.3%. For plain ball milled CNTs, *RAF* decreases to between 3.6% and 5.1%. However, both dry and aqueous mechanochemically functionalized CNTs show higher *RAF* values compared to the plain milled nanotubes at 9.1% and 6.9%, respectively. This corroborates the improved percolation behavior and improved individual-level CNT dispersion seen in SEM micrographs, again due to enhanced polymer-nanotube interactions from surface functionalization.

Interestingly, the *RAF* of PC with 5 wt% NC7000 is notably higher than for milled or functionalized CNTs. This could be explained by NC7000 having a higher specific surface area than VNT100. On a per weight basis, the total contact area between carbon nanotubes and the polymer depends on CNT density and CNT surface area per unit volume. The density of an individual nanotube calculated based on the number of concentric cylinders and overall diameters measured from TEM gives an equivalent value of 1.95 g/cm^3 for both VNT100 and NC7000 within experimental error [22]. Since the surface area per unit length for an individual nanotube is proportional to the circumference (i.e., diameter), VNT100 (~47 nm^2/nm) has more surface area per unit length than NC7000 (~35 nm^2/nm). However, dividing by CNT cross sectional area yields the surface area per unit volume, for which that of VNT100 (0.27 nm^2/nm^3) is less than NC7000 (0.36 nm^2/nm^3). Thus, because the densities are the same, the specific surface area per unit weight

of NC7000 (~1.9 x 10^6 cm^2/g) is greater than that of VNT100 (~1.4 x 10^6 cm^2/g), inherently leading to a larger polymer-nanotube interfacial area for PC-NC7000 assuming similar degrees of dispersion. Further, while NC7000 nanotubes are much lower in aspect ratio and require higher contents to achieve percolation compared to VNT100, it is likely that these nanotubes disperse better due to the initial randomly agglomerated bulk morphology. Previous studies have shown very good dispersion of NC7000 in polymers by melt-mixing with experimental percolation thresholds under 0.5 wt%, outperforming theoretical predictions of 0.66 wt% according to Equation 4 [167, 168].

5.4 Mechanical properties

Figure 61 presents the elastic modulus, tensile strength, and failure strain of PC composites containing 1 wt% CNTs. The elastic modulus of neat PC is 1.7 GPa and does not change within statistical significance with the addition of CNTs. The failure strain of PC decreases substantially from 53% to 14% upon addition of pristine CNTs with no statistically significant differences between different CNTs. While there is some change in tensile strength, t-tests show that the only statistically significant result here is the difference in tensile strength between PC-dfVNT5 and PC-afVNT20. The lack of significant changes in mechanical properties for CNT addition to PC is not uncommon in the literature [65, 169, 170], although some have shown improvements in strength and stiffness [64, 171, 172]. Mechanical reinforcement of thermoplastics with CNTs relies heavily on dispersion, aspect ratio, and polymer-CNT adhesion. While VNT100 is shown to have very high aspect ratio, agglomeration and lack of adhesion between the nanotubes and polymer likely offset any positive mechanical reinforcement effects. Additionally, while mechanochemical functionalization improves dispersion, the reduced aspect ratio and PC degradation from

compounding may contribute to offsetting any positive mechanical reinforcement effects. The notable improvement in strength for PC-afVNT20 compared to PC-dfVNT5 could be explained by afVNT20 nanotubes possessing a larger aspect ratio with similar degree of dispersion.

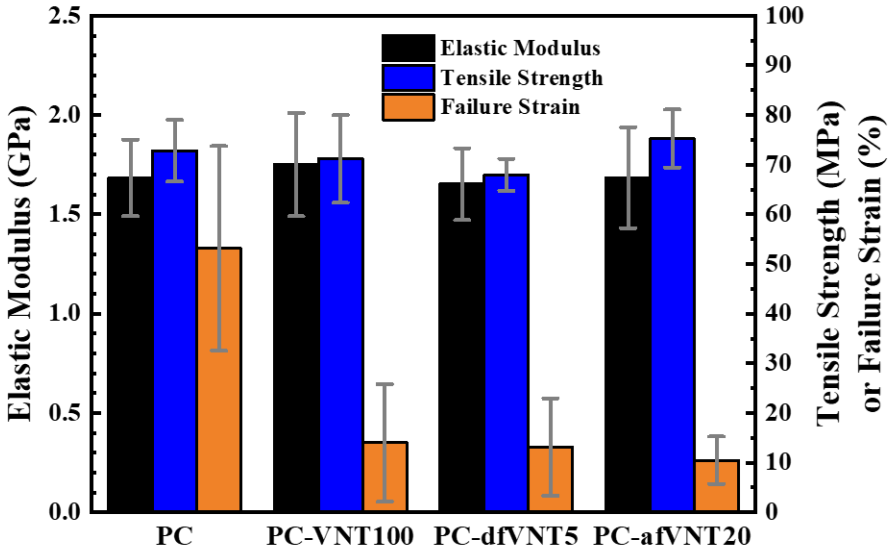

Figure 61: *Tensile mechanical properties of PC composites containing 1 wt% CNTs.*

Chapter 6: Aspect ratio and surface chemistry effects on tire tread rubber-nanotube composites

6.1 Design considerations

Tire tread design typically relies on three important performance considerations – durability, grip, and rolling resistance – that are often dubbed the "magic triangle" of tire design [173]. Tire durability is important for extending the lifetime of a tire. Abrasion resistance is the primary key performance indicator of tire durability in this context, and the tensile mechanical properties (tensile strength, stiffness, etc.) are also important. Grip is another important tire characteristic to consider for driving in wet and icy conditions. The loss tangent, *tanδ*, which is the ratio of the loss modulus, *G"*, to storage modulus, *G'*, is often used as a measure of tire rubber traction characteristics. A high *tanδ* at ~0 °C is an indication of good wet traction, and a high *tanδ* at -20 °C is an indication of good ice traction. A high *tanδ* indicates a rubber compound with more viscous-like behavior, allowing for enhanced rubber flexibility and increased contact area with road surfaces. The final vertex of the magic triangle, rolling resistance, is important for understanding how the tire design contributes to the fuel economy of the vehicle. A high rolling resistance typically is related to high hysteresis, i.e., energy loss, due to tire rubber deformation. Thus, rolling resistance is also often characterized by tracking the loss tangent, as measured by dynamic mechanical analysis at higher temperatures compared to the traction regime. A low *tanδ* at 60 °C (sometimes a range of 50-70 °C is used) is an indication of low rolling resistance due to the rubber presenting more solid-like characteristics and experiencing less deformation and energy loss upon rolling, which would subsequently lead to reduced fuel consumption and improved gas mileage. A 10% reduction rolling resistance generally results in a 1-2% improvement in fuel economy [174].

Carbon nanotubes present an interesting case for partial of full replacement of carbon black in tire tread rubber. Carbon black (CB) is a roughly spherical, usually micron-sized particle composed of paracrystalline carbon that has traditionally been used as a high content filler for improving tire rubber mechanical properties and abrasion resistance. In typical tread compounds, the CB content is usually between 40 and 80 phr, which ends up being well over 25 wt% of the tread rubber. As previously discussed with high aspect ratio fillers, the required filler content for adequate reinforcement may be less than for lower aspect ratio fillers. While full replacement of CB with CNTs may not be viable, partial replacement of CB with CNTs may allow for the reduction in total filler amount, which would reduce tire density and subsequently tire weight. Additionally, reduced filler content has often shown to lead to reduced rolling resistance. The slight lightweighting effect with reduced rolling resistance could yield a small but notable improvement in vehicle fuel economy that could have major reductions on absolute gasoline consumption given the enormous scale of vehicle miles driven. The goal of the following study is not to develop a new tire formulation to replace carbon black in tire tread rubber, but to present an initial investigation into the viability of ultrahigh aspect ratio CNTs (VNT100) as partial or full replacements for CB in tire tread rubber.

6.2 Compounding

Compounding time optimization for filler dispersion was based on drive torque (i.e., compound viscosity) during compounding [175, 176]. Figure 62 presents a typical mixing curve (blade torque vs. mixing time) for the 72 phr CB control SBR-BR compound. The rubber mastication time (step 1) was chosen to be 1 min as the torque, i.e., viscosity, was found to reach a near constant level. Addition of fillers, processing oil, activators, antioxidant, and antiozonant

(step 2) took 1 min, then the mixer was closed for compounding (step 3). The blade torque increased to a maximum torque, τ_{max}, within 15 sec, and after 12 min of compounding the torque was found to reach a near constant level τ_{const}. The optimal compounding time was chosen such that the torque reduced by 90% (τ_{90}) from τ_{max} to τ_{const}. For the control compound, the time to reach τ_{90} was found to be 8 min (10 min total including mastication and ingredient addition). Thus, sulfur and accelerator were chosen to be added to the mixer after 6 min of compounding time (step 4) and allowed to mix for 2 min before ejecting the rubber compound (step 5). While variances in optimal compounding time could be expected for different filler types and contents, the mixing time was kept constant for all compounds.

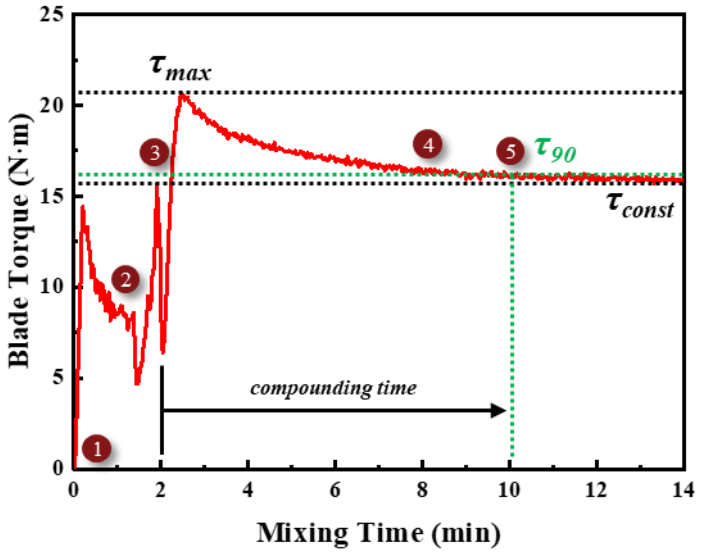

Figure 62: *Rubber compounding curves.*

While thermoplastics usually require high processing temperatures that can severely degrade the polymer if the viscosity is too high, typical rubber processing occurs at much lower temperatures (60 °C in this case), reducing the probability of rubber degradation. However, the

effects of CNT incorporation on raw rubber compound viscosity are still of high interest given the extreme aspect ratio differences between carbon nanotubes and carbon black. Figure 63 presents the maximum and final blade torques as well as internal mixer temperature rise during compounding for SBR-BR compounds. The maximum and final torque during compounding for the control 72 phr CB compound was 20.7 N·m, and 16.2 N·m, respectively. Upon duplicate mixing trials of the control compound, it was found that the error in maximum and final blade torque was under 2%, and it was assumed that this deviation did not change greatly for other compounds containing different filler contents and types. Decreasing the CB content to 54 phr and 36 phr decreases the maximum torque by 8.7% (18.9 N·m) and 14.5% (17.7 N·m), respectively, as well as the final torque by 1.9% (15.9 N·m) and 7.4% (15.0 N·m), respectively. Because the batch size remained constant, this drop in torque is directly attributed to the reduced filler content. For 54 phr filler content, the partial replacement of 6 phr carbon black with carbon nanotubes notably increases the maximum torque by 13.2% (21.1 N·m) for NC7000 and 29.1% (24.4 N·m) for VNT100. Similarly, the final torque is increased by 11.9% (17.8 N·m) for NC7000 and 18.9% (18.9 N·m) for VNT100. Further, full replacement of 72 phr CB with just 12 phr carbon nanotubes significantly increases the viscosity of SBR-BR compounds. For 12 phr NC7000, the maximum and final torques are 26.0 N·m and 19.4 N·m, respectively, and for 12 phr VNT100, the maximum and final torques are 29.4 N·m and 22.3 N·m, respectively. The significant increases in compound viscosity upon partial and full replacement of carbon black with carbon nanotubes is due to the extreme aspect ratio differences as discussed previously. Further, the ultrahigh aspect ratio VNT100 nanotubes show higher compound viscosities compared to the lower aspect ratio NC7000, further agreeing with expectations from suspension viscosity dependence on filler aspect ratio.

The temperature rise of an internal mixer is an important parameter to mitigate in industrial rubber compounding due to the possibility of scorching. Scorching occurs when rubber vulcanizes prematurely during compounding, causing it to harden and become unable to be processed further. The internal mixer temperature rise for all SBR-BR compounds containing only carbon black filler was approximately 6-7 °C and did not vary greatly among different CB contents. However, all compounds containing carbon nanotubes displayed elevated temperature rises during compounding due to higher contributions from viscous heating. SBR-BR compounding with 48CB:6CNT filler systems resulted in the highest temperature rise despite containing a lower total filler content than the control 72 phr CB compound. While the maximum and final torques for SBR-BR compounds containing 12 phr CNT are notably higher compared to all other compounds, the temperature rise is lower than for the 48CB:6CNT systems, likely due to the significantly lower total filler content. In both cases (48CB:6CNT and 12CNT), the temperature rise for higher aspect

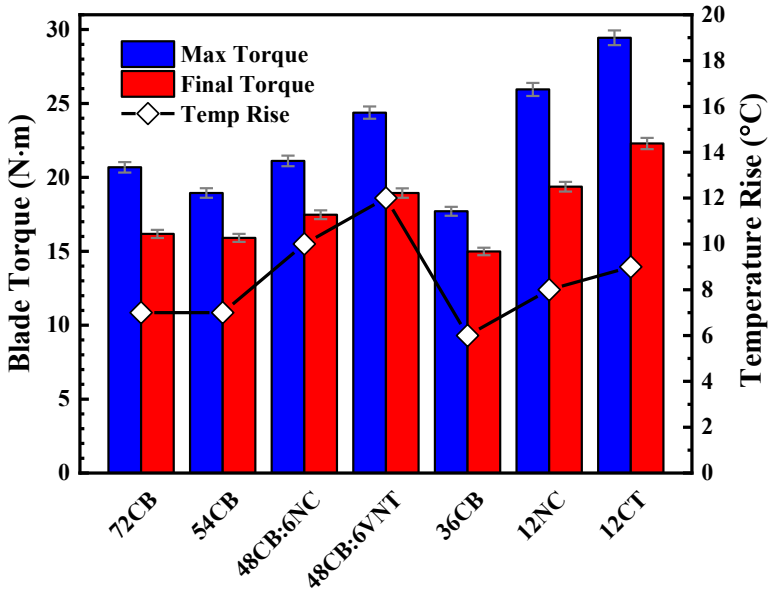

Figure 63: *Maximum and final blade torque measurements during compounding for SBR-BR compounds.*

ratio VNT100 was greater than that for the lower aspect ratio NC7000. However, given that vulcanization of rubber compounds typically occurs near 160 °C, a maximum temperature rise of 12 °C found here would likely not have a great effect. Additionally, because the sulfur is mixed for only 2 min at the end of the compounding process, the probability of scorching withing the conditions studied is minimal.

6.3 Curing kinetics

The vulcanization behavior of unfilled SBR-BR and the control SBR-BR compound containing 72 phr carbon filler at 160 °C is presented in Figure 64. Rheometry curves show increasing torque over time, indicative of the formation of a crosslinked network due to rubber curing. The maximum torque reached after curing for SBR-BR filled with 72 phr CB is more than three times that of the unfilled compound, suggesting the addition of carbon black significantly increases the viscosity and stiffness of SBR-BR. This is expected as carbon black's role in rubber

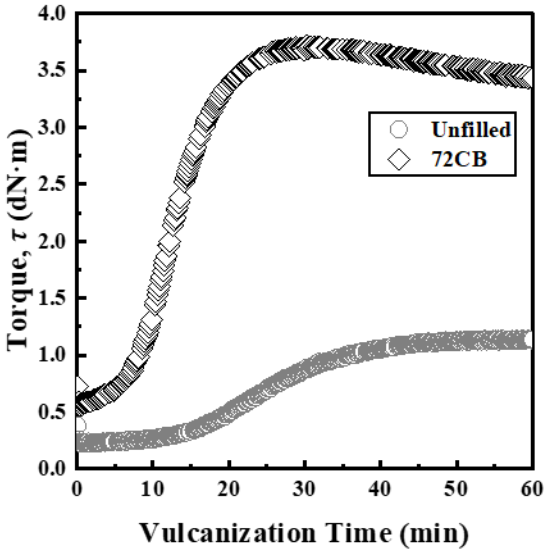

Figure 64: *SBR-BR torque curves during isothermal vulcanization at 160 °C.*

is primarily as mechanical reinforcement. Additionally, the addition of 72 phr CB appears to increase the rate of curing as full cure is reached under 30 min compared to the unfilled compound that requires seemingly up to 60 min to reach maximum torque.

Torque measurements during vulcanization can be normalized to yield a dimensionless value that represents the degree of cure. Thus, the degree of vulcanization, θ_v, can be calculated by the following

$$\theta_v = \frac{\tau - \tau_{min}}{\tau_{max} - \tau_{min}} \tag{28}$$

where τ is the measured torque and τ_{max} and τ_{min} are the maximum and minimum torque during vulcanization. Additionally, the kinetics of rubber vulcanization have been shown to follow the Kamal-Sourer model of the following form

$$\theta_v = \frac{k_v(t - t_0)^{n_v}}{1 + k_v(t - t_0)^{n_v}} \tag{29}$$

where k_v is the rate constant, n_v is the power law exponent, t is the time during vulcanization, and t_0 is the induction time [177, 178]. Figure 65 presents degree of vulcanization curves for SBR-BR compounds along with lines representing the fit to the Kamal-Sourer model, and Figure 66 presents the corresponding vulcanization rate constant dependence on filler content and type. The relationship between CB content and vulcanization rate constant more clearly demonstrates how the rate of curing is increased upon addition of CB to SBR-BR. This could be attributed to the increased bulk thermal conductivity, increasing the rate at which heat accumulates in the compound during vulcanization. Crystalline regions of carbon black can enhance phonon conduction as has been shown previously for rubber-CB compounds [179]. Additionally, the addition of fillers to rubber results in a bound rubber fraction at the surface of filler particles (similar to *RAF* discussed previously), reducing chain mobility and energy (i.e., heat) dissipation.

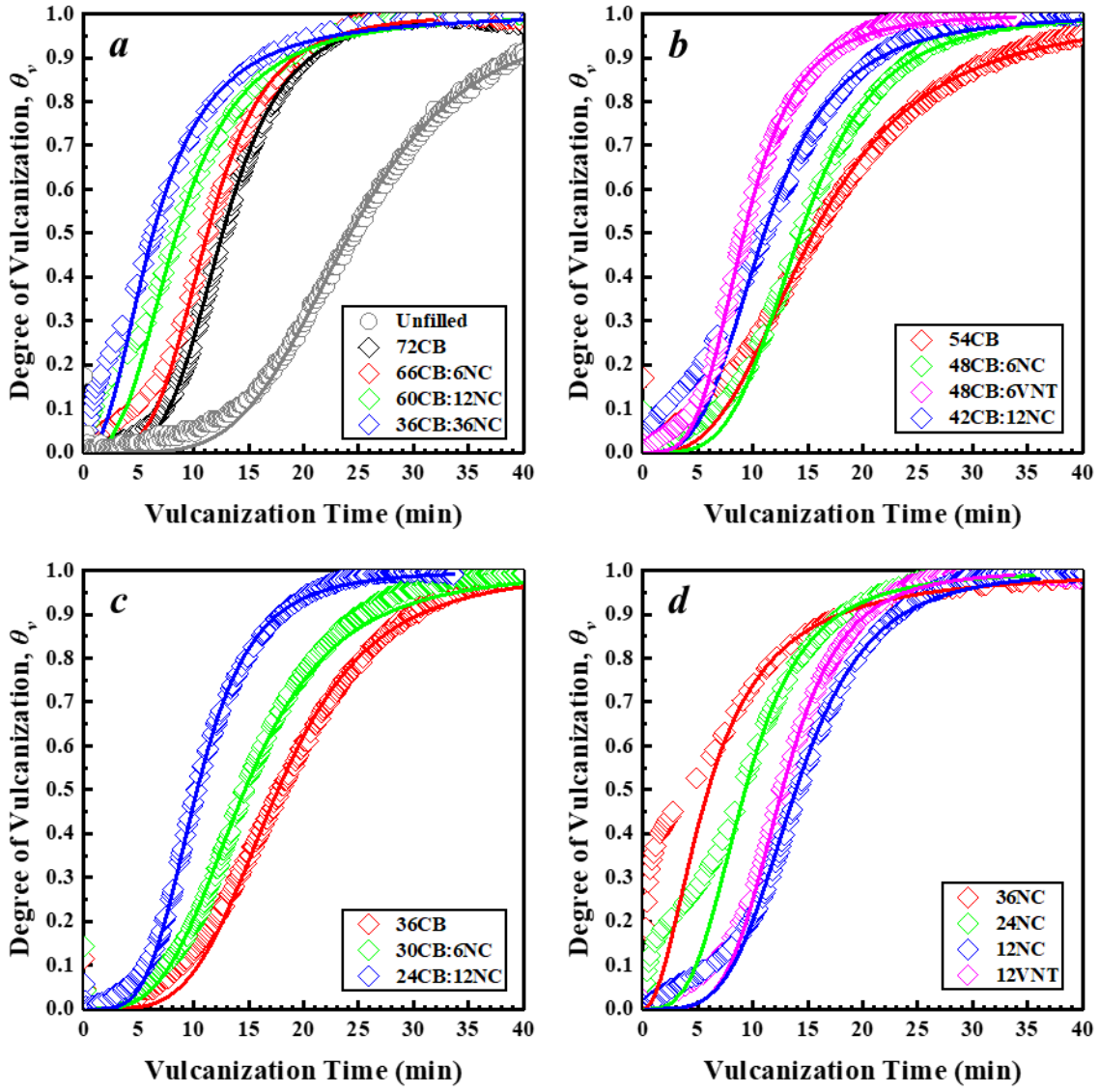

Figure 65: *Degree of vulcanization curves for SBR-BR composites containing (a) 72 phr filler, (b) 52 phr filler, (c) 36 phr filler, and (d) CNT filler only.*

Full replacement of CB with carbon nanotubes results in faster rates of cure for equivalent loadings as evidenced by much higher vulcanization rate constants in Figure 66. This same effect is seen for compounds with CB partially replaced by NC7000. Faster rates can generally be attributed to the higher thermal conductivity of CNTs compared to carbon black and the higher

filler surface area. Additionally, higher aspect ratio CNTs appear to result in faster curing rates compared to lower aspect ratio CNTs as seen for SBR-BR compounds containing VNT100 compared to those containing NC7000. Interestingly, for SBR-BR compounds with increasing CNT content, there is a region of torque elevation during the first ~5 min of vulcanization; this effect is more pronounced in Figures 65a and 65d for the highest CNT content samples. This phenomenon has been reported previous by Garcia et al. and was attributed to the presence of a percolated CNT network that alters the bulk rheological behavior of the compound [178]. Additionally, this elevated initial torque could be evidence of scorching due to higher viscous heating during compounding for CNT filled compounds.

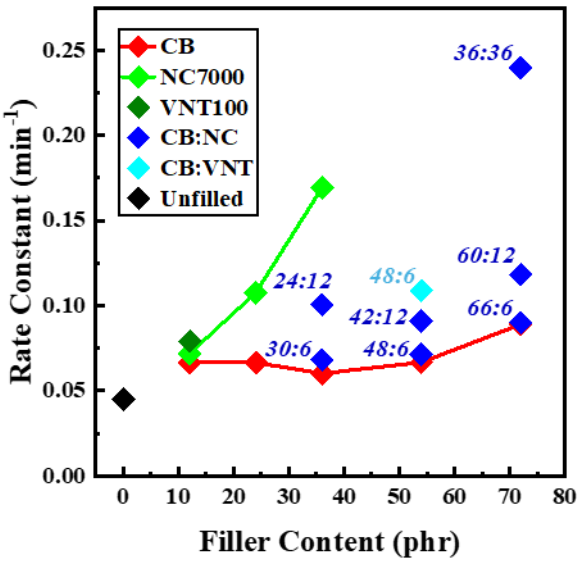

Figure 66: *Vulcanization rate constant dependence on filler type and content.*

6.4 Mechanical properties

Tensile mechanical properties of SBR-BR compounds are presented in Figure 67. The tensile strength of unfilled SBR-BR is 1.2 ± 0.2 MPa and the Young's modulus is 0.7 ± 0.1 MPa.

Upon addition of 72 phr CB for the control compound, the tensile strength and Young's modulus increase to 6.6 ± 0.5 MPa and 2.9 ± 0.1 MPa, respectively. Partial replacement of 72 phr CB with 6 phr NC7000 results in an increase in tensile strength to 8.3 ± 0.9 MPa with a simultaneous increase in failure strain, suggesting there may be some synergistic effects of dual CB:CNT filler systems on the mechanical reinforcement of SBR-BR rubber. However, further increasing the replaced CB content to 12 phr NC and 36 NC results in drops in tensile strength to 6.8 ± 0.7 MPa

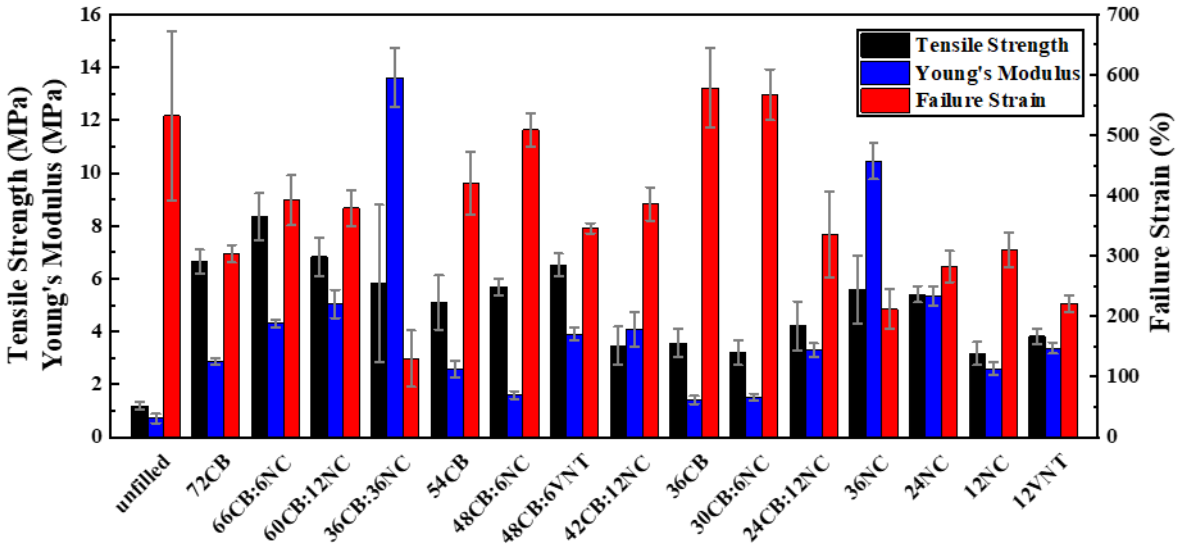

Figure 67: *Tensile mechanical properties of SBR-BR composites.*

and 5.8 ± 2.9 MPa, respectively, due to significantly reduced ductility. Interestingly, partial replacement of 6 phr CB with CNTs in a 54 total phr filler compound yields similar mechanical properties to the control 72 phr CB compound; the tensile strength of compounds with 48CB:6NC and 48 are 5.7 ± 0.3 MPa and 6.5 ± 0.4 MPa, respectively. In other words, the total filler content can be reduced by 25% and partially replaced with a small amount of CNTs to yield similar mechanical properties to the control. It is interesting to note also that higher CNT aspect ratios

appear to increase the degree of mechanical reinforcement. This effect is seen comparing the 48CB:6CNT filler systems as well as comparing 12 phr NC700 (tensile strength of 3.2 ± 0.4 MPa) with 12 phr VNT100 (tensile strength of 3.8 ± 0.3 MPa).

The positive effects of small CNT content incorporation on the mechanical properties of rubber are well documented, and the general trends of strength and modulus with respect to filler content and aspect ratio agree with expected trends [26, 53, 180]. However, the extent to which the mechanical properties are enhanced for the ultrahigh aspect ratio VNT100 compared to the lower aspect ratio NC7000 is less than what would be predicted from theory, which is very likely due to non-ideal dispersion of VNT100 nanotubes as shown previously in polycarbonate. Of particular interest was the simultaneous enhancement in stiffness and failure strain for the 66CB:6NC filler system. Typically, for higher stiffness a lower failure strain would be expected. However, for low CNT incorporations to a high CB content compound, the CNTs can possibly act as bridges connecting the primary reinforcing CB particles. The presence of CNT bridges in regions not containing CB could transfer the stress back to the primary reinforcing particles, allowing for a higher strain before failure. However, increasing CNT content beyond 6 phr or reducing total filler content below 72 phr appears to deviate from this phenomenon.

The tensile strengths of all rubber compounds found here are lower than typically reported tensile strength values (10-20 MPa) for modern tire tread rubber. This discrepancy could be attributed to a few factors. The control tire tread formulation chosen for this study, which was used as a CB-containing control passenger tire tread compound by BF Goodrich in a 1985 patent [116], may be outdated compared to modern tire rubber technology with higher strengths [181]. Additionally, the processing oil content (37 phr) is quite high compared to that of many other comparable tire tread compounds recently patented/studied using under 20 phr processing aid [182,

183]. High oil contents would certainly reduce stiffness and would likely reduce strength depending on the filler content. While further study would be warranted to ensure carbon nanotubes can be added to rubber to yield composite mechanical properties within the necessary standards for tire tread rubber, the relative effects of partial or full replacement of carbon black with carbon nanotubes on the mechanical properties found in this work would also be expected for other rubber compounds assuming all other components are kept constant.

The mass loss of abrasion tested SBR-BR compounds is presented in Figure 68. Increasing carbon black content generally leads to an increased abrasion resistance (comparing 36CB to 54CB to 72CB). Partial replacement of CB with NC7000 improves abrasion resistance at both 72 and 54 total filler phr, reducing mass loss by as much as 50% (compare 95 ± 17 mg mass loss for 42CB:12NC to 198 ± 44 mg mass loss for 54CB). This effect is more pronounced comparing 36 phr CB to 36 phr NC7000, exhibiting a 71% decrease in abrasion mass loss from 233 ± 42 mg to

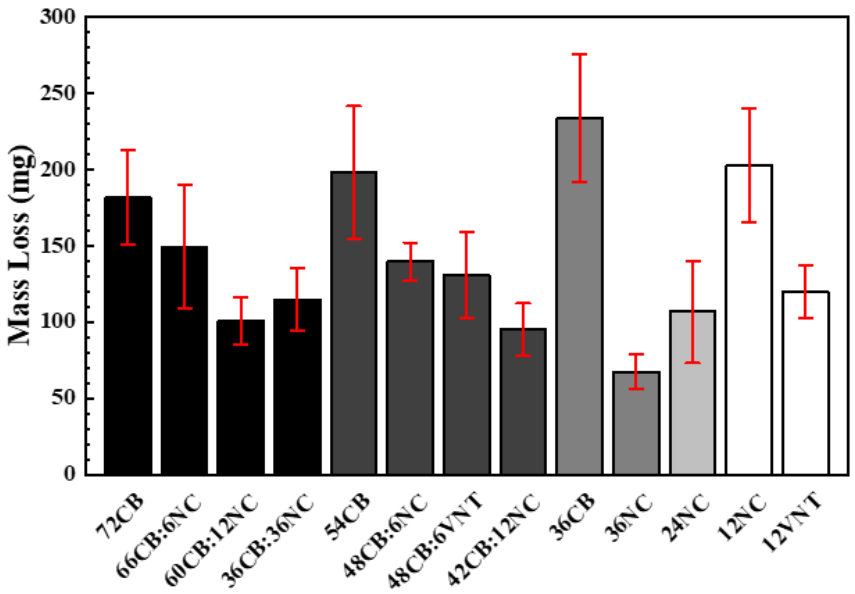

Figure 68: *Abrasion resistance of SBR-BR compounds measured by mass loss from abrasion testing.*

67 ± 12 mg. Additionally, higher aspect ratio VNT100 nanotubes result in improved abrasion resistance compared to lower aspect ratio NC7000 as evidenced by the reduction in mass loss of 48CB:6VNT (131 ± 28 mg) compared to 48CB:6NC (140 ± 13 mg) as well as 12VNT (120 ± 17 mg) compared to 12NC (203 ± 38 mg). The wear properties of these SBR-BR compounds also largely follow the trends of mechanical reinforcement presented previously, suggesting the reinforcing mechanism under tensile load and shear abrasion is related. This parallel relationship between CNT aspect ratio and rubber compound tensile mechanical and abrasion properties has been shown previously [183].

6.5 Dynamic mechanical properties

Storage modulus, loss modulus, and loss tangent curves of SBR-BR composites generated from dynamic mechanical analysis in oscillatory linear tension are presented in Figure 69. The loss tangent of all SBR-BR compounds reaches a maximum around -55 °C, indicative of the glass transition of the rubber. The amount of filler appears to have a negligible effect on the glass transition temperature. However, increasing filler content appears to reduce *tanδ* at the glass transition. Additionally, increasing CNT content at equivalent total filler loadings similarly reduces *tanδ* at the glass transition, both of which are due to the increased stiffness due to higher filler content and CNT incorporation.

As discussed previously, the value of *tanδ* at different temperatures can help predict the rolling resistance and traction characteristics for tire tread rubber. While direct translation of *tanδ* to other physical property values of tire rubber, such as the rolling resistance coefficient, is not straightforward, the relative changes in *tanδ* for different filler contents and types can be used to infer whether rolling resistance and wet/ice traction will be improved or worsened. Loss tangent

values of SBR-BR compounds at 60 °C, 0 °C, and -20 °C associated with rolling resistance, wet traction, and ice traction, respectively, are listed in Table 12. The control 72 phr CB compound has $tan\delta_{0°C}$ and $tan\delta_{-20°C}$ values of 0.11 and 0.13, respectively. Decreasing total CB content to 54 phr reduces both values to 0.07 and 0.10, respectively, suggesting higher filler contents are better for improving wet and ice traction. Partial replacement of CB with small amounts of CNT at both 72 and 54 total filler phr generally results in higher *tanδ* values in the traction temperature regime, suggesting CNT incorporation into tire tread rubber can notably improve wet and ice traction.

The rolling resistance characteristics are represented by the *tanδ* value at 60 °C, which is 0.05 for the control 72 phr CB compound. The 52 phr CB compound has a lower *tanδ* of 0.02, suggesting higher filler contents result in higher rolling resistances which has been proven previously. Partial replacement of CB with CNTs results in significant increases in *tanδ*, indicating the rolling resistance of these compounds would be much higher compared to SBR-BR containing only CB. While increases in rolling resistance have been shown previously for CNT incorporation for tire tread rubbers [184], the extent to which the rolling resistance increases could be an indication of poor dispersion. Typically for higher filler surface area, a lower *tanδ* would be expected. This is due to reduced chain mobility as discussed previously with *RAF* in the context of PC-CNT composites, thus promoting energy storage rather than energy dissipation. However, in this case we find that the loss modulus, i.e., viscous behavior, of SBR-BR compounds increases substantially upon CNT incorporation, increasing the dissipation factor and thus increasing rolling resistance.

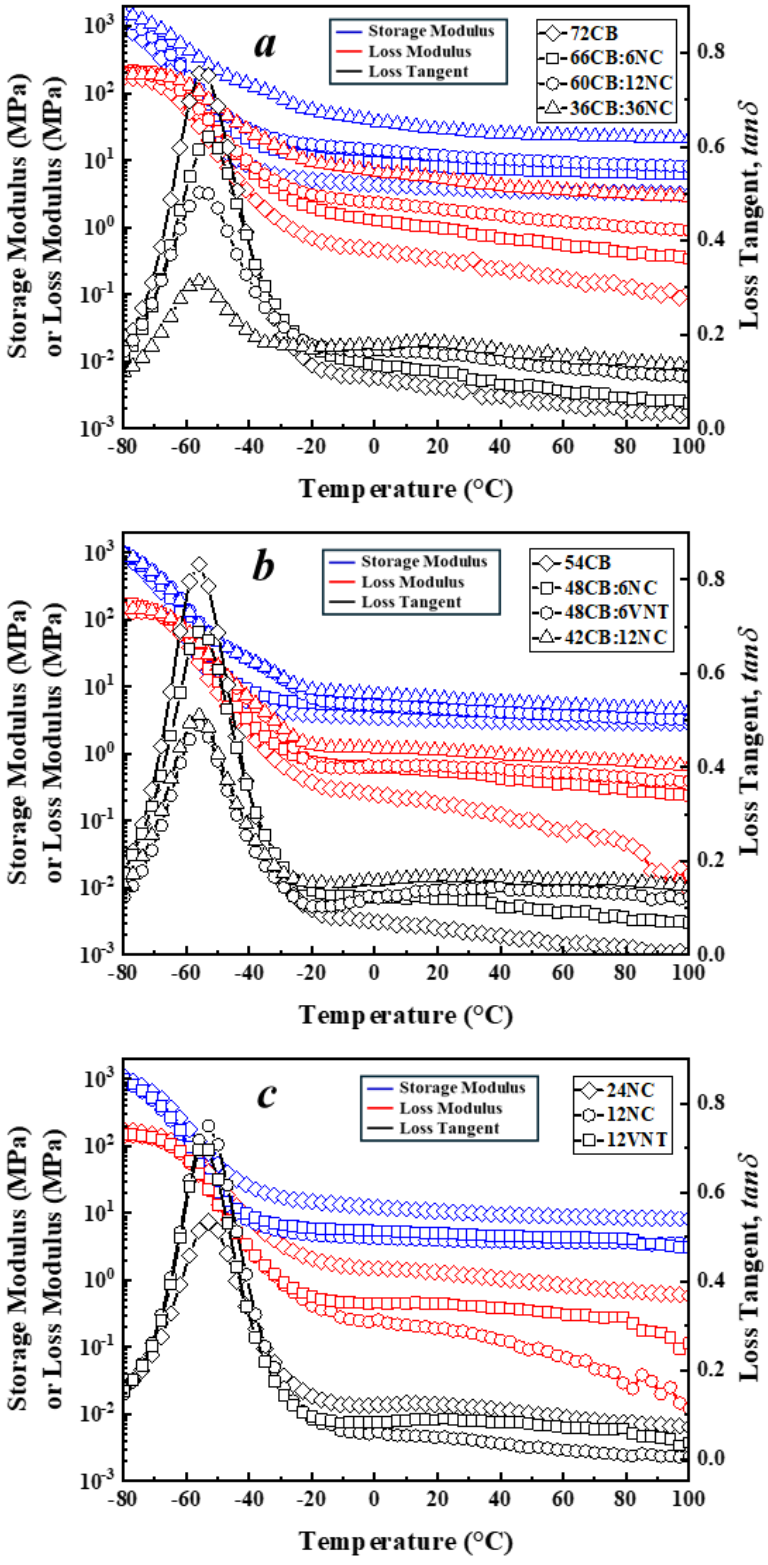

Figure 69: *Storage modulus, loss modulus, and loss tangent curves for SBR-BR composites containing (a) 72 phr filler, (b) 54 phr filler, and (c) CNTs only.*

Table 12: *Loss tangent values of SBR-BR compounds at reference temperatures.*

Compound	$tan\delta_{60°C}$	$tan\delta_{0°C}$	$tan\delta_{-20°C}$
72CB	0.05	0.11	0.13
66CB:6NC	0.08	0.13	0.17
60CB:12NC	0.13	0.17	0.18
36CB:36NC	0.15	0.18	0.17
54CB	0.02	0.07	0.10
48CB:6NC	0.09	0.12	0.14
48CB:6VNT	0.14	0.12	0.10
42CB:12NC	0.16	0.16	0.15
24NC	0.09	0.12	0.14
12NC	0.02	0.06	0.09
12VNT	0.07	0.08	0.10

6.6 Surface chemistry effects

Figure 70 presents vulcanization curves for SBR-BR compounds containing sulfur doped CNTs along with the corresponding compounds with equivalent filler systems with unfunctionalized CNTs. The rate of curing is faster for SBR-BR compounds containing sulfur-doped CNTs; note that the total amount of sulfur was the same with and without sulfur-doped CNTs. However, because sulfur is added to the mixer earlier in this case as a component of the milled CNT-sulfur powder, this result may indicate scorching. However, the fact that the initial torque of SBR-BR composites has negligible variance suggests that any scorching effects are minimal or partial in explaining the faster rate of cure. The expanded mixing time for sulfur could

lead to enhanced dispersion in the compound and better interaction with the accelerating agent, which could increase the rate of curing. In the context of industrial applications for tire rubber manufacturing and raw compound vulcanization, accelerator content can be changed to tune the curing process. Additionally, retarders can be added to slow the initial rates of cure if scorching is an issue.

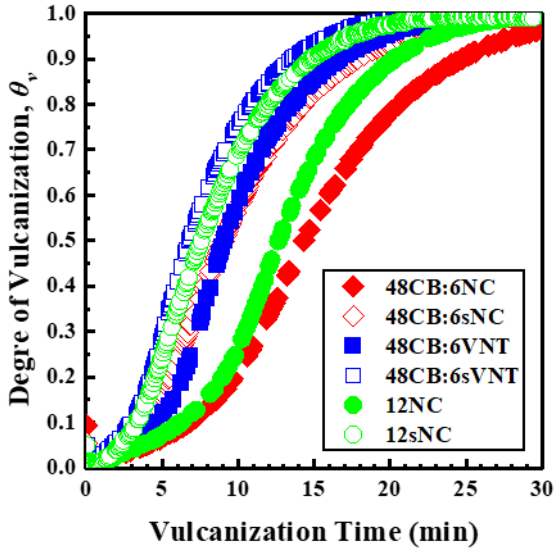

Figure 70: *Sulfur doping effects on SBR-BR vulcanization kinetics.*

The tensile mechanical properties of SBR-BR compounds containing sulfur functionalized CNTs are presented in Figure 71. For both 48CB:6CNT filler systems, the tensile strength marginally increases from 5.7 MPa to 6.4 MPa for NC7000 and from 6.5 MPa to 7.0 MPa for VNT100 upon sulfur functionalization. For the 48CB:6sNC compound, this enhancement in strength is shown in simultaneous enhancements in initial stiffness and failure strain, perhaps due to enhanced rubber-CNT interactions due to sulfur functionalization. However, for the 48CB:6sVNT compound, the Young's modulus (1.9 MPa) is notably decreased compared to the

unfunctionalized 48CB:6VNT counterpart (3.9 MPa), which can be attributed to the significant aspect ratio reduction due to milling. However, the failure strain increases substantially such that the tensile strength experiences a net increase compared to 48CB:6VNT. For only low NC7000 content, the mechanochemical sulfur doping process also results in reduced stiffness (2.5 MPa to 1.5 MPa), however in this case leading to a net decrease in tensile strength (3.2 MPa to 2.5 MPa). Thus, the sulfur doping process appears to be best for higher total filler loadings with low CNT content.

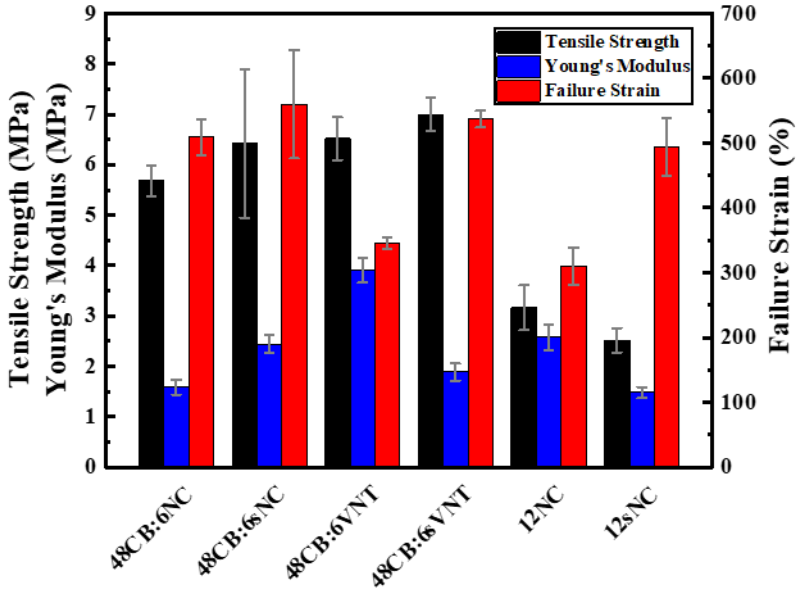

Figure 71: *Effect of sulfur doping on tensile mechanical properties of SBR-BR composites.*

Figure 72 presents the abrasion resistance of SBR-BR composites containing sulfur functionalized CNTs. For both 48CB:6CNT systems and 12 phr sNC, the abrasion resistance is notably better compared to the unfunctionalized counterparts. For 48CB:6NC, the mass loss during abrasion testing decreases from 140 mg to 114 mg (19% reduction) upon sulfur functionalization.

Similarly for both 48CB:6VNT and 12NC, sulfur functionalization of the CNTs results in a 20% improvement in abrasion resistance. The improvements in abrasion resistance for the 48CB:6CNT systems mimic the enhanced tensile strength. However, for 12 phr NC, the abrasion resistance is improved despite a reduction is tensile strength. Thus, while compound tensile strength is largely related to abrasion resistance, there may be additional effects of rubber-CNT adhesion strength.

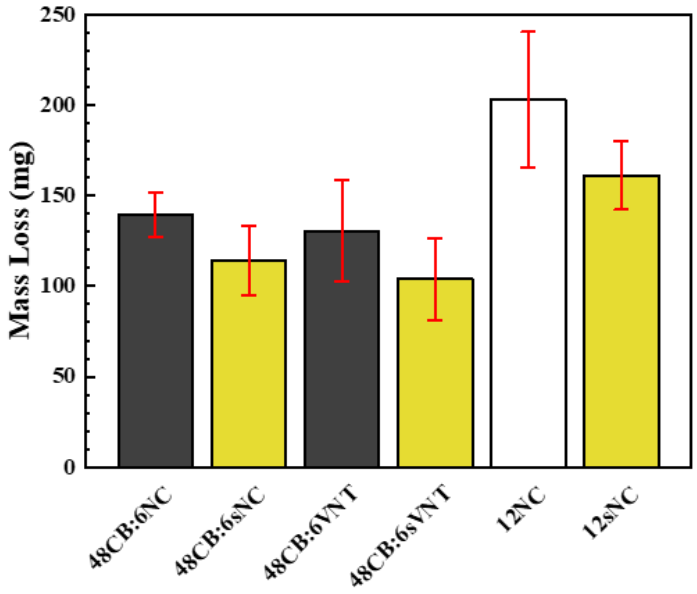

Figure 72: *Sulfur doping effects on the abrasion resistance of SBR-BR compounds.*

Figure 73 presents the loss tangent of SBR-BR composites containing sulfur doped NC7000 and VNT100. For the 48CB:6VNT system, in the wet/ice traction temperature region between -20 °C and 0 °C, both the wet and ice traction characteristics appear to be improved upon sulfur functionalization as evidenced by higher *tanδ* values. However, for 48CB:6sNC, the loss tangent in this temperature regime is slightly lower than that for the unfunctionalized counterpart, suggesting worse traction characteristics. This worse traction behavior is magnified for 12sNC, especially at -20 °C. However, while the effects of mechanochemical sulfur functionalization on

the traction of SBR-BR compounds is mixed, *tanδ* values at 60 °C are all slightly reduced for compounds containing sulfur functionalized CNTs, indicating better polymer-CNT interactions and a slightly reduced rolling resistance for these compounds.

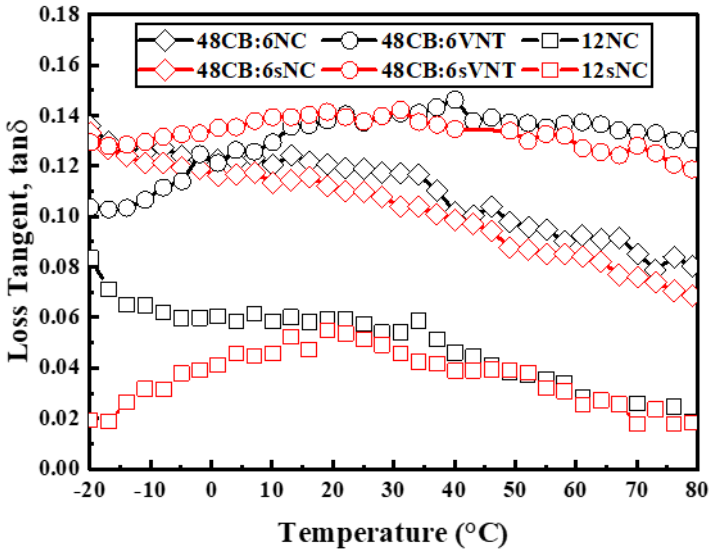

Figure 73: *Sulfur doping effects on the loss tangent of SBR-BR composites containing dual CB:CNT fillers.*

While the improvements in tensile mechanical properties and rolling resistance are marginal, the notably enhanced abrasion resistance suggests there may be improved rubber-CNT interaction due to the presence of sulfur-containing functional groups on CNT surfaces. However, it should be noted that CNT dispersion is likely not improved due to sulfur functionalization, but rather the chemical interactions with the rubber polymer chains are enhanced. For the previously studied polycarbonate system filled with mechanochemically functionalized CNTs via ball milling with ammonium carbonate, CNTs could interact with polycarbonate chains via weak but prevalent hydrogen bonding between hydroxyl and carboxyl groups on CNT surfaces and oxygen atoms of

PC carbonate groups. In the case of the SBR-BR system filled with sulfur-doped CNTs, no such hydrogen bonding interactions can occur as polystyrene-butadiene and polybutadiene chains contain no strong hydrogen bonding acceptors like oxygen or nitrogen. Thus, the notable improvements in compound properties are attributed to the strengthened interface between SBR-BR chains and CNTs from the formation of covalently bonded sulfur bridges during vulcanization, as depicted in Figure 74.

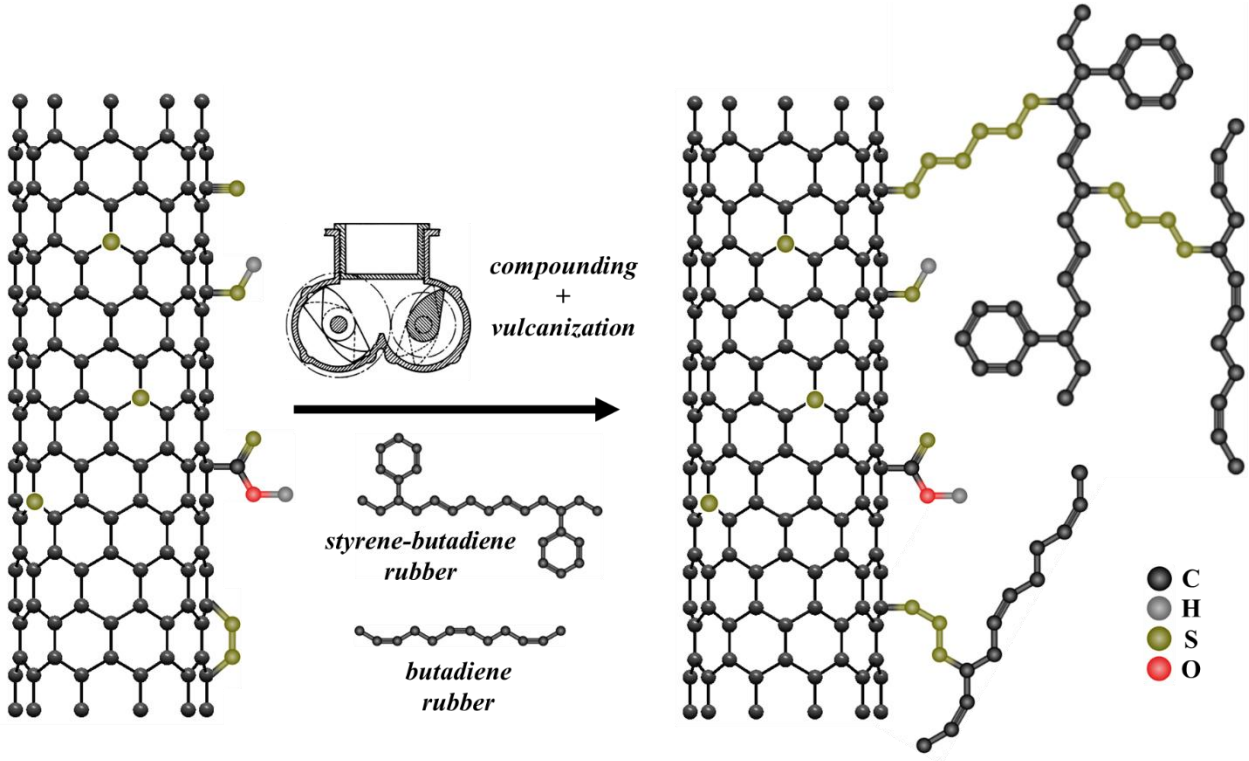

Figure 74: *Schematic of sulfur-doped CNT interaction with vulcanization SBR-BR rubber.*

Regarding the mechanical properties of SBR-BR composites, sulfur bridges between CNTs and rubber chains would expect to result in increased stiffness. This effect is seen primarily for 48CB:6sNC as the Young's modulus increased compared to 48CB:6NC. However, for 48CB:sVNT, the increased stiffness due to sulfur linkages is counteracted by higher aspect ratio

reduction (compared to NC7000) upon mechanochemical functionalization with sulfur. Despite the reduction in aspect ratio, tensile strength is still improved as the sulfur bridges prevent chain slippage and eventual mechanical failure until higher strains are reached compared to the unfunctionalized counterpart. Regarding abrasion resistance, the blanket improvement for all compounds containing sulfur functionalized CNTs can be directly attributed to the enhanced interfacial strength between the CNTs and the rubber chains. While the bulk stiffness and strength of the composite is highly related to abrasion strength, molecular level covalent interactions appear to play a large role, even outweighing reduced stiffness and strength in the case of 12 phr NC7000. While the dispersion of the CNTs may not be greatly improved upon functionalization, the enhancement in chemical interactions with the rubber chains was enough to slightly reduce the loss tangent of SBR-BR compounds containing sulfur functionalized CNTs compared to those containing functionalized CNTs in the rolling resistance temperature regime. Thus, mechanochemical modification of CNTs with elemental sulfur largely improves the properties of SBR-BR composites containing small amounts of CNTs within a larger CB reinforcement system and could serve as the first step in partially or fully replacing carbon black in tire tread rubber for lightweighting and improved fuel economy.

Chapter 7: Conclusions

In Chapter 3, it was shown that multiwalled carbon nanotubes possess a minimum single impact energy threshold for fracture that is dependent on diameter, wall morphology, and bulk morphology. Additionally, the length reduction kinetics of initially short CNTs were able to be modeled by a simple exponential expression relating a normalized length term to the cumulative impact energy of milling. The kinetic length reduction behavior was found to also apply for ultralong CNTs, suggesting the length reduction of carbon nanotubes with widely varying morphologies can be predictably controlled using a simple ball milling process.

In Chapter 4, multiple facile mechanochemical carbon nanotube functionalization approaches were investigated. Milling CNTs in the presence of ammonium carbonate added a variety of oxygen containing functional groups to nanotube surfaces, most notably hydroxyl (R-OH) and carboxyl (R-COOH) groups. The degree of functionalization for dry milled CNTs was found to follow a power law relationship with cumulative impact energy, suggesting there may be a parallel with Freundlich-type adsorption behavior, while aqueous milling resulted in a relatively linear relationship between degree of functionalization and milling time. Milling CNTs in the presence of melamine was found to non-covalently functionalized CNTs via π-π interactions. Similarly to functionalization with ammonium carbonate, the degree of melamine functionalization was found to scale with milling duration. Finally, milling CNTs in the presence of sulfur was found to result in a variety of sulfur-containing covalently bonded functional groups as well as physically adsorbed sulfur. These simple, scalable, solvent-free CNT functionalization approaches could prove effective in a large-scale industrial setting.

In Chapter 5, the effects of carbon nanotube aspect ratio and surface chemistry on polycarbonate-nanotube composites were investigated. Compounding initially ultrahigh aspect

ratio CNTs was found to result in high melt viscosities. Additionally, these ultrahigh aspect ratio CNTs were found to not disperse well in polycarbonate due to the initial bundle morphology, likened to the interleaved pages of a book, leading to rheological and electrical percolation thresholds over an order of magnitude higher than expected based on percolation theory. Ball milling the ultrahigh aspect ratio CNTs to shorter lengths significantly improved their processability in PC by reducing melt viscosity and polymer degradation. However, while the agglomeration of plain milled CNTs was found to reduce significantly in the PC composites, the individual level CNT dispersion was found to be worse than even for the pristine ultrahigh aspect ratio CNTs, suggesting plain ball milling is not a suitable method for simultaneously improving processability and dispersion of CNTs in polymers. Upon mechanochemical functionalization of CNTs with ammonium carbonate, the percolation behavior of functionalized CNTs was found to be significantly improved compared to plain milled CNTs of the same aspect ratio, suggesting the enhanced chemical interactions between the functionalized CNTs and polycarbonate chains via weak but prevalent hydrogen bonding improves dispersion.

In Chapter 6, the efficacy of the partial or full replacement of carbon black with carbon nanotubes in a passenger tire tread rubber formulation was investigated. Ultrahigh aspect ratio CNTs were shown to impart a higher degree of mechanical reinforcement and abrasion resistance compared to lower aspect ratio CNTs and carbon black. While the traction characteristics of rubber compounds containing ultrahigh aspect ratio CNTs were improved compared to those containing lower aspect ratio CNTs or CB, the rolling resistance was significantly increased. However, mechanochemical functionalization of CNTs with sulfur before compounding with rubber resulted in further improved mechanical strength and abrasion resistance while also reducing rolling resistance due to enhanced chemical interactions between CNTs and rubber chains from the

formation of sulfur bridges during vulcanization. While further study would be necessary to confidently suggest CNTs can partially or fully replace CB in tire tread rubber, the findings of this work suggest there may be merit to this proposal if dispersion and CNT-rubber interactions can be maximized, leading to low rolling resistance and improved fuel economy.

Chapter 8: Recommendations

While the research presented here added valuable insights into carbon nanotube length and surface chemistry modification by planetary ball milling and their subsequent effects on polymer composites, further work is recommended in a few areas. The first would be to investigate how the length reduction kinetics of carbon nanotubes vary with different types of ball mills. Whereas vertically oriented planetary ball mills are popular in laboratory settings for imparting high impact energies and working with small sample sizes, industrial scale ball milling typically uses horizontal mills with larger volume capacities. While the Burgio-Rojac model is specific to planetary ball milling, energy models do exist for different ball mill configurations, suggesting the length reduction kinetics found in this study may be able to extrapolated to different types of ball mills by substituting the appropriate term for cumulative impact energy into the exponential expression related to normalized CNT length. Investigating the effects of grinding media configuration, rotational speed, and milling during would prove or disprove if the length reduction kinetics change based on mill configuration.

A limitation of the mechanochemical functionalization work presented here is the inability to eliminate ambient oxygen and humidity from the grinding vessel. Decoupling the effects of ambient oxygen and humidity from functionalization due to the introduction of other species to the mill can be achieved by using a grinding vessel compatible with a vacuum pump or by using a glove box during sample preparation and vessel loading. In this case, any functionalization effects would be solely due to the addition of the functionalizing species rather than a combination of effects with ambient oxygen and humidity. Additionally, while the adsorption behavior of carbon nanotubes before and after plain ball milling has been studied previously, the in-situ adsorption behavior of CNTs via mechanochemical functionalization is a largely unstudied area. If the

pressure inside the vessel could be tracked during milling and the effect of milling energy on CNT surface area was known, the relationship between surface coverage and partial pressure of functionalizing species could be expressed in the context of Langmuir, Freundlich, etc. adsorption behavior.

A simple but important recommendation for future work is to investigate the effect of purification of ultrahigh aspect ratio CNTs grown on vermiculite supports on CNT processability and dispersion in polymer composites. While the elimination of the purification step is a primary advantage of high yield CNT synthesis, the resulting bundle morphology was shown to result in poor dispersion in polycarbonate. Thus, removing the catalyst and support material from the pristine CNTs by acid treatment might allow bundles to be dispersed better or change the bulk morphology altogether. By subsequently compounding purified ultrahigh aspect ratio CNTs in polycarbonate and assessing the morphology of composites via microscopy and the percolation behavior via rheology and electrical conductivity, it would be interesting to see if the dispersion improved upon purification. This would confirm if the initial bulk morphology of the CNTs is the primary issue leading to poor dispersion or if there are other contributing factors.

To better determine the efficacy of partial or full replacement of carbon black with carbon nanotubes in tire tread rubber, a more recently developed tire tread compound should be tested. Of particular interest would be modifying the rubber base system to include a fraction of natural rubber, which typical has higher tensile strength and stiffness compared to synthetic rubber (like SBR and BR). Additionally, evaluating the amount and type of processing aid (paraffin oil in the case of this study) could have significant effects on the properties of the tread compound. The application of a more realistic industrial compounding process with a paired two- or three-roll mill and/or calendaring system alongside the internal mixer could improve the dispersion of the fillers.

With the recent emergence of silica fillers for tire tread rubber yielding improved rolling resistance and traction characteristics compared to carbon black, dual silica-CNT or triad silica-CB-CNT filler systems could result in low total filler contents required for superior mechanical strength along with low rolling resistance for improved fuel economy.

Appendix A: Sample Calculation for Burgio-Rojac Model

The single impact energy, E_b, is calculated by the following…

$$E_b = \frac{1}{2}\varphi_b\left(\rho_b\frac{\pi d_b^3}{6}\right)\omega_p^2\left[\left(\frac{\omega_v}{\omega_p}\right)^2\left(\frac{d_v-d_b}{2}\right)^2\left(1-2\frac{\omega_v}{\omega_p}\right)-2r_p\left(\frac{\omega_v}{\omega_p}\right)\left(\frac{d_v-d_b}{2}\right)-\left(\frac{\omega_v}{\omega_p}\right)^2\left(\frac{d_v-d_b}{2}\right)^2\right]$$

Fixed, known values include…

$\rho_b = 7{,}760\ \frac{kg}{m^3}$ (stainless steel density)

$d_v = 0.06\ m$ (grinding jar diameter)

$r_p = 0.0705\ m$ (effective sun plate radius)

For the small grinding media configuration, $d_b = 0.01\ m$ and $N_b = 25$…

The obstruction factor, φ_b, is calculated by the following…

$$\varphi_b = 1 - n_v^{\varepsilon}$$

where

$$n_v = \frac{N_b}{N_{b,v}}$$

$$N_{b,v} = \frac{\pi d_v^2 h_v}{4d_b^3}$$

$$0.95 = 1 - \left(\frac{N_{b,s}}{N_{b,v}}\right)^{\varepsilon}$$

$$N_{b,s} = \frac{\pi(d_v - d_b)h_v}{3d_b^2}$$

$N_{b,v}$ is the number of grinding balls needed to completely fill the grinding jar in a cubic arrangement, and thus n_v is the degree of filling of the grinding jar. $N_{b,s}$ is the number of grinding balls needed to cover one third of the inner surface area of the grinding jar in a cubic

arrangement and h_v is the height of the grinding jar (0.036 m for the 80 mL grinding jar).

Parameter ε is evaluated at $\varphi_b = 0.95$ with $N_{b,s}$ substituted for N_b. Thus…

$$N_{b,v} = \frac{\pi(0.06\ m)^2(0.036\ m)}{4(0.01\ m)^3} = 101.788$$

$$N_{b,s} = \frac{\pi(0.06\ m - 0.01\ m)(0.036\ m)}{3(0.01\ m)^2} = 18.850$$

$$0.95 = 1 - \left(\frac{18.850}{101.788}\right)^{\varepsilon} \rightarrow \varepsilon = 1.776$$

$$n_v = \frac{N_b}{N_{b,v}} = \frac{25}{101.788} = 0.246$$

$$\varphi_b = 1 - (0.246)^{1.776} = 0.917$$

Considering a rotational speed, ω_p, of 300 rpm…

$$\omega_p = 300\ \frac{rot}{min}\left(\frac{2\pi\ rad}{rot}\right)\left(\frac{min}{60\ s}\right) = 31.4\ \frac{rad}{s}$$

The speed ratio, ω_v/ω_p of the PM100 mill is -2, so…

$$\omega_v = -600\ \frac{rot}{min} = -62.8\ \frac{rad}{s}$$

Thus, the single impact energy can be calculated as…

$$E_b = \frac{1}{2}(0.917)\left[\left(7{,}760\ \frac{kg}{m^3}\right)\frac{\pi(0.01\ m)^3}{6}\right]\left(31.4\ \frac{rad}{s}\right)^2\left[(-2)^2\left(\frac{0.06\ m - 0.01\ m}{2}\right)^2(1 - 2(-2))\right.$$

$$\left. - 2(0.0705\ m)(-2)\left(\frac{0.06\ m - 0.01\ m}{2}\right) - (-2)^2\left(\frac{0.06\ m - 0.01\ m}{2}\right)^2\right]$$

$$= 0.0314\ J = 31.4\ mJ$$

The total cumulative energy is calculated from the following…

$$E_{cum} = E_b v_t t$$

And the total impact frequency is calculated by…

$$v_t = N_b K \left(\frac{\omega_p - \omega_v}{2\pi}\right)$$

The geometry factor, K, for 10 mm grinding ball is 1.5. Thus…

$$v_t = 25(1.5)\left(\frac{31.4\frac{rad}{s} - \left(-62.8\ \frac{rad}{s}\right)}{2\pi\ rad}\right) = 562.5\ s^{-1}$$

$$E_{cum} = \left(0.0314\ \frac{J}{impact}\right)\left(562.5\ \frac{impact}{s}\right)\left(30\ min * \frac{60\ s}{min}\right) = 31800\ J = 31.8\ kJ$$

For a minimum single impact energy, $E_{b,min}$, of 10 mJ, the excess single impact energy is…

$$E_b^* = E_b - E_{bmin} = 31.4\ mJ - 10\ mJ = 21.4\ mJ$$

And the excess cumulative energy is…

$$E_{cum}^* = E_b^* v_t t = \left(0.0214\ \frac{J}{impact}\right)\left(562.5\ \frac{impact}{s}\right)\left(30\ min * \frac{60\ s}{min}\right) = 21700\ J = 21.7\ kJ$$

Appendix B: XPS O1s/N1s Core Level Scans of Functionalized CNTs

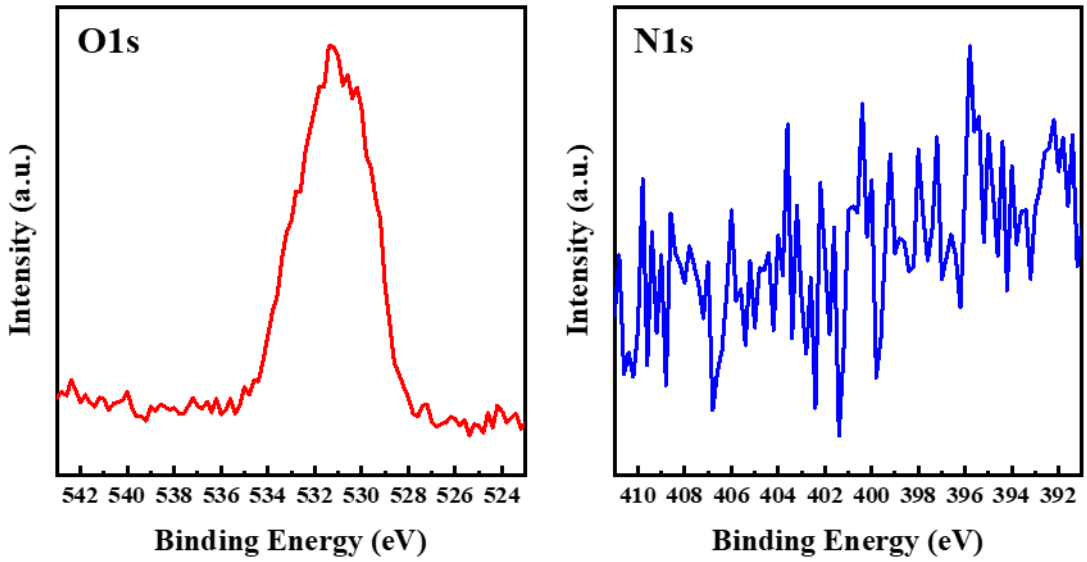

Figure B1: *O1s and N1s scans of pristine VNT100.*

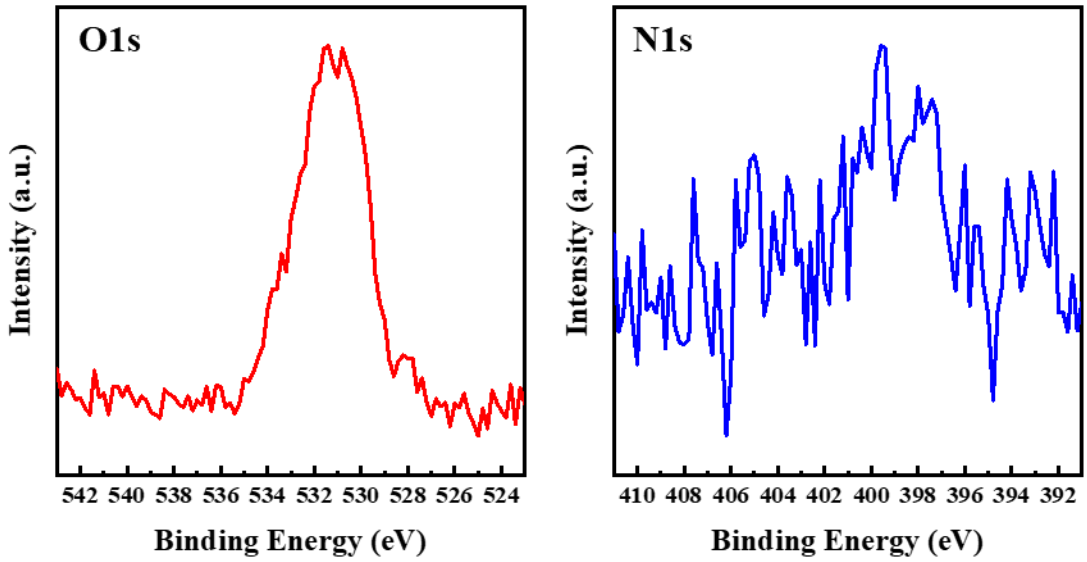

Figure B2: *O1s and N1s scans of pristine NC7000.*

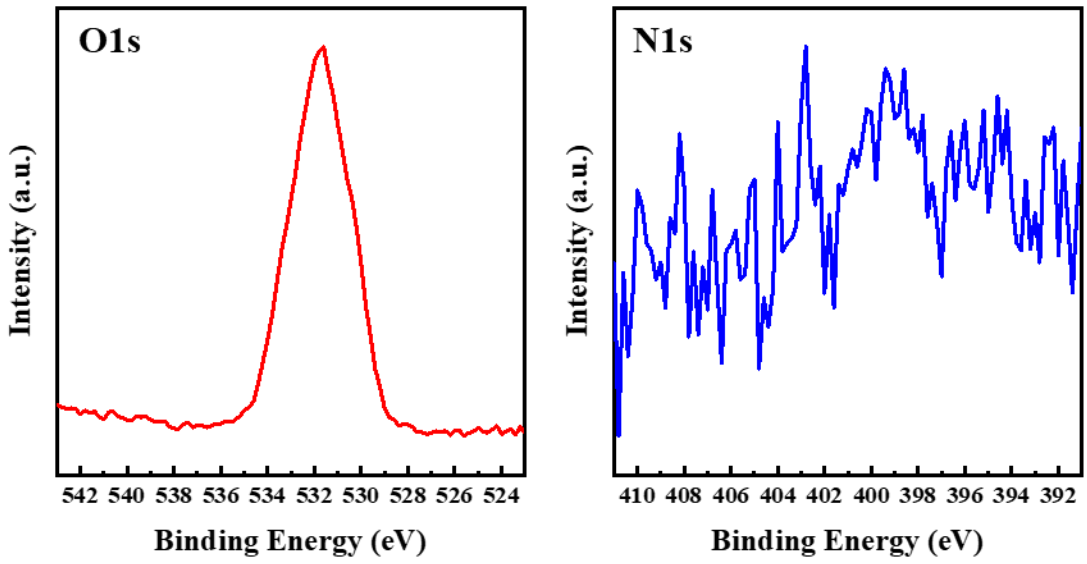

Figure B3. *O1s and N1s scans of dfVNT milled at 300 rpm for 30 min.*

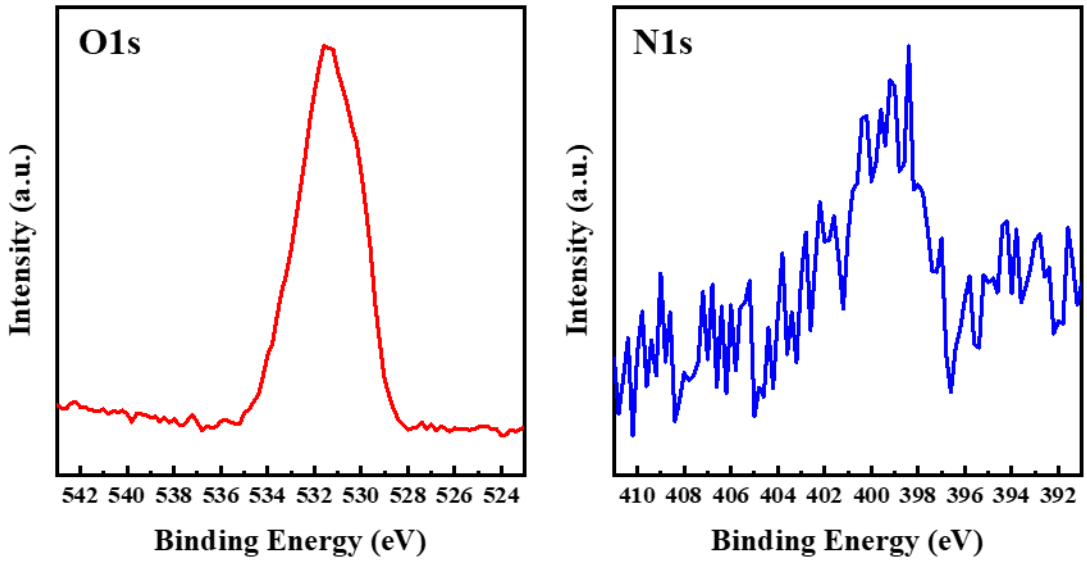

Figure B4: *O1s and N1s scans of dfVNT milled at 300 rpm for 1 hr.*

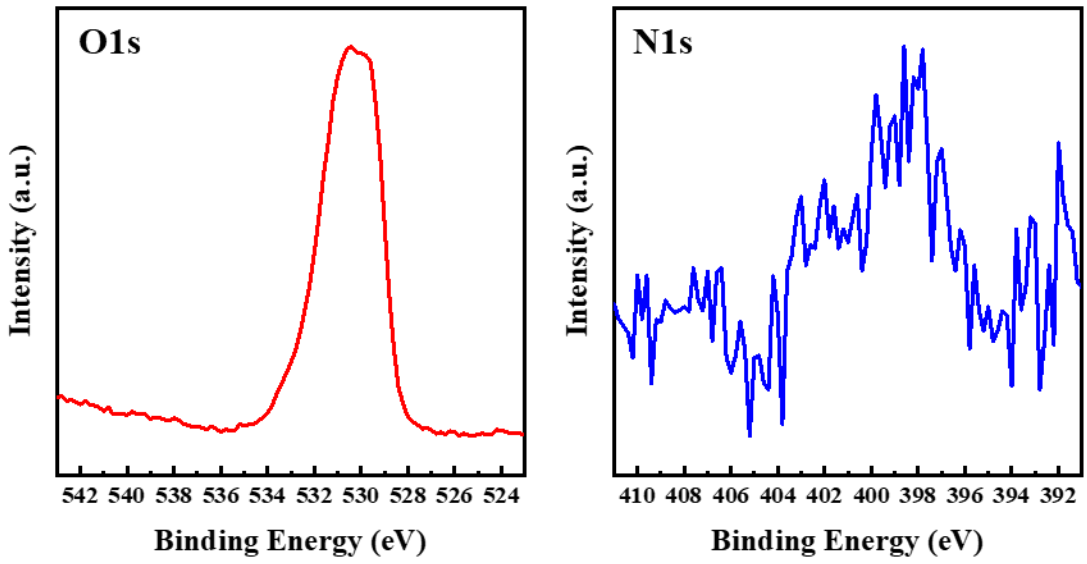

Figure B5: *O1s and N1s scans of dfVNT milled at 300 rpm for 4 hr.*

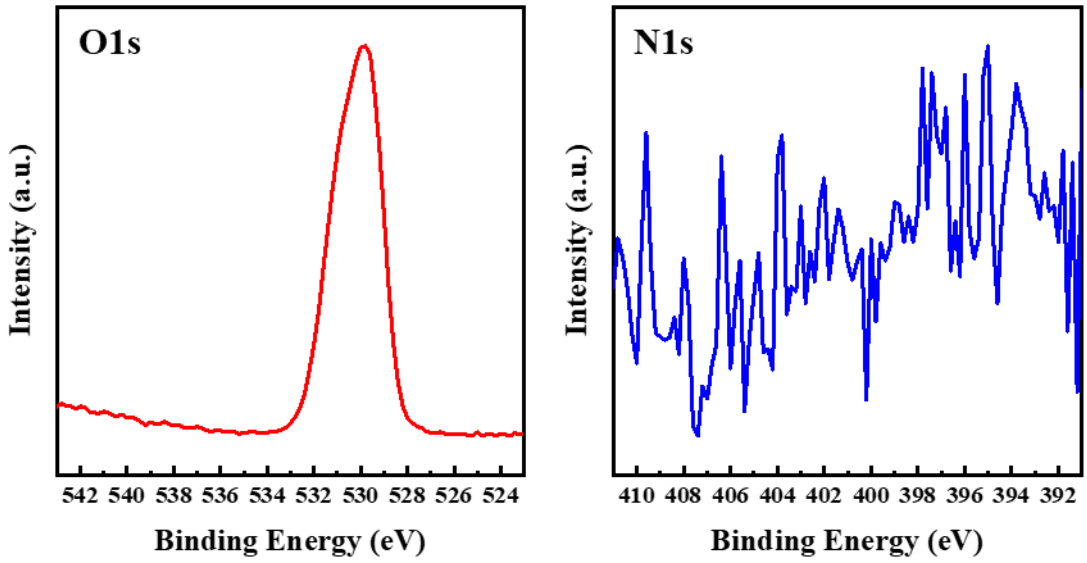

Figure B6: *O1s and N1s scans of afVNT milled at 300 rpm for 30 min.*

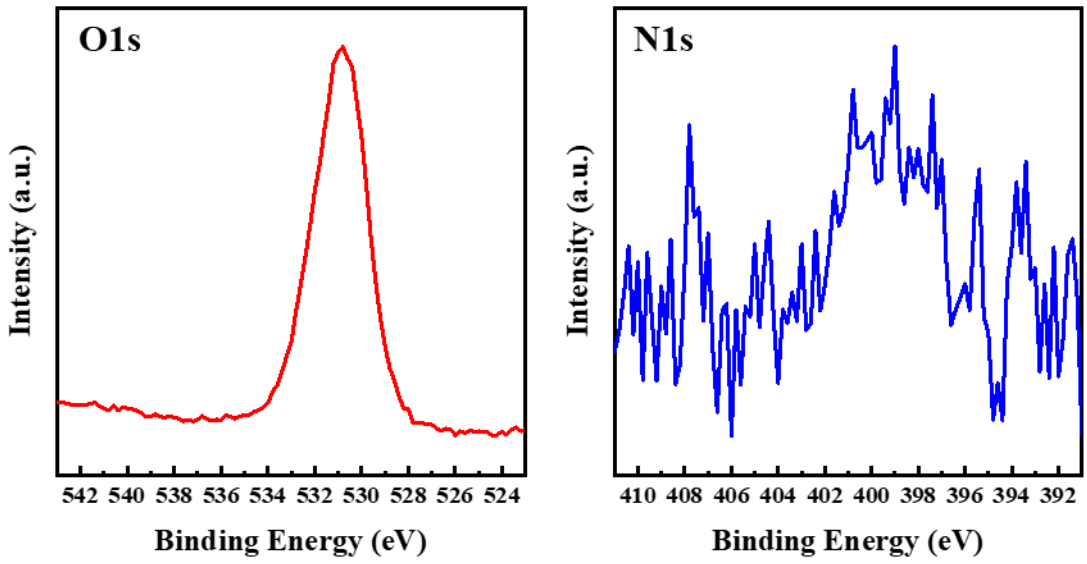

Figure B7: *O1s and N1s scans of afVNT milled at 300 rpm for 1 hr.*

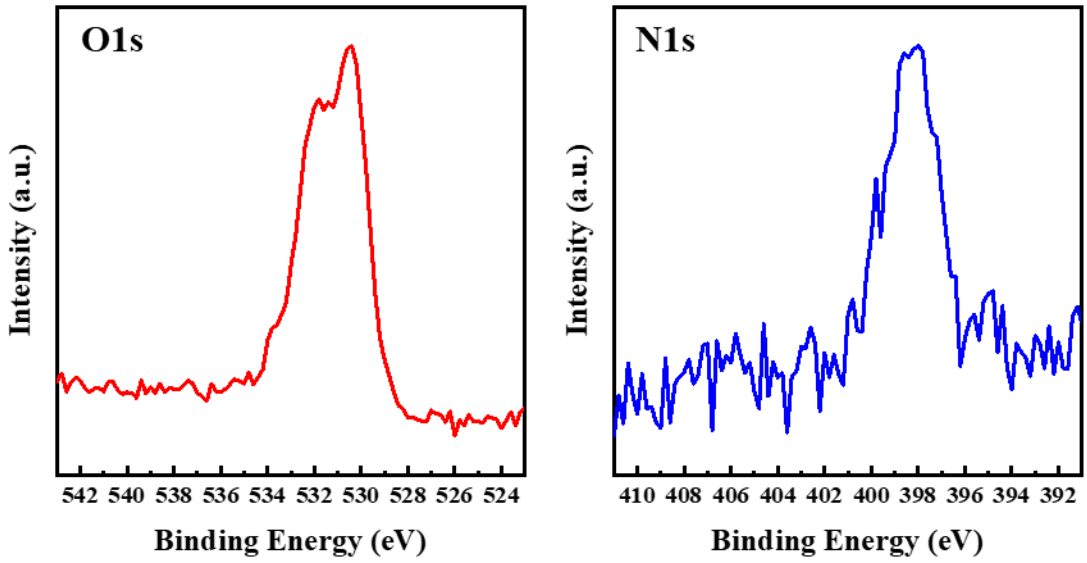

Figure B8: *O1s and N1s scans of afVNT milled at 300 rpm for 4 hr.*

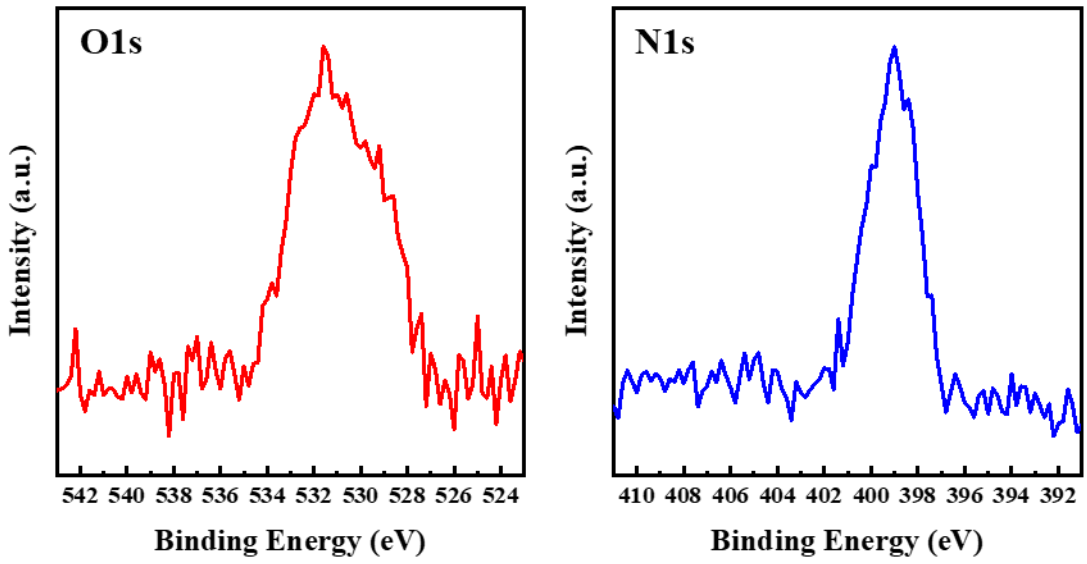

Figure B9: *O1s and N1s scans of melNC milled at 300 rpm for 30 min.*

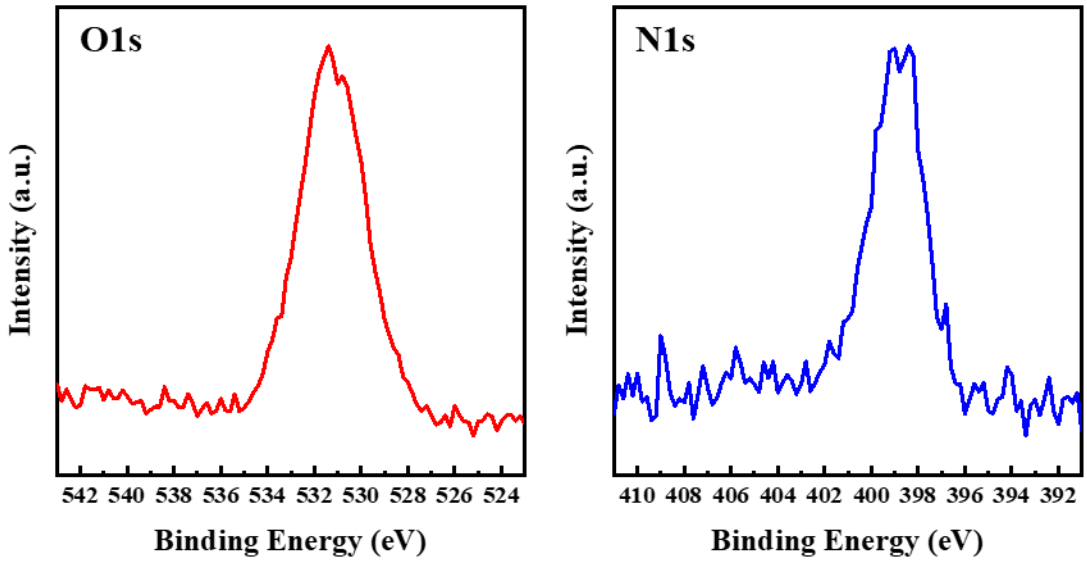

Figure B10: *O1s and N1s scans of melNC milled at 300 rpm for 1 hr.*

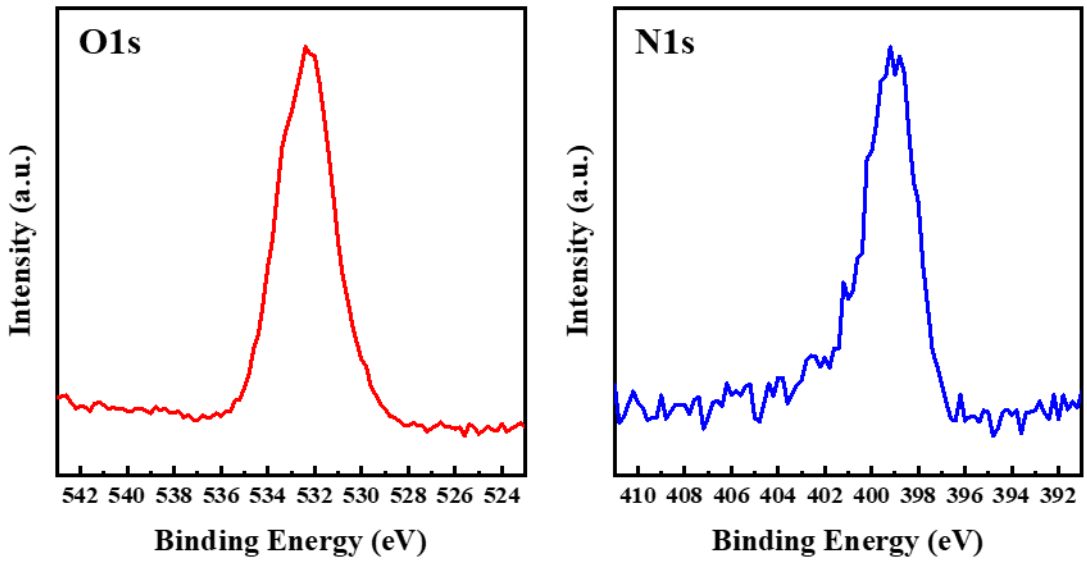

Figure B11: *O1s and N1s scans of melNC milled at 300 rpm for 4 hr.*

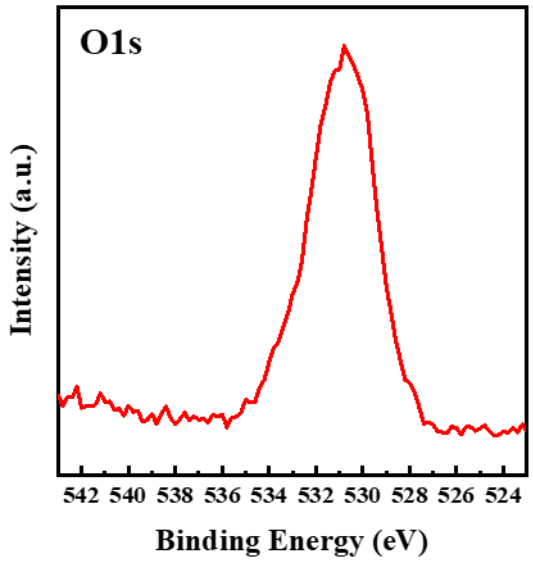

Figure B12: *O1s scan of sVNT milled at 300 rpm for 1hr.*

References

1. Iijima, S., *Helical microtubules of graphitic carbon.* Nature, 1991. **354**(6348): p. 56-58.
2. Zhang, L., et al., *Bamboo and Herringbone Shaped Carbon Nanotubes and Carbon Nanofibres Synthesized in Direct Current-Plasma Enhanced Chemical Vapour Deposition.* Journal of Nanoscience and Nanotechnology, 2009. **9**(7): p. 4502-4506.
3. Liu, F., P. Ming, and J. Li, *Ab initio calculation of ideal strength and phonon instability of graphene under tension.* Physical Review B, 2007. **76**(6): p. 064120.
4. Spear, K.E. and J.P. Dismukes, *Synthetic Diamond: Emerging CVD Science and Technology*. 1994: Wiley.
5. Yu, M.-F., et al., *Strength and Breaking Mechanism of Multiwalled Carbon Nanotubes Under Tensile Load.* Science, 2000. **287**(5453): p. 637-640.
6. Peng, B., et al., *Measurements of near-ultimate strength for multiwalled carbon nanotubes and irradiation-induced crosslinking improvements.* Nature Nanotechnology, 2008. **3**(10): p. 626-631.
7. Forro, L., et al., *Electronic and Mechanical Properties of Carbon Nanotubes*, in *Science and Application of Nanotubes*, M.F. Thorpe, D. Tománek, and R.J. Enbody, Editors. 2002, Springer US: Boston, MA. p. 297-320.
8. Jack, D.A., et al., *Electrical conductivity modeling and experimental study of densely packed SWCNT networks.* Nanotechnology, 2010. **21**(19).
9. Lekawa-Raus, A., et al., *Electrical transport in carbon nanotube fibres.* Scripta Materialia, 2017. **131**: p. 112-118.
10. Flygare, M. and K. Svensson, *Influence of crystallinity on the electrical conductivity of individual carbon nanotubes.* Carbon Trends, 2021. **5**.

11. Kumanek, B. and D. Janas, *Thermal conductivity of carbon nanotube networks: a review.* Journal of Materials Science, 2019. **54**(10): p. 7397-7427.

12. Liang, X., et al., *Enhancing the strength, toughness, and electrical conductivity of twist-spun carbon nanotube yarns by π bridging.* Carbon, 2019. **150**: p. 268-274.

13. Jensen, B.D., et al., *Modeling Carbon Nanotube Entanglement Load Transfer: Implications for Lightweight Aerospace Structures.* Acs Applied Nano Materials, 2023. **6**(11): p. 9558-9568.

14. Nguyen, A.N., et al., *Carbon Nanotube Yarns Tailored Using Dispersants and Surfactants for Flexible and Wearable Thermoelectric Generators.* ACS Applied Nano Materials, 2024. **7**(9): p. 9880-9886.

15. Ma, R.Z., et al., *Study of electrochemical capacitors utilizing carbon nanotube electrodes.* Journal of Power Sources, 1999. **84**(1): p. 126-129.

16. Landi, B.J., et al., *Carbon nanotubes for lithium ion batteries.* Energy & Environmental Science, 2009. **2**(6): p. 638-654.

17. Li, W.Z., et al., *Preparation and characterization of multiwalled carbon nanotube-supported platinum for cathode catalysts of direct methanol fuel cells.* Journal of Physical Chemistry B, 2003. **107**(26): p. 6292-6299.

18. Corry, B., *Designing carbon nanotube membranes for efficient water desalination.* Journal of Physical Chemistry B, 2008. **112**(5): p. 1427-1434.

19. Cong, H.L., et al., *A smart temperature and magnetic-responsive gating carbon nanotube membrane for ion and protein transportation.* Scientific Reports, 2016. **6**.

20. Bianco, A., K. Kostarelos, and M. Prato, *Applications of carbon nanotubes in drug delivery.* Current Opinion in Chemical Biology, 2005. **9**(6): p. 674-679.

21. Harrison, B.S. and A. Atala, *Carbon nanotube applications for tissue engineering.* Biomaterials, 2007. **28**(2): p. 344-353.

22. Laurent, C., E. Flahaut, and A. Peigney, *The weight and density of carbon nanotubes versus the number of walls and diameter.* Carbon, 2010. **48**(10): p. 2994-2996.

23. Tang, W.Z., M.H. Santare, and S.G. Advani, *Melt processing and mechanical property characterization of multi-walled carbon nanotube/high density polyethylene (MWNT/HDPE) composite films.* Carbon, 2003. **41**(14): p. 2779-2785.

24. Zhu, K.L., et al., *Crystallization, rheological behavior and mechanical properties of carbon nanotube/metallocene polypropylene composites.* Materials Research Express, 2023. **10**(2).

25. Wang, J.D., et al., *Preparation and mechanical properties of natural rubber powder modified by carbon nanotubes.* Journal of Applied Polymer Science, 2006. **100**(6): p. 4697-4702.

26. Deng, F., et al., *Elucidation of the Reinforcing Mechanism in Carbon Nanotube/Rubber Nanocomposites.* Acs Nano, 2011. **5**(5): p. 3858-3866.

27. Li, X.F., K.T. Lau, and Y.S. Yin, *Mechanical properties of epoxy-based composites using coiled carbon nanotubes.* Composites Science and Technology, 2008. **68**(14): p. 2876-2881.

28. Allaoui, A., et al., *Mechanical and electrical properties of a MWNT/epoxy composite.* Composites Science and Technology, 2002. **62**(15): p. 1993-1998.

29. Ivanov, S.G., A. Aniskevich, and V. Kulakov, *Simplified Calculation of the Electrical Conductivity of Composites with Carbon Nanotubes.* Mechanics of Composite Materials, 2018. **54**(1): p. 61-70.

30. Kulakov, V., et al., *Effective electrical conductivity of carbon nanotube-epoxy nanocomposites.* Journal of Composite Materials, 2017. **51**(21): p. 2979-2988.

31. Hong, W.T. and N.H. Tai, *Investigations on the thermal conductivity of composites reinforced with carbon nanotubes.* Diamond and Related Materials, 2008. **17**(7-10): p. 1577-1581.

32. Naskar, A.K., J.K. Keum, and R.G. Boeman, *Polymer matrix nanocomposites for automotive structural components.* Nature Nanotechnology, 2016. **11**(12): p. 1026-1030.

33. Huebner, B., *Novel Composites for Lightweighting in Deep Space Applications.* AM&P Technical Articles, 2024. **182**(5): p. 24-28.

34. Karimian, A., et al., *High flexible additively manufactured nanocomposite textiles with desirable thermoelectric properties.* Polymer Composites, 2023. **44**(3): p. 1617-1635.

35. Al-Saleh, M.H. and U. Sundararaj, *Electromagnetic interference shielding mechanisms of CNT/polymer composites.* Carbon, 2009. **47**(7): p. 1738-1746.

36. Thomassin, J.M., et al., *Multiwalled carbon Nanotube/Poly(ε-caprolactone) nanocomposites with exceptional electromagnetic interference shielding properties.* Journal of Physical Chemistry C, 2007. **111**(30): p. 11186-11192.

37. Awasthi, K., A. Srivastava, and O.N. Srivastava, *Synthesis of carbon nanotubes.* Journal of Nanoscience and Nanotechnology, 2005. **5**(10): p. 1616-1636.

38. Hernadi, K., et al., *Fe-catalyzed carbon nanotube formation.* Carbon, 1996. **34**(10): p. 1249-1257.

39. Hernadi, K., et al., *Carbon nanotubes production over Co/silica catalysts.* Catalysis Letters, 1997. **48**(3-4): p. 229-238.

40. Ricardo, P.S. and A. Dave, *In-situ synthesis of carbon nanotubes-graphite hybrid materials.* Catalysis Today, 2024. **429**.

41. Zhang, Q., et al., *Carbon Nanotube Mass Production: Principles and Processes.* ChemSusChem, 2011. **4**(7): p. 864-889.

42. Tessonnier, J.-P. and D.S. Su, *Recent Progress on the Growth Mechanism of Carbon Nanotubes: A Review.* ChemSusChem, 2011. **4**(7): p. 824-847.

43. *Alibaba.com*. February 7, 2025]; Available from: https://www.alibaba.com/trade/search?spm=a2700.galleryofferlist.the-new-header_fy23_pc_search_bar.keydown__Enter&tab=all&SearchText=multiwalled+carbon+nanotubes.

44. *Carbon black price index*, in *Price Indexes*. 2025: Business Analytiq.

45. Red'kin, A.N., et al., *Chemical Vapor Deposition of Carbon Nanotube Layers on Aluminum Foil.* Inorganic Materials, 2017. **53**(2): p. 148-153.

46. Robertson, J., et al., *Chemical vapor deposition of carbon nanotube forests.* Physica Status Solidi B-Basic Solid State Physics, 2012. **249**(12): p. 2315-2322.

47. Wang, K.K., et al., *Controlled synthesis, properties, and applications of ultralong carbon nanotubes.* Nanoscale Advances, 2024.

48. Sugime, H., et al., *Gd-Enhanced Growth of Multi-Millimeter-Tall Forests of Single-Wall Carbon Nanotubes.* ACS Nano, 2019. **13**(11): p. 13208-13216.

49. Briggs, N.M. and S.P. Crossley, *Rapid growth of vertically aligned multi-walled carbon nanotubes on a lamellar support.* Rsc Advances, 2015. **5**(102): p. 83945-83952.

50. Huang, J.Q., et al., *Efficient synthesis of aligned nitrogen-doped carbon nanotubes in a fluidized-bed reactor.* Catalysis Today, 2012. **186**(1): p. 83-92.

51. Destrée, A., et al., *Synthesis and characterization of carbon nanotubes grown on montmorillonite clay catalysts.* Journal of Materials Science, 2007. **42**(20): p. 8671-8689.

52. Bavlnka, C., et al., *High-yield synthesis of vertically aligned carbon nanotube arrays on acid-treated vermiculite.* Fullerenes Nanotubes and Carbon Nanostructures, 2025.

53. Halpin, J.C. and J.L. Kardos, *HALPIN-TSAI EQUATIONS - REVIEW.* Polymer Engineering and Science, 1976. **16**(5): p. 344-352.

54. Stauffer, D. and A. Aharony, *Introduction To Percolation Theory*. Revised 2nd ed. 1994: Taylor & Francis.

55. Jung, S., et al., *Modeling Electrical Percolation to optimize the Electromechanical Properties of CNT/Polymer Composites in Highly Stretchable Fiber Strain Sensors.* Scientific Reports, 2019. **9**(1): p. 20376.

56. Zeng, X., et al., *Characteristics of the Electrical Percolation in Carbon Nanotubes/Polymer Nanocomposites.* The Journal of Physical Chemistry C, 2011. **115**(44): p. 21685-21690.

57. Hu, G., et al., *Low percolation thresholds of electrical conductivity and rheology in poly(ethylene terephthalate) through the networks of multi-walled carbon nanotubes.* Polymer, 2006. **47**(1): p. 480-488.

58. Xie, L. and Y.T. Zhu, *Tune the phase morphology to design conductive polymer composites: A review.* Polymer Composites, 2018. **39**(9): p. 2985-2996.

59. Mondal, R.K., K.A. Dubey, and Y.K. Bhardwaj, *Role of the interface on electron transport in electro-conductive polymer-matrix composite: A review.* Polymer Composites, 2021. **42**(6): p. 2614-2628.

60. Castillo, F.Y., et al., *Electrical, mechanical, and glass transition behavior of polycarbonate-based nanocomposites with different multi-walled carbon nanotubes.* Polymer, 2011. **52**(17): p. 3835-3845.

61. Lin, B., U. Sundararaj, and P. Potschke, *Melt mixing of polycarbonate with multi-walled carbon nanotubes in miniature mixers.* Macromolecular Materials and Engineering, 2006. **291**(3): p. 227-238.

62. Kim, B., J. Lee, and I.S. Yu, *Electrical properties of single-wall carbon nanotube and epoxy composites.* Journal of Applied Physics, 2003. **94**(10): p. 6724-6728.

63. Mierczynska, A., et al., *Electrical and mechanical properties of carbon nanotube/ultrahigh-molecular-weight polyethylene composites prepared by a filler prelocalization method.* Journal of Applied Polymer Science, 2007. **105**(1): p. 158-168.

64. Gao, X., et al., *Influence of processing parameters during ultrasound assisted extrusion on the properties of polycarbonate/carbon nanotubes composites.* Composites Science and Technology, 2017. **144**: p. 125-138.

65. Guo, J.X., et al., *Aspect Ratio Effects of Multi-walled Carbon Nanotubes on Electrical, Mechanical, and Thermal Properties of Polycarbonate/MWCNT Composites.* Journal of Polymer Science Part B-Polymer Physics, 2014. **52**(1): p. 73-83.

66. Douglas, J.F. and E.J. Garboczi, *Intrinsic viscosity and the polarizability of particles having a wide range of shapes*, in *Advances in Chemical Physics, Vol 91*, I. Prigogine and S.A. Rice, Editors. 1995. p. 85-153.

67. Bicerano, J., J.F. Douglas, and D.A. Brune, *Model for the Viscosity of Particle Dispersions.* Journal of Macromolecular Science, Part C, 1999. **39**(4): p. 561-642.

68. Penu, C., et al., *Rheological and electrical percolation thresholds of carbon nanotube/polymer nanocomposites.* Polymer Engineering & Science, 2012. **52**(10): p. 2173-2181.

69. Arboleda-Clemente, L., et al., *Segregated conductive network of MWCNT in PA12/PA6 composites: Electrical and rheological behavior.* Polymer Composites, 2017. **38**(12): p. 2679-2686.

70. Pötschke, P., T.D. Fornes, and D.R. Paul, *Rheological behavior of multiwalled carbon nanotube/polycarbonate composites.* Polymer, 2002. **43**(11): p. 3247-3255.

71. Arrigo, R. and G. Malucelli, *Rheological Behavior of Polymer/Carbon Nanotube Composites: An Overview.* Materials, 2020. **13**(12).

72. Faridirad, F., S. Ahmadi, and M. Barmar, *Rheological and electrical percolation thresholds of multi-walled carbon nanotube/in-situ polymerised Nylon12 nanocomposites.* Micro & Nano Letters, 2018. **13**(11): p. 1594-1599.

73. Hennrich, F., et al., *The mechanism of cavitation-induced scission of single-walled carbon nanotubes.* Journal of Physical Chemistry B, 2007. **111**(8): p. 1932-1937.

74. Liu, P. and T.M. Wang, *Ultrasonic-assisted chemical oxidative cutting of multiwalled carbon nanotubes with ammonium persulfate in neutral media.* Applied Physics a-Materials Science & Processing, 2009. **97**(4): p. 771-775.

75. Lucas, A., et al., *Kinetics of Nanotube and Microfiber Scission under Sonication.* Journal of Physical Chemistry C, 2009. **113**(48): p. 20599-20605.

76. Pagani, G., et al., *Competing mechanisms and scaling laws for carbon nanotube scission by ultrasonication.* Proceedings of the National Academy of Sciences of the United States of America, 2012. **109**(29): p. 11599-11604.

77. Chew, H.B., et al., *Compressive dynamic scission of carbon nanotubes under sonication: fracture by atomic ejection.* Proceedings of the Royal Society a-Mathematical Physical and Engineering Sciences, 2011. **467**(2129): p. 1270-1289.

78. Jang, J.W., C.E. Lee, and C.J. Lee, *Exponential decrease of scission length and low tensile strength of bamboo-shaped multi-walled carbon nanotubes under ultrasonication.* Current Applied Physics, 2017. **17**(4): p. 507-512.

79. Liu, F., et al., *Preparation of short carbon nanotubes by mechanical ball milling and their hydrogen adsorption behavior.* Carbon, 2003. **41**(13): p. 2527-2532.

80. Pierard, N., et al., *Ball milling effect on the structure of single-wall carbon nanotubes.* Carbon, 2004. **42**(8-9): p. 1691-1697.

81. Kukovecz, A., et al., *Long-time low-impact ball milling of multi-wall carbon nanotubes.* Carbon, 2005. **43**(5): p. 994-1000.

82. Burgio, N., et al., *Mechanical alloying of the Fe-Zr system in different milling condition.* Journal De Physique, 1990. **51**(14): p. C4265-C4271.

83. Burgio, N., et al., *Mechanical alloying of the Fe-Zr system - Correlation between input energy and end-products.* Nuovo Cimento Della Societa Italiana Di Fisica D-Condensed Matter Atomic Molecular and Chemical Physics Fluids Plasmas Biophysics, 1991. **13**(4): p. 459-476.

84. Iasonna, A. and M. Magini, *Power measurements during mechanical milling. An experimental way to investigate the energy transfer phenomena.* Acta Materialia, 1996. **44**(3): p. 1109-1117.

85. Magini, M., A. Iasonna, and F. Padella, *Ball milling: An experimental support to the energy transfer evaluated by the collision model.* Scripta Materialia, 1996. **34**(1): p. 13-19.

86. Magini, M. and A. Iasonna, *Energy-transfer in mechanical alloying.* Materials Transactions Jim, 1995. **36**(2): p. 123-133.

87. Padella, F., et al., *Mechanical alloying of the Pd-Si system in controlled conditions of energy-transfer.* Journal of the Less-Common Metals, 1991. **175**(1): p. 79-90.

88. Guo, W., et al., *Synthesis of amorphous and metastable Ti40Al60 alloys by mechanical alloying of elemental powders.* Journal of Materials Science, 1994. **29**(9): p. 2436-2444.

89. Liu, L. and M. Magini, *Correlation between energy transfers and solid state reactions induced by mechanical alloying on the Mo33Si66 system.* Journal of Materials Research, 1997. **12**(9): p. 2281-2287.

90. Kozma, G., et al., *Experimental validation of the Burgio-Rojac model of planetary ball milling by the length control of multiwall carbon nanotubes.* Carbon, 2016. **105**: p. 615-621.

91. Ros, T.G., et al., *Surface oxidation of carbon nanofibres.* Chemistry-a European Journal, 2002. **8**(5): p. 1151-1162.

92. Misak, H.E., et al., *Functionalization of carbon nanotube yarn by acid treatment.* International Journal of Smart and Nano Materials, 2014. **5**(1): p. 34-43.

93. Temirgaliyeva, T.S., et al., *Synthesis of Multiwall Carbon Nanotubes by the Cvd Method and their Functionalization.* Journal of Engineering Physics and Thermophysics, 2020. **93**(1): p. 91-94.

94. Simmons, T.J., et al., *Noncovalent Functionalization as an Alternative to Oxidative Acid Treatment of Single Wall Carbon Nanotubes with Applications for Polymer Composites.* ACS Nano, 2009. **3**(4): p. 865-870.

95. Hsieh, C.-T., et al., *Hierarchical oil–water separation membrane using carbon fabrics decorated with carbon nanotubes.* Surface and Coatings Technology, 2016. **286**: p. 148-154.

96. Knyazev, A., et al., *Selective Adsorption of Proteins on Single-Wall Carbon Nanotubes by Using a Protective Surfactant.* Chemistry – A European Journal, 2011. **17**(51): p. 14663-14671.

97. Konya, Z., et al., *Large scale production of short functionalized carbon nanotubes.* Chemical Physics Letters, 2002. **360**(5-6): p. 429-435.

98. Vittore, A., M.R. Acocella, and G. Guerra, *Graphite functionalization by ball milling with sulfur.* SN Applied Sciences, 2019. **1**(2): p. 169.

99. Rubio, N., et al., *Ball-Milling Modification of Single-Walled Carbon Nanotubes: Purification, Cutting, and Functionalization.* Small, 2011. **7**(5): p. 665-674.

100. Ambrogi, V., et al., *Multiwalled carbon nanotubes functionalized with maleated poly(propylene) by a dry mechano-chemical process.* Polymer, 2012. **53**(2): p. 291-299.

101. Choi, E.Y., J.Y. Kim, and C.K. Kim, *Fabrication and properties of polycarbonate composites with polycarbonate grafted multi-walled carbon nanotubes by reactive extrusion.* Polymer, 2015. **60**: p. 18-25.

102. Eskandari, P., et al., *Polymer-functionalization of carbon nanotube by in situ conventional and controlled radical polymerizations.* Advances in Colloid and Interface Science, 2021. **294**: p. 102471.

103. Yang, S.-Y., et al., *Effect of functionalized carbon nanotubes on the thermal conductivity of epoxy composites.* Carbon, 2010. **48**(3): p. 592-603.

104. Barick, A.K. and D.K. Tripathy, *Preparation, characterization and properties of acid functionalized multi-walled carbon nanotube reinforced thermoplastic polyurethane nanocomposites.* Materials Science and Engineering: B, 2011. **176**(18): p. 1435-1447.

105. Choi, W. and S.H. Ryu, *Electrical and rheological properties of MWCNT/polycarbonate nanocomposites.* Polymer Bulletin, 2013. **70**.

106. Buffa, F., et al., *Effect of nanotube functionalization on the properties of single-walled carbon nanotube/polyurethane composites.* Journal of Polymer Science Part B: Polymer Physics, 2007. **45**(4): p. 490-501.

107. Hadianfard, M.J., M. Alizadeh, and M. Moradzaman, *Effects of chemical and mechanical funtionalization of carbon nanotubes on the behavior of a CNT/Phenolic nanocomposite.* Boletin Del Grupo Espanol Del Carbon, 2019(51): p. 20-25.

108. Cha, J., et al., *Comparison to mechanical properties of epoxy nanocomposites reinforced by functionalized carbon nanotubes and graphene nanoplatelets.* Composites Part B-Engineering, 2019. **162**: p. 283-288.

109. Rojac, T., et al., *The application of a milling map in the mechanochemical synthesis of ceramic oxides.* Journal of the European Ceramic Society, 2006. **26**(16): p. 3711-3716.

110. Ma, P.C., et al., *In-situ amino functionalization of carbon nanotubes using ball milling.* J Nanosci Nanotechnol, 2009. **9**(2): p. 749-53.

111. Kasaliwal, G., A. Goldel, and P. Potschke, *Influence of Processing Conditions in Small-Scale Melt Mixing and Compression Molding on the Resistivity and Morphology of Polycarbonate-MWNT Composites.* Journal of Applied Polymer Science, 2009. **112**(6): p. 3494-3509.

112. Grady, B.P., et al., *Glass Transition Behavior of Single-Walled Carbon Nanotube-Polystyrene Composites.* Macromolecules, 2009. **42**(16): p. 6152-6158.

113. Bach, Q.-V., C.M. Vu, and H.T. Vu, *Effects of Co-Silanized Silica on the Mechanical Properties and Thermal Characteristics of Natural Rubber/Styrene-Butadiene Rubber Blend.* Silicon, 2020. **12**(8): p. 1799-1809.

114. Shooli, S.A. and M. Tavakoli, *Styrene Butadiene Rubber/Epoxidized Natural Rubber (SBR/ENR50) Nanocomposites Containing Nanoclay and Carbon Black as Fillers for Application in Tire-Tread Compounds.* Journal of Macromolecular Science Part B-Physics, 2016. **55**(10): p. 969-983.

115. Poikelispää, M., et al., *The effect of partial replacement of carbon black by carbon nanotubes on the properties of natural rubber/butadiene rubber compound.* Journal of Applied Polymer Science, 2013. **130**(5): p. 3153-3160.

116. Ahmad, S. and R.J. Schaefer, *Energy saving tire with silica-rich tread*. 1985, UG Licensing Services Inc: United States.

117. Smart, S.K., et al., *Shortened double-walled carbon nanotubes by high-energy ball milling.* International Journal of Nanotechnology, 2007. **4**(5): p. 618-633.

118. Forro, L., et al., *Tuning the length dispersion of multi-walled carbon nanotubes by ball milling.* Aip Advances, 2013. **3**(9).

119. Guo, J.X., et al., *A new finding for carbon nanotubes in polymer blends: Reduction of nanotube breakage during melt mixing.* Journal of Thermoplastic Composite Materials, 2018. **31**(1): p. 110-118.

120. Li, Y.B., et al., *Transformation of carbon nanotubes to nanoparticles by ball milling process.* Carbon, 1999. **37**(3): p. 493-497.

121. Kim, Y.A., et al., *Effect of ball milling on morphology of cup-stacked carbon nanotubes.* Chemical Physics Letters, 2002. **355**(3-4): p. 279-284.

122. Ozden, S., et al., *Ballistic Fracturing of Carbon Nanotubes.* Acs Applied Materials & Interfaces, 2016. **8**(37): p. 24819-24825.

123. De Silva, K.K.H., et al., *Restoration of the graphitic structure by defect repair during the thermal reduction of graphene oxide.* Carbon, 2020. **166**: p. 74-90.

124. Souza, N., et al., *In situ tracking of defect healing and purification of single-wall carbon nanotubes with laser radiation by time-resolved Raman spectroscopy.* RSC Advances, 2015. **5**(76): p. 62149-62159.

125. Lu, K.L., et al., *Mechanical damage of carbon nanotubes by ultrasound.* Carbon, 1996. **34**(6): p. 814-816.

126. Pierard, N., et al., *Production of short carbon nanotubes with open tips by ball milling.* Chemical Physics Letters, 2001. **335**(1-2): p. 1-8.

127. Papp, I.Z., et al., *Effect of planetary ball milling process parameters on the nitrogen adsorption properties of multiwall carbon nanotubes.* Adsorption-Journal of the International Adsorption Society, 2013. **19**(2-4): p. 687-694.

128. Zhao, Z., et al., *Multiple functionalization of multi-walled carbon nanotubes with carboxyl and amino groups.* Applied Surface Science, 2013. **276**: p. 476-481.

129. Allegri, M., et al., *Toxicity determinants of multi-walled carbon nanotubes: The relationship between functionalization and agglomeration.* Toxicology Reports, 2016. **3**: p. 230-243.

130. Adamson, A.W. and A.P. Gast, *Physical Chemistry of Surfaces*. 6th ed. 1997: Wiley.

131. Chen, L., W. Yu, and H. Xie, *Enhanced thermal conductivity of nanofluids containing Ag/MWNT composites.* Powder Technology, 2012. **231**: p. 18-20.

132. Lu, Y., et al., *Preparation of carbon–silicon carbide composite powder via a mechanochemical route.* Ceramics International, 2013. **39**(4): p. 4421-4426.

133. Chua, C.K., et al., *Ball-milled sulfur-doped graphene materials contain metallic impurities originating from ball-milling apparatus: their influence on the catalytic properties.* Physical Chemistry Chemical Physics, 2016. **18**(27): p. 17875-17880.

134. Xu, J., et al., *Sulfur–Graphene Nanostructured Cathodes via Ball-Milling for High-Performance Lithium–Sulfur Batteries.* ACS Nano, 2014. **8**(10): p. 10920-10930.

135. Bernal-Ortega, P., et al., *Sulfur-modified carbon nanotubes for the development of advanced elastomeric materials.* Polymers, 2021. **13**(5).

136. Rao, C.N.R., R. Venkataraghavan, and T.R. Kasturi, *CONTRIBUTION TO THE INFRARED SPECTRA OF ORGANOSULPHUR COMPOUNDS.* Canadian Journal of Chemistry, 1964. **42**(1): p. 36-42.

137. Lonkar, S.P., V.V. Pillai, and S.M. Alhassan, *Scalable solid-state synthesis of MoS2-NiS2/graphene nanohybrids as bifunctional electrocatalysts for enhanced overall water splitting.* Materials Advances, 2020. **1**(4): p. 794-803.

138. Hegedüs, M., et al., *Mechanochemical approach to a Cu2ZnSnS4 solar cell absorber via a "micro-nano" route.* Journal of Materials Science, 2018. **53**(19): p. 13617-13630.

139. Hori, H., et al., *Process for crosslinking polycarbonate resins*, U.S.P.a.T. Office, Editor. 1983, Furukawa Electric Co Ltd: United States.

140. Jang, B.N. and C.A. Wilkie, *The thermal degradation of bisphenol A polycarbonate in air.* Thermochimica Acta, 2005. **426**(1): p. 73-84.

141. Abbås, K.B., *Thermal degradation of bisphenol A polycarbonate.* Polymer, 1980. **21**(8): p. 936-940.

142. Davis, A. and J.H. Golden, *Thermal degradation of polycarbonate.* Journal of the Chemical Society B: Physical Organic, 1968(0): p. 45-47.

143. K. Muallah, S., *Experimental Determination of the Elastic and Viscous Behavior of Polycarbonate Melts at Different Temperatures and Their Relationship to the Steady State Viscosity via the Cox-Merz Rule.* Iraqi Journal of Chemical and Petroleum Engineering, 2014. **15**(2): p. 49-59.

144. Pötschke, P., et al., *Rheological and dielectrical characterization of melt mixed polycarbonate-multiwalled carbon nanotube composites.* Polymer, 2004. **45**(26): p. 8863-8870.

145. Pötschke, P., et al., *Comparisons Among Electrical and Rheological Properties of Melt-Mixed Composites Containing Various Carbon Nanostructures.* Journal of Macromolecular Science, Part A, 2009. **47**(1): p. 12-19.

146. Huang, S., et al., *Dynamic Electrical and Rheological Percolation in Isotactic Poly(propylene)/Carbon Black Composites.* Macromolecular Materials and Engineering, 2012. **297**(1): p. 51-59.

147. Linares, A., et al., *Broad-Band Electrical Conductivity of High Density Polyethylene Nanocomposites with Carbon Nanoadditives: Multiwall Carbon Nanotubes and Carbon Nanofibers.* Macromolecules, 2008. **41**(19): p. 7090-7097.

148. Sheng, P., E.K. Sichel, and J.I. Gittleman, *Fluctuation-Induced Tunneling Conduction in Carbon-Polyvinylchloride Composites.* Physical Review Letters, 1978. **40**(18): p. 1197-1200.

149. Chatterjee, A.P., *A percolation-based model for the conductivity of nanofiber composites.* The Journal of Chemical Physics, 2013. **139**(22).

150. Krause, B., et al., *Influence of dry grinding in a ball mill on the length of multiwalled carbon nanotubes and their dispersion and percolation behaviour in melt mixed polycarbonate composites.* Composites Science and Technology, 2011. **71**(8): p. 1145-1153.

151. Huang, J.C., *Carbon black filled conducting polymers and polymer blends.* Advances in Polymer Technology, 2002. **21**(4): p. 299-313.

152. Pötschke, P., M.H. Arnaldo, and H.J. Radusch, *Percolation behavior and mechanical properties of polycarbonate composites filled with carbon black/carbon nanotube systems.* Polimery, 2012. **57**(3): p. 204-211.

153. Caamaño, C., B. Grady, and D.E. Resasco, *Influence of nanotube characteristics on electrical and thermal properties of MWCNT/polyamide 6,6 composites prepared by melt mixing.* Carbon, 2012. **50**(10): p. 3694-3707.

154. Müller, M.T., et al., *Influence of feeding conditions in twin-screw extrusion of PP/MWCNT composites on electrical and mechanical properties.* Composites Science and Technology, 2011. **71**(13): p. 1535-1542.

155. Yetgin, S.H., *Effect of multi walled carbon nanotube on mechanical, thermal and rheological properties of polypropylene.* Journal of Materials Research and Technology, 2019. **8**(5): p. 4725-4735.

156. Pötschke, P., et al., *A Novel Strategy to Incorporate Carbon Nanotubes into Thermoplastic Matrices.* Macromolecular Rapid Communications, 2008. **29**(3): p. 244-251.

157. Sandler, J.K.W., et al., *Ultra-low electrical percolation threshold in carbon-nanotube-epoxy composites.* Polymer, 2003. **44**(19): p. 5893-5899.

158. Deplancke, T., et al., *Impact of carbon nanotube prelocalization on the ultra-low electrical percolation threshold and on the mechanical behavior of sintered UHMWPE-based nanocomposites.* Polymer, 2017. **111**: p. 204-213.

159. Dalnoki-Veress, K., T. Salez, and F. Restagno, *Why can't you separate interleaved books?* Physics Today, 2016. **69**(6): p. 74-75.

160. Polli, H., et al., *Degradation behavior and kinetic study of ABS polymer.* Journal of Thermal Analysis and Calorimetry, 2009. **95**(1): p. 131-134.

161. Khairy, M., N.H. Amin, and R. Kamal, *Optical and kinetics of thermal decomposition of PMMA/ZnO nanocomposites.* Journal of Thermal Analysis and Calorimetry, 2017. **128**(3): p. 1811-1824.

162. Kubatovics, F. and M. Blazsó, *Thermal decomposition of polyamide-6 in the presence of PVC.* Macromolecular Chemistry and Physics, 2000. **201**(3): p. 349-354.

163. Evgin, T., et al., *Effect of aspect ratio on thermal conductivity of high density polyethylene/multi-walled carbon nanotubes nanocomposites.* Composites Part a-Applied Science and Manufacturing, 2016. **82**: p. 208-213.

164. Paul, A., B.P. Grady, and W.T. Ford, *PMMA composites of single-walled carbon nanotubes-graft-PMMA.* Journal of Applied Polymer Science, 2014. **131**(4).

165. Heberer, D.P., et al., *CRYSTALLIZATION AND MORPHOLOGY OF SEMICRYSTALLINE POLYIMIDES.* Macromolecules, 1991. **24**(8): p. 1890-1898.

166. Lipatov, Y.S. and V.P. Privalko, *Glass transition in filled polymer systems.* Polymer Science U.S.S.R., 1972. **14**(7): p. 1843-1848.

167. Pötschke, P., et al., *Influence of Twin Screw Extrusion Conditions on MWCNT Length and Dispersion and Resulting Electrical and Mechanical Properties of Polycarbonate Composites.* Polymers, 2024. **16**(19): p. 2694.

168. Otaegi, I., et al., *The Effect of the Preparation Method and the Dispersion and Aspect Ratio of CNTs on the Mechanical and Electrical Properties of Bio-Based Polyamide-4,10/CNT Nanocomposites.* Polymers, 2019. **11**(12): p. 2059.

169. Hornbostel, B., et al., *Mechanical properties of triple composites of polycarbonate, single-walled carbon nanotubes and carbon fibres.* Physica E: Low-dimensional Systems and Nanostructures, 2008. **40**(7): p. 2434-2439.

170. Hwang, S.H., et al., *Fabrication and Characterization of Aluminum-Carbon Nanotube Powder and Polycarbonate/Aluminum-Carbon Nanotube Composites.* Journal of Composite Materials, 2010. **44**(23): p. 2711-2722.

171. Via, M.D., et al., *Tensile modulus modeling of carbon black/polycarbonate, carbon nanotube/polycarbonate, and exfoliated graphite nanoplatelet/polycarbonate composites.* Journal of Applied Polymer Science, 2012. **124**(3): p. 2269-2277.

172. Bagotia, N. and D.K. Sharma, *Ballistic behavior of multiwalled carbon nanotube-reinforced toughened polycarbonate nanocomposites.* Polymer Composites, 2020. **41**(5): p. 1813-1819.

173. Tullo, A.H., *STRETCHING TIRES' MAGIC TRIANGLE.* Chemical & Engineering News, 2009. **87**(46): p. 10-14.

174. Bartlett, J.S. *Low-Roling-Resistance Tires Can Save You Money at the Pump*. 2022.

175. Campanelli, J.R., et al., *Dispersion, temperature and torque models for an internal mixer.* Polymer Engineering & Science, 2004. **44**(7): p. 1247-1257.

176. Kablov, V.F., A.Y. Kurakin, and A.Y. Aleksandrina, *A Study of the Stages of Mixing of a Model Mixture of Rubber and Carbon Black on a Brabender Plastograph.* International Polymer Science and Technology, 2016. **43**(2): p. 33-36.

177. Kamal, M.R. and S. Sourour, *KINETICS AND THERMAL CHARACTERIZATION OF THERMOSET CURE.* Polymer Engineering and Science, 1973. **13**(1): p. 59-64.

178. García, D.B., et al., *Effect of carbon nanotubes content on the vulcanization kinetic in styrene-butadiene rubber compounds.* Polymer Engineering and Science, 2019. **59**: p. E327-E336.

179. Song, J.-p., et al., *The effect of carbon black morphology to the thermal conductivity of natural rubber composites.* International Journal of Heat and Mass Transfer, 2019. **137**: p. 184-191.

180. Nah, C., et al., *Reinforcing rubber with carbon nanotubes.* Journal of Applied Polymer Science, 2010. **118**(3): p. 1574-1581.

181. Bijarimi, M., Z. Hassan, and M.D. Beg, *Mechanical Properties of Industrial Tyre Rubber Compounds.* Journal of Applied Sciences, 2010. **10**.

182. Zhao, J. and M.S. Skurich, *Passenger tire having low rolling resistance with improved wet traction and treadwear*. 2015: United States.

183. Kim, S.W., et al., *Effects of Aggregate Structure and Dimension of Carbon Nanotubes on the Mechanical, Electrical and Thermal Properties of Rubber Composites.* Asian Journal of Chemistry, 2013. **25**(9): p. 5165-5170.

184. Shao, H.-Q., H. Wei, and J.-H. He, *DYNAMIC PROPERTIES AND TIRE PERFORMANCES OF COMPOSITES FILLED WITH CARBON NANOTUBES.* Rubber Chemistry and Technology, 2018. **91**(3): p. 609-620.